The Dissertation Committee for Manish Kumar Niranjan
certifies that this is the approved version of the following dissertation:

THEORETICAL INVESTIGATION OF CONTACT MATERIALS FOR EMERGING ELECTRONIC AND SPINTRONIC DEVICES

Committee:

L. Kleinman, Co-Supervisor

A. A. Demkov, Co-Supervisor

A. H. MacDonald

M. Tsoi

S. K. Banerjee

J. Chelikowsky

THEORETICAL INVESTIGATION OF CONTACT MATERIALS FOR EMERGING ELECTRONIC AND SPINTRONIC DEVICES

by

Manish Kumar Niranjan, M.S

Dissertation

Presented to the Faculty of the Graduate School of

The University of Texas at Austin

In Partial Fulfillment

of the Requirements

for the Degree of

Doctor of Philosophy

The University of Texas at Austin

December 2007

Acknowledgement

I would like to express my deep and sincere gratitude to my supervisors, Professor Leonard Kleinman and Professor Alexander A. Demkov, for their guidance, encouragement and support during the entire period of PhD work.

I warmly thank Dr. B. R. Sahu for his personal guidance and suggestions on many topics.

I warmly thank Dr. Stefan Zollner for introducing and encouraging me to work on contact materials significant to semiconductor industry.

My warm thanks are due to Dr. S. C. Song, Dr. Prashant Majhi and Dr. H. Mustafa for their supervision during the internship period at SEMATECH Inc.

My sincere thanks are due to all committee members Prof. A. H. MacDonald, Prof. S. Banerjee, Prof. M. Tsoi and Prof. J. Chelikowsky.

Finally, I would like to thank my friends Adrian Ciucivara and Dr. M. N. Huda who always kept the atmosphere cheerful with their warm presence.

MANISH KUMAR NIRANJAN

The University of Texas at Austin
August 2007

THEORETICAL INVESTIGATION OF CONTACT MATERIALS FOR EMERGING ELECTRONIC AND SPINTRONIC DEVICES

Publication No. _____________

Manish Kumar Niranjan, Ph.D.
The University of Texas at Austin, 2007

Supervisors: Leonard Kleinman and Alexdander A. Demkov

We present a theoretical study of the electronic structure, surface energies and work functions of orthorhombic Pt monosilicide and germanides of Pt, Ni, Y and Hf within the framework of density functional theory (DFT). Calculated work functions for the (001) surfaces of PtSi, NiGe and PtGe suggest that these metals and their alloys can be used as self-aligned contacts to p-type silicon and germanium. In addition, we also study electronic structure and calculate the Schottky-barrier height at Si(001)/PtSi(001) interface and GaAs(001)/NiPtGe(001) interfaces with different GaAs(001) and NiPtGe (001) terminations. The p-type Schottky barrier height of 0.28 eV at Si/PtSi interface is found in good agreement with predictions of a simple metal induced gap states (MIGS) theory and available experiment. This low barrier suggests PtSi as a low contact resistance junction metal for silicon CMOS technology. We identify the growth conditions necessary to stabilize this orientation. The calculated p-type Schottky barrier heights (SBH) at different GaAs/NiPtGe interfaces vary by as much as 0.18 eV around the average value of 0.5 eV. We further identify and discuss factors responsible for strong Fermi level pinning resulting in small variation in the p-SBH. We also present a theoretical study of magnetic state of β-MaAs and show that it is antiferromagnetic and explain the lack of observed long-range order.

Contents

List of Figures

List of Tables

Chapter 1

Introduction

The rapid advancement in microelectronics during the last 40 years has been realized through miniaturization and integration of the electronic devices into integrated circuits (IC) based on complementary metal oxide semiconductor (CMOS) technology. CMOS technology uses n-type and p-type field effect transistors (FETs) to produce digital logic elements that are superior to other available logic technologies for many applications. The dominance of CMOS over technologies is based on its low power consumption as well as the ability to scale CMOS and achieve simultaneous improvements in power consumption, speed and cost. As the result of continuous device scaling (miniaturization of the device), the CMOS transistor dimensions and critical parameters, such as channel length, oxide layer thickness, etc. have already reached in nanometers and their further scaling turned out to be challenging. According to the International Technology Roadmap for Semiconductors (ITRS) [24] one of the most pressing concerns of CMOS technology beyond the 65 nm node (channel length) is the contact resistances in source/drain regions between the doped silicon and metal alloy (silicide). Thus the roadmap calls for a new contact technology by the 45 nm node. Recently, silicides of platinum and rare earth metals have been found promising to address contact resistance issue in CMOS.

Furthermore, due to continuous device scaling, silicon CMOS technology is rapidly reaching fundamental limits and has led to intense research into alternative channel materials. The low mobility of carriers in silicon is a serious obstacle towards the performance requirement of nanoscale CMOS transistors as defined in ITRS [24]. Recently, III-V compound semiconductors (such as GaAs, InSb) and germanium have generated lot of interest as potential candidates for implementation in future CMOS-type devices, due to their much higher electron mobility than that in silicon [13-18, 25-27]. However, to fully exploit transport properties of germanium, GaAs and other compound semiconductors, a low resistance contact technology will have to be developed, much in the same way as that in silicon CMOS technology based on metal-silicides. Metal germanides have attracted much attention recently and seem to be very promising to make low resistance contacts since they are closely related to analogous silicides in respect to their compositions and structures.

In this work we study 1) electronic structure, surface energies, work functions of PtSi, NiGe, PtGe, Y_5Ge_3, YGe, Hf_5Ge_3, HfGe 2) electronic structure and SBH at PtSi/Si and GaAs/NiPtGe interfaces.

The rest of the chapter is organized as follows. In section 1.1, we provide an overview of CMOS transistor and the role of silicide (germanide) in the formation of low resistance contacts to source, grain and gate in it. In section 1.2 and 1.3, we discuss metal semiconductor contacts (M/S) and various models to calculate barrier height at the M/S interface. And, in section 1.4, we provide an overview of this work/thesis.

1.1 CMOS transistor and use of silicides (germanides)

It is known that metal-oxide-semiconductor field-effect-transistor (MOSFET) is the basic building block for the absolute majority of today’s electronic systems [29]. A cross section of two modern MOSFETs placed side-by-side resulting into a CMOS-FET is shown schematically in Figure 1.1a, with a metal silicide layer present in the three electrode terminals, gate, source, and drain for both transistors.

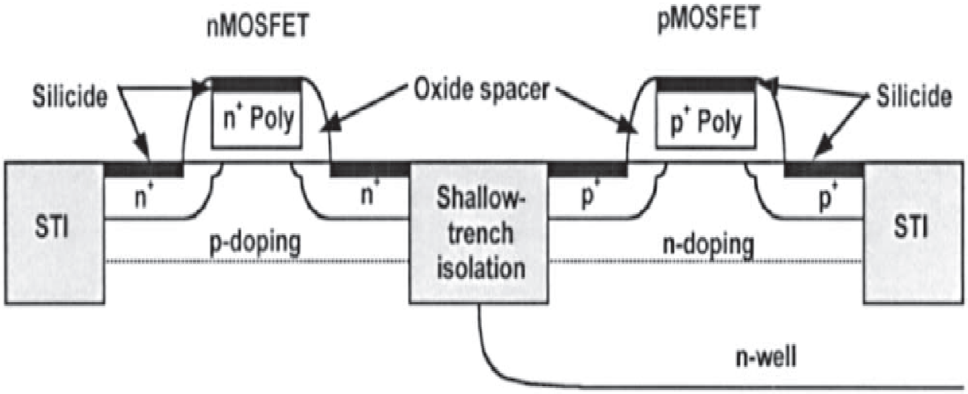

Figure 1.1a: *Cross section of modern CMOS transistors with an n-channel MOSFET (n-MOSFET) and a p-channel MOSFET (pMOSFET).*

The silicide layer is usually formed simultaneously in all six electrode areas. The two transistors are of opposite polarity, one n-channel MOSFET (n-MOSFET) built directly on the p-type substrate and one p-channel MOSFET (p-MOSFET) built inside the n-well, that is, in turn first formed on the same p-type substrate as shown. Constructed simultaneously on the same substrate, the two transistors are usually connected in series between the power supply terminals in an electronic circuit to minimize standby power dissipation, that is, the complementary MOS (CMOS) technology. Among many technical parameters, the gate length of a MOSFET, which is one of the most critical indicators of the integration technology, will decrease below 10 nm by year 2016, in order to attain the desired technological gain and economical profit. Figure 1.1b shows, how the electrical contact resistivity should be scaled according to ITRS in order to deliver MOSFETs with the desired performance. Depicted in Figure 1.1c is the ITRS prediction for how sheet resistance in the source/drain regions of a MOSFET should scale. The requirements for a decreasing source/ drain series resistance and contact resistivity in smaller MOSFETs are well treated by Ng and Lynch [30].

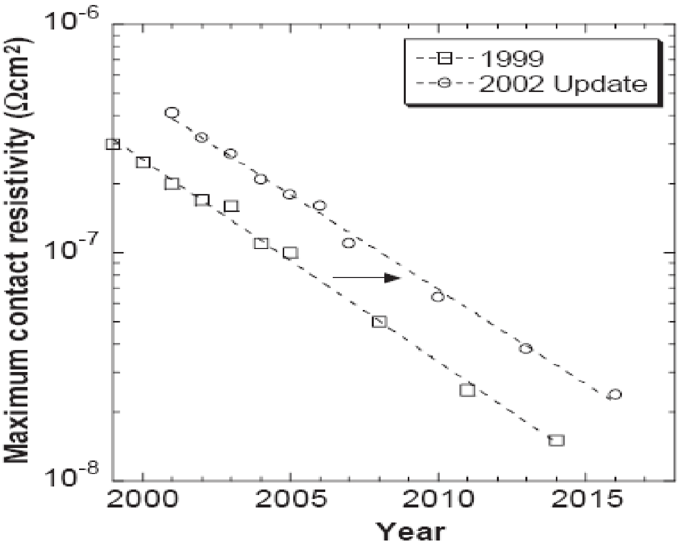

Figure 1.1b: *Maximum contact resistivity as predicted in ITRS 1999 and 2002 update.*

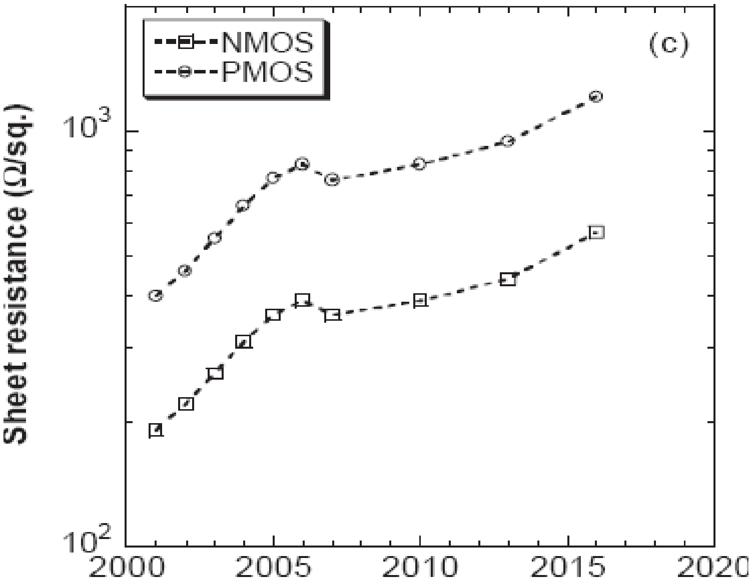

Figure 1.1c: *Scaling of sheet resistance as predicted in ITRS (1999 and 2002 update).*

The main driver for the continuous advancement in very large scale integration (VLSI) has been the search for electronic circuits of higher performance and lower cost. In particular, the speed of an electronic circuit is one of the major concerns. To enhance the speed, parasitic capacitance and series resistance should both be minimized to reduce the RC (resistance-capacitance) time delay and increase the clock frequency [31]. For this purpose of reaching higher speed, metal silicides have been utilized to form ohmic contacts with source, drain, and gate silicon because of their low resistivity, low contact resistance to Si, reasonable thermal stability, and excellent process compatibility with standard Si technology. Undoubtedly, they have played a crucial part in the rapid development of microelectronic devices [1], and have recently attracted renewed attention [2, 3]. Over the past two decades, silicides of Ti, Co and Ni have been successively used in integrated circuit manufacturing [1-7]. Fig. 1.1d shows evolution of gate sheet resistance with the use of silicides and reduction of channel length with time. In the deep submicron regime NiSi is now succeeding $CoSi_2$ [8, 9, 12, 13]. However, both $CoSi_2$ and NiSi exhibit large (0.5-0.6 eV) Schottky barriers to Si, in addition, NiSi suffers from low thermal stability [8]. This contact resistance already amounts to a quarter of the total parasitic resistance [8], and will clearly only rise as scaling continues. (Fig 1.1e shows all the resistances which can be significant in a MOSFET). Thus, it is desirable to identify new metals or alloys with a lower Schottky barrier to n- and p- type Si for use in NMOS and PMOS, respectively [4]. Adding Pt to NiSi significantly enhances the NiSi thermal stability [10]. PtSi is attractive in its own right as a p-type contact. It has relatively low (0.2 eV) Schottky barrier on Si (001) and has excellent thermal stability.

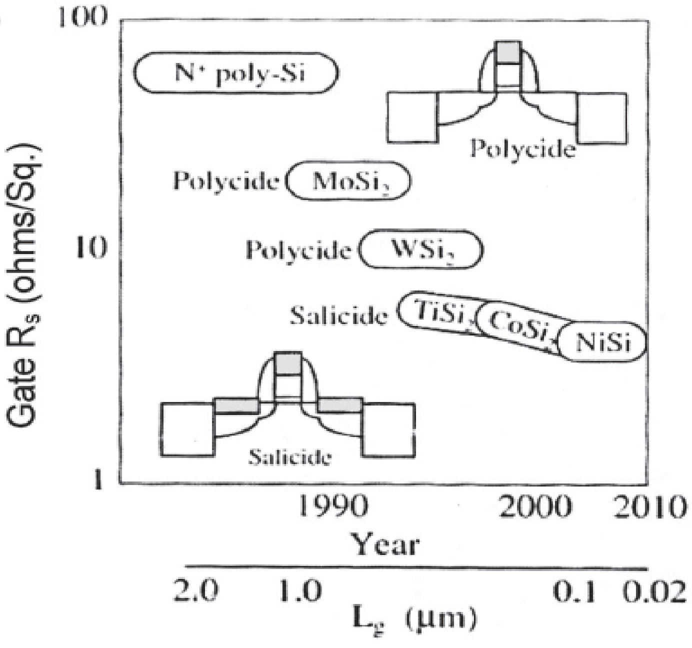

Figure 1.1d: *Evolution of gate sheet resistance with gate technology over time. Ref [1]*

Silicides can be formed by either a solid state reaction between a metal and Si, or by co-depositing the metal and Si. The solid-state reaction method is used in a salicide process [1] (self-aligned silicide process), whereas the co-deposition method is used in a polycide process [1]. Fig. 1.1e shows the parasitic resistances in a MOSFET which can be significantly large if silicides are not used to form contacts.

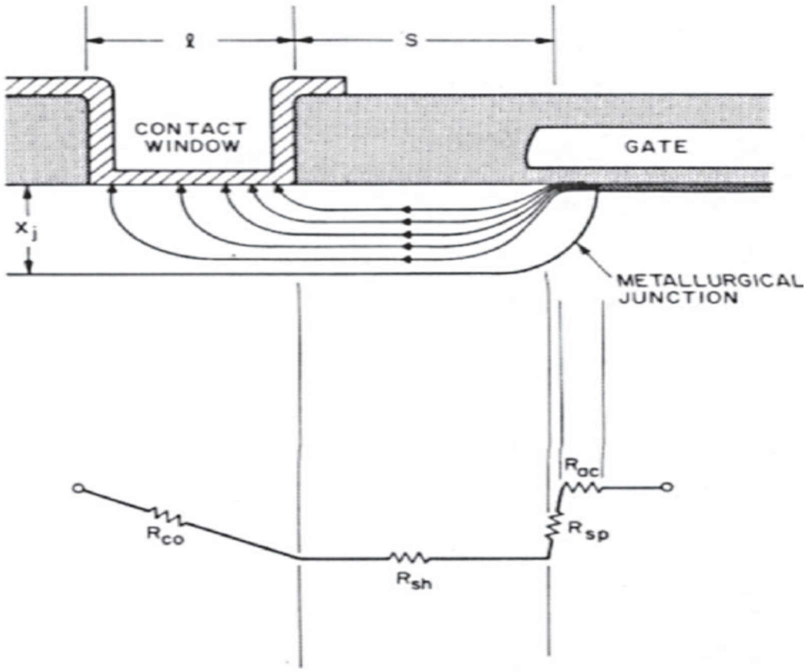

Figure 1.1e: *Resistance components for the series resistance from the source/drain region to the channel [30].*

Unlike metal silicides [1], metal germanides have not, until recently, attracted much attention, presumably, due to the lack of practical applications. However, this is about to change, as scaling of traditional silicon based technology is rapidly reaches its physical limit, a germanium channel field effect transistor (FET) is generating a lot of interest [13-18]. It is worth noting that the first (bipolar) transistor of Bardeen, Brattain and Shockley was made of Ge [19]. The germanium channel metal oxide semiconductor FET (MOSFET) offers high mobility of both carriers (electrons and holes) resulting in higher overdrive current, enhanced transconductance, and higher cutoff frequencies as compared with a Si transistor. Historically, the use of germanium has been limited due to the lack of a stable native oxide and processing technology. Ironically, the emerging use of alternative high-k dielectrics as the gate insulator in Si-based technology [20] may help finally realize the full potential of a germanium MOSFET [17, 18]. Nevertheless, to fully exploit transport properties of germanium, a low resistance contact technology will have to be developed based on metal germanides, much in the same way that self aligned metal silicides are used in a standard complimentary metal oxide semiconductor (CMOS) process today. Thus germanides with low *n*- and *p*-type Schottky barriers to the germanium channel (for use in NMOS and PMOS devices) need to be identified. Germanides are closely related to analogous silicides in respect to their compositions and structures. In the deep submicron regime (22 nm and below) NiGe, PtGe and their alloys appear to be promising as low barrier contacts to p-type germanium [21-23].

In addition to germanium, III-V compound semiconductors such as GaAs and InSb have emerged as potential candidates for implementation in future CMOS-type devices, due to their much higher electron mobility than that in silicon [25-27]. Compound semiconductors are also attractive materials for applications where silicon can not be used, such as optoelectronics, high-power devices, high frequency devices, and high temperature devices. However, transport properties of GaAs and other compound semiconductors can not be exploited fully with out the development of ohmic contact technology. Interestingly, germanides of nickel have been used to make contacts in GaAs based devices [28]. However, their further development is required to address the contact resistance issues in nanoscale devices.

1.2 Metal-Semiconductor contacts

Metallic contacts to semiconductors are an essential part of most modern electronic and optoelectronic devices. The electronic structure of metal/semiconductor (MS) interfaces plays a fundamental role in the transport properties of these junctions. One of the most relevant parameters of MS junctions is its Schottky barrier height (SBH), which is a measure of the energy mismatch across the interface between the Fermi energy of the metal and the majority carrier band edge of the semiconductor. For ohmic contacts, a vanishing SBH is desirable while larger value of the SBH is sought for more rectifying contact. However, a control of the SBH is always sought regardless of the application. Generally, in most cases an ohmic contact is wanted. Due to their technological importance, MS contacts and their SBH have been the subject of numerous investigations

[32, 33]. Despite the enormous progress in solid state physics and semiconductor device physics, in particular, the factors controlling the SBH are still not yet fully understood. Recent advances in Schottky barrier concepts have shown the importance of the occurrence of interfaces states and polarization of the bonds at the interface.

1.2.1 Current transport mechanism, contact resistance and SBH at metal-semiconductor (MS) interface

When a metal directly contacts a semiconductor, the valence and conduction bands of the semiconductor bend to make the Fermi levels in the metal and the semiconductor equal. The carrier transport mechanisms through this M/S interface are strongly influenced by the doping concentration in the semiconductor (N_D), barrier height (φ_B) and the temperature (T). When the semiconductor is lightly doped ($N_D < 10^{17}$ cm^{-3}), the depletion width becomes very wide and the electrons cannot tunnel through the semiconductor interface. The only way the electrons can transport between the semiconductor and the metal is by thermionic emission (TE) over the potential barrier φ_B. In case of medium doping of the semiconductor ($10^{17} < N_D < 10^{18}$ cm^{-3}), electrons can partially tunnel through the semiconductor interface and both the thermionic and tunneling processes are equally important. The current flow is controlled by electrons with some thermal energy tunneling through the mid-section of the potential barrier. This is called thermionic field-emission (TFE). When the semiconductor is extremely heavily doped (>10^{18} cm– 3), the electrons can tunnel through from the Fermi level in the metal into the semiconductor. This process is called field-emission (FE).

A useful parameter indicative of the electron tunneling probability is kT/E_{00}, where E_{00} is defined by,

$$E_{00} = \frac{qh}{4\pi}\sqrt{\frac{N_D}{m^{*}\varepsilon}}$$

where q is the electronic charge, h is Plancks constant, m^* is the effective mass of the tunneling electron, ε is the dielectric constant of the semiconductor. With increasing the doping concentration (N_D), the width of the depletion region decreases, making it easier for carriers to tunnel through. This indicates that when E_{00} is high relative to thermal energy kT, the probability of the electron transport by tunneling increases. Therefore, the ratio kT/E_{00} is a useful measure of the relative importance of the thermionic process to the tunneling process. For lightly doped semiconductors, $kT/E_{00} >> 1$ and the thermionic emission is the dominant current flow mechanism. For $kT/E_{00} \sim 1$ both the thermionic and tunneling mechanisms are dominant, and for $kT/E_{00} << 1$, the tunneling mechanism dominates the current flow. Again, note that the doping level in the semiconductor and the temperature influence the carrier transport mechanism

The specific contact resistance ρ_c is given by the reciprocal of the derivative of the current density with respect to the voltage,

$$\rho_c = \left(\frac{dJ}{dV} \right)^{-1}_{V=0}$$

The current-voltage relations have been developed based on the simple energy band models using the Wentzel-Kramers-Brillouin (WKB) approximation [34, 35]. This approximation provides relatively simple results that are sufficient here to obtain the basic background for estimating the Ohmic contact resistance ρ_c.

For the thermionic-emission mechanism, ρ_c is given by,

$$\rho_c = C_1 \exp\left(\frac{q\phi_B}{kT} \right)$$

where $C_1 = (k/qA)T$. For contacts with heavy doping in which the tunneling process is the dominant current transport mechanism, ρ_c is given by,

$$\rho_c = C_2 \exp\left(\frac{q\phi_B}{E_{00}} \right) = C_2 \exp\left[\frac{4\pi\sqrt{\varepsilon m^*}}{h} \left(\frac{\phi_B}{\sqrt{N_D}} \right) \right]$$

where C_2 has a weak temperature dependence. For the contacts in which thermionic field-emission is the dominant transport mechanism, ρ_c is given by,

$$\rho_c = C_2 \exp\left[\frac{\phi_B}{\sqrt{N_D} Coth(E_{00}/kT))} \right]$$

where C_3 is functions of φ_B and T. The theory predicts that reduction of ρ_c is achieved by reducing the φ_B value and/or increasing the N_D value in the vicinity of the MS interface.

A more detailed description of the MS interface and transport properties can be found in [2c, 2d]

1.2.2 Experimental techniques to probe metal/semiconductor interfaces

In this section we shortly present the most important experimental techniques which are used to study the properties of metal/semiconductor junctions and the kind of information that these techniques can provide. A much more extensive and detailed discussion of these techniques can be found in numerous textbooks and review articles, e.g. [38-44].

F. Braun reported in 1874 in his pioneering work on the rectifying properties of metal contacts to metal sulfides [45]. Rectifiers and early MS diodes were fabricated by pressing fine metal wires and plates on semiconducting crystals and were mostly used in broadcasting technologies in the 20's. Given their technical importance, an extensive work on metal contacts to several sulfides was carried out by Schottky [46]. Historically, metal/semiconductor interfaces have been characterized by $I-V$ and C-V measurements [47-50]. In these cases, the conductance and the capacitance of the junction are measured as a function of the applied voltage. In general, barrier heights obtained from $I-V$ are more reliable [41] than those deduced from $C-V$ results, since in the latter case the boundary layer may introduce important corrections. However, $C-V$ measurements, which are best suited for junctions exhibiting poor rectification [51], are widely used since the experiments are essentially electrostatic measurements of equilibrium charge distributions versus position and are almost free from transport effects. The weakness of both approaches is that the SBH is derived from the measured curves using rather simplified models of the interface. With continuous improvements in epitaxy and spectroscopic techniques, these measurements have nowadays reached a precision of the order of 0.05 eV [52, 53].

In addition to the classic transport techniques mentioned above, optical and electron spectroscopy and photoemission techniques have become alternative approaches which can also provide additional interface properties such as, for example, atomic positions and energies of interface electron states. Most of these experiments are performed on devices with thin overlayers or quantum wells. A common difficulty of these techniques is their weak lateral resolution which is an important issue in semiconductor interface research. A widely used technique to overcome this drawback is the ballistic- electron emission microscopy (BEEM) [54] which is based on scanning tunneling microscopy (STM). Thereby, an STM tip is used to inject electrons into a thin metal overlayer grown on top of a semiconductor substrate. A fraction of these electrons reaches ballistically the interface region and contributes to the current when the voltage of the tip is higher than the SBH. BEEM allows probing the electronic transport with a lateral resolution of about 20 ˚A [39, 55, 56]. Electronic and optical techniques which are most commonly used for characterizing semiconductor surfaces and interfaces are listed in Table 1.2.2a together with the kind of information that they provide.

Technique	**Information**
Auger electron spectroscopy (AES)	Surface chemical composition, depth distribution
X-ray photoemission spectroscopy (XPS)	Surface chemical composition and bonding
UV photoemission spectroscopy	Fermi levcl with respect to band edges, work function, valence-band states
Soft X-ray photoemission spectroscopy (SXPS)	Surface chemical composition and bonding, Fermi level with respect to hand edges, valence-band state
Constant initial (CIS) and final (CFS) state spectroscopies	Empty states above Fermi level
Angle-resolved photoemission spectroscopy(ARPES)	Atomic bonding symmetry, Brillouin zone dispersion
Surface extended X-ray absorption fine structure (SEXAFS)	Local surface bonding coordination
Inverse photoemission spectroscopy	Unoccupied surface state and conduction-band states
Laser-excited photoemission spectroscopy (LAPS)	Band gap states
Low-energy electron (LEED) and positron (LEPD) diffraction	Surface atomic geometry
X-ray diffraction	Bulk atomic geometry
Total external X-ray diffraction (TEXRD)	Interface lattice structure, interface strain
Low-energy electron-loss	Interface reactions, electronic and atomic excitations

spectroscopy (LELS,EELS)	
Surface photovoltage spectroscopy (SPS)	Band gap states. work function, band bending
Infrared absorption spectroscopy (IR)	Band gap states, atomic bonding and coordination
Cathodoluminescence spectroscopy (CLS)	Surface states within band gap, buried interface states, new compound band gap energies
Photoluminescence spectroscopy	Surface chemical compounds, states within band gap
Surface reflectance spectroscopy (SRS)	Surface dielectric response
Ellipsometry	Surface or interface dielectric response
Surface photoconductivity spectroscopy	States within band gap
Raman scattering spectroscopy	Interface compounds and bonding, hand bending
Rutherford backscattering spectroscopy (RBS)	Surface atomic geometry, depth distribution
Secondary ion mass spectroscopy (SIMS)	Interface chemical composition, depth distribution
He beam scattering	Energy transfer dynamics, surface charge density
Scanning tunneling microscopy (STM)	Surface atomic geometry, surface morphology, filledand empty-state geometries
Atomic force microscopy (AFM)	Surface electrostatic forces, magnetic polarization
Scanning tunneling spectroscopy (STS)	Band gap states, heterojunction band offsets
Ballistic electron energy microscopy (BEEM)	Barrier heights, heterojunction hand offsets, barrier height lateral inhomogeneity
Field ion microscopy (FIM)	Surface atomic motion, atomic geometry
High-resolution transmission electron microscopy (HRTEM)	Interface lattice structure
Low-energy electron microscopy (LEEM)	Surface morphology, diffusion, phase transformations, grain boundary motion
Electron paramagnetic resonance (EPR)	Unpaired electron spins

Table 1.2.2a: *Electronic and optical techniques for characterizing semiconductor surfaces and interfaces and the corresponding information they can provide (from [57]).*

1.3 SBH, Fermi level pinning and phenomenological models

More than 60 years after the pioneering experiments by Braun and the experimental developments by Schottky and Deutschmann [46], a first model of the barrier formation was proposed independently in 1938 by Schottky [58] and Mott [59]. Fig 1.3a illustrates the band diagram of Schottky's *Gedankenexperiment* illustrating the formation of a Schottky barrier. The metal and the semiconductor are supposed to be electrically neutral, separated from each other and without any surface charge. We consider the case of an *n*-type semiconductor with electron affinity χ_s and work function φ_s, smaller than the metal work function φ_m. When the metal and the semiconductor come in electrical contact, the two Fermi levels are forced to coincide and electrons pass from the semiconductor into the metal. The result is an excess of negative charge on the metal surface and a negative charge depletion zone in the semiconductor near its surface. These excess charges form an interface dipole and produce an electric field, directed from the semiconductor to the metal. By bringing the metal and the semiconductor closer together, the gap between the two materials vanishes and the electric field corresponds now to a gradient of the electron potential in the depletion layer, resulting in the well known band-bending regime. The Schottky-Mott model leads to a *n*-type SBH φ_n given by,

$$\varphi_n = \varphi_m - \chi_s$$

And, therefore, depends linearly on the metal work function. However, experimental results as those presented in Fig. 1.3b for GaAs do not confirm this relationship since the SBH depends only weakly on the metal work function. Deviation from the Schottky-Mott behavior are very often measured in terms of the slope parameter, $S = \frac{d\varphi_n}{d\varphi_m}$

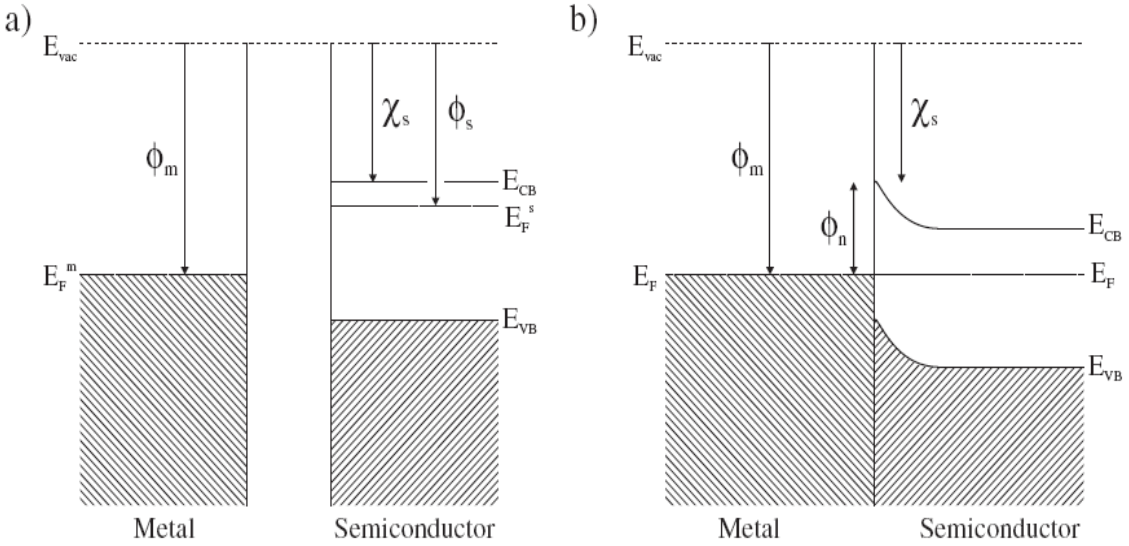

,

Figure 1.3a: *Schematic band diagram of band bending according to the Schottky model for the MS interface.* ***a)*** *Before contact,* ***b)*** *after the contact formation. An n-type semiconductor is assumed*

first introduced by Kurtin *et al.* [60] and describing the dependence of the SBH on the metal work function. According to the Schottky-Mott model *S* should be equal to 1, while it is of the order of 0.1 for metal contacts to GaAs [60, 61].

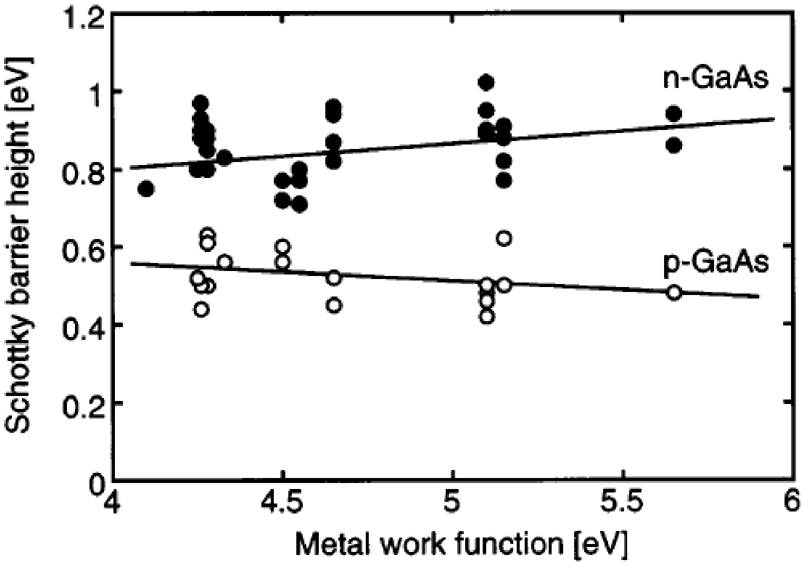

Figure 1.3b: *Barrier height at metal/GaAs as a function of metal work function [62]*

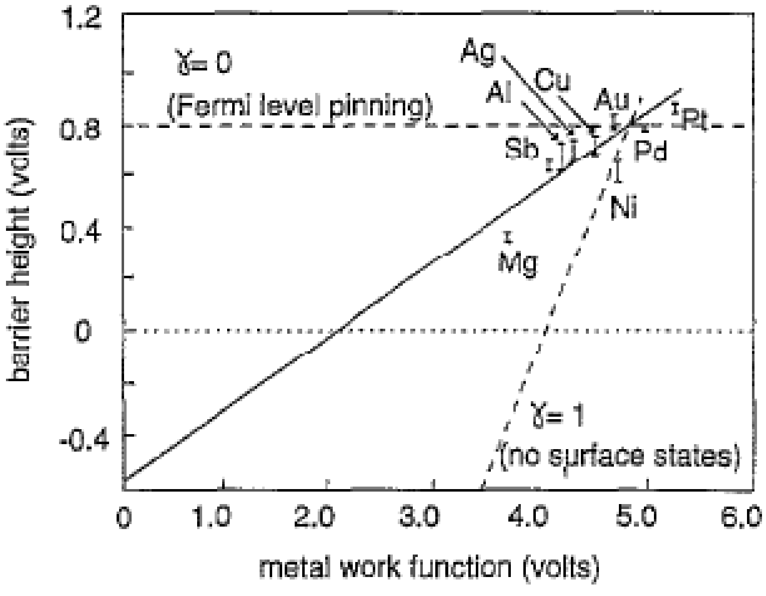

Figure 1.3c: *Barrier height at metal/n-Si as a function of metal work function.*

An important limitation of the Schottky-Mott model is the neglect of surface states. This prompted Bardeen [63] to propose in 1947 a different model. He showed that if the density of localized states [64, 65] having energies distributed in the semiconductor energy gap is sufficiently high, double layer at the free surface of a semiconductor is formed from a net charge of electrons in surface states and a space charge of opposite sign. He concluded that this double layer will tend to make the work function independent of the height of the Fermi level in the interior of the semiconductor, and the rectification characteristics or barrier height at the metal-semiconductor contact are then practically independent of the metal (Figure 1.3d). In this extreme case, the SBH does not depend at all on the metal work function, i.e. $S = 0$ when surface states are present. All models of MS interfaces proposed afterwards are essentially generalizations of these two basic models. In the following section we discuss the phenomenological formula for *n*-SBH derived by Cowley and Sze in 1965 [66]. This formula is valid as long as the Fermi level pinning of SBH is described by the presence of interface gap states. These interface gap states may be of the nature of semiconductor surface states, metal induced gap states (MIGS) [67], defect states [68] and/or disorder induced gap states [69]. We will also discuss how the polarized bonds at the interface can lead to apparent Fermi level pinning effect [70].

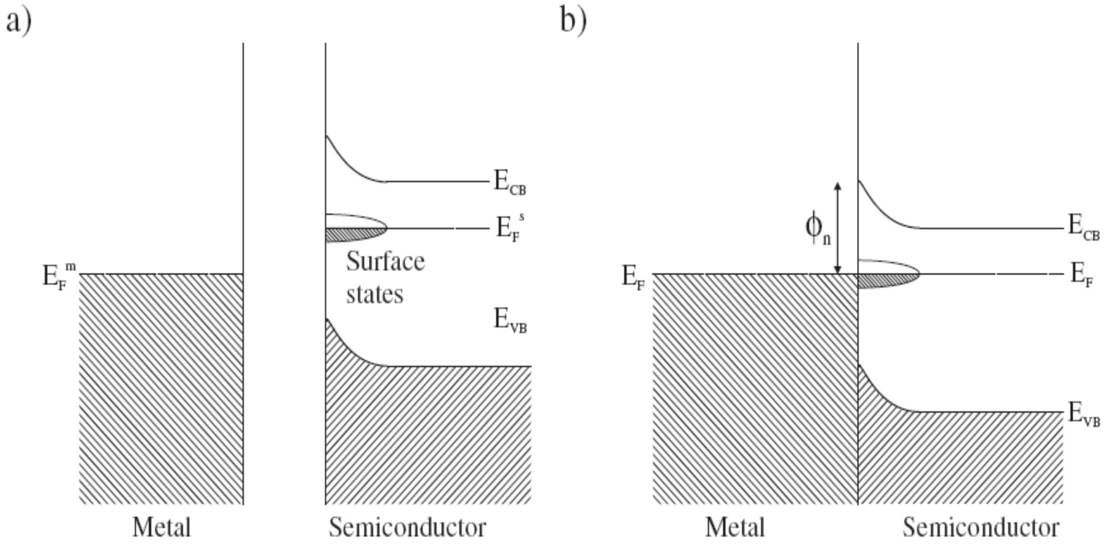

Figure 1.3d: *Schematic band diagram of band bending according to the Bardeen model for the MS interface.* ***a)*** *Before contact,* ***b)*** *after the contact formation. The Fermi level is pinned by a high density of surface states of the semiconductor.*

1.3.1 Theory of SBH in presence of surface states

The energy band diagram of a metal–*n* type semiconductor contact is shown in Figure 1.3.1a. We assume that the contact between metal and semiconductor has an interfacial layer of the order of atomic dimensions and surface states density (per unit area per eV) at the interface is a property only of the semiconductor surface and is independent of the metal. The energy φ_0 is measured from the valence band edge at the semiconductor surface and specifies the level below which all surface states must be filled for charge neutrality at the semiconductor surface. This is also called the charge neutrality level (CNL). The quantity φ_{Bn} is the *n*-SBH at metal semiconductor contact and $\Delta\varphi_n$ is the image force lowering of the *n*-SBH [37]. The interfacial layer is assumed to have a thickness of a few angstroms and will be assumed transparent to electrons whose energy is greater than the potential barrier.

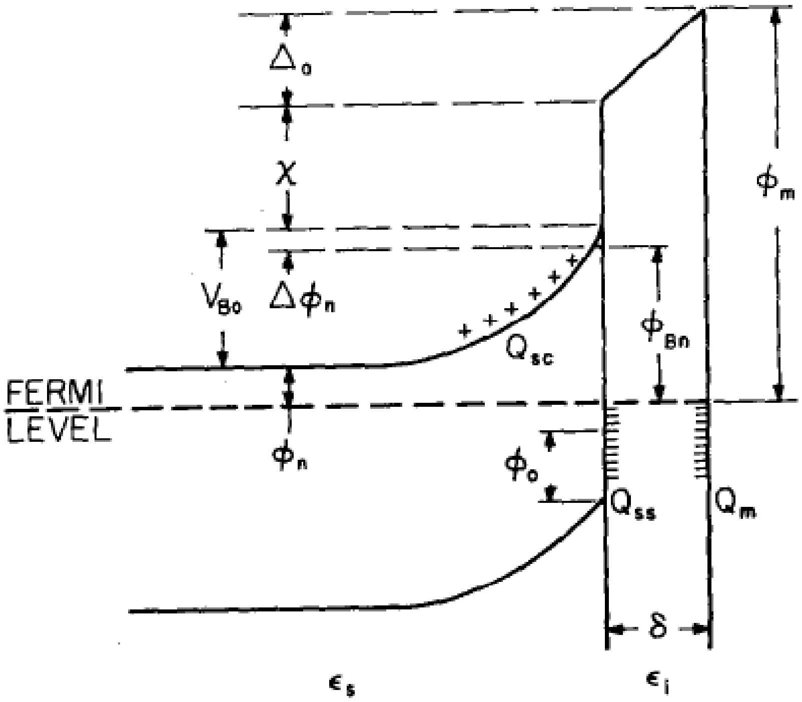

Figure 1.3.1a: *Energy band diagram of a metal- n-type semiconductor contact with an interfacial layer.* φ_m *is the work function of metal;* φ_{Bn} *is the n-SBH of metal-*

semiconductor surface barrier; φ_0 *is the charge neutrality level;* $\Delta\varphi_n$ *is the image force barrier lowering;* φ_n *is the energy difference between conduction band and Fermi level in the semiconductor;* Δ_0 *is the potential across interfacial layer;* χ *is the lectron affinity of semiconductor;* V_{B0} *is the diffusion potential;* ε_s *and* ε_i *are the dielectric constant of semiconductor and interfacial layer;* δ *is the thickness of interfacial layer;* Q_{ss} *is the surface charge density on semiconductor;* Q_m *is the surface density on metal [66].*

We consider a semiconductor with acceptor surface states whose density is D_s states/cm^2/eV and assume that D_s is constant over the energy range from φ_0 to the Fermi level. For a uniform distribution the surface state charge density on the semiconductor Q_{ss} is given by

$$Q_{ss} = -eD_s(E_g - \varphi_0 - \varphi_{Bn} - \Delta\varphi_n)C/cm^2, \qquad (1.3.1\text{ a})$$

The quantity in parentheses is simply the difference between the Fermi level at the surface and φ_0 .D_s times this quantity yields the number of surface states above φ_0 which are full. The space charge which forms in the depletion layer of the semiconductor can be expressed as an equivalent surface charge density, which is the net charge/cm^2 looking into the bulk semiconductor from a point just inside the semiconductor surface. The charge is obtained by solving Poisson's equation for the depletion layer of the semiconductor and can be written as

$$Q_{sc} = [2e\varepsilon_s N_D(\varphi_{Bn} + \Delta\varphi_n - \varphi_n - kT/e)]^{1/2} C/cm^2, \qquad (1.3.1\text{b})$$

where N_D is the donor density of the bulk semiconductor. The equivalent surface charge density on the semiconductor surface is given by the sum of Eqs. (1.3.1a) and (1.3.1b). In the absence of any space charge effects in the interfacial layer, an exactly equal and opposite charge Q_m. develops on the metal surface. For thin interfacial layers, such effets are negligible, and Q_m be written as

$$Q_m = -(Q_{ss} + Q_{sc}) = eD_s(E_g - \varphi_0 - \varphi_{Bn} - \Delta\varphi_n) - [2e\varepsilon_s N_D(\varphi_{Bn} + \Delta\varphi_n - \varphi_n - kT/e)]^{1/2} \qquad (1.3.1\text{c})$$

The potential Δ_0 across the interfacial layer with no voltage applied to the junction can be obtained by the application of Gauss's law to the surface charge on the metal and semiconductor:

$$\Delta_0 = -\delta(Q_m / \varepsilon_i), \qquad (1.3.1d)$$

where ε_i is the dielectric constant of the interfacial layer and δ its thickness. Another relation for Δ_0 can be obtained by inspection of the energy band diagram of Figure 1.3.1a:

$$\Delta_0 = \varphi_m - (\chi + \varphi_{Bn} + \Delta\varphi_n), \qquad (1.3.1e)$$

These results from the fact the Fermi level must be constant throughout the metal-interfacial layer-semiconductor system at equilibrium. If Δ_0 is eliminated from Eqs. (1.3.1d) and (1.3.1e), and Eq. (1.3.1c) is used to substitute for Q_m, we obtain

$$(\varphi_m - \chi) - (\varphi_{Bn} + \Delta\varphi_n) = \left[\frac{2e\varepsilon_s N_D \delta^2}{\varepsilon_i^{\,2}}\left(\varphi_{Bn} + \Delta\varphi_n - \varphi_n - kT/e\right)\right]^{1/2} - \frac{eD_s\delta}{\varepsilon_i}\left(E_g - \varphi_0 - \varphi_{Bn} - \varphi_n\right)$$

(1.3.1f)

Equation (1.3.1f) can now be solved for $\varphi_{Bn.}$ Introducing the quantities V_1, α, and γ

$$V_1 = 2e\varepsilon_s N_D \delta^2 / \varepsilon_i^{\,2} \quad ; \quad \alpha = eD_s\delta / \varepsilon_i \quad ; \quad \gamma = 1/(1+\alpha) = \varepsilon_i /(\varepsilon_i + e\delta D_s) \quad ; \qquad (1.3.1g)$$

Equation (1.3.1f) can be written as

$$\varphi_{Bn} = \left[\gamma(\varphi_m - \chi) + (1-\gamma)(E_g - \varphi_0) - \Delta\varphi_n\right] + \left\{\gamma^2 V_1/2 - \gamma^{3/2}\left[\begin{array}{l} V_1(\varphi_m - \chi) + (1-\gamma)(E_g - \varphi_0)V_1/2 - \\ V_1(\varphi_n + kT/e)/\gamma + \gamma V_1^2/4 \end{array}\right]^{1/2}\right\}$$

(1.3.1h)

Equation (1.3.1g) can be used to calculate V_1 if values of δ and ε_i are estimated: For vacuum-cleaved or well cleaned semiconductor substrates the interfacial layer will have a thickness of atomic dimensions, i.e., 4 or 5 Å. The dielectric constant of such a thin layer can be well approximated by the free space value, and since this approximation represents a lower limit for ε_i, it leads to an overestimation of V_1 .For $\varepsilon_s \sim 10\,\varepsilon_i$ and $N_D < 10^{18}$ cm^{-3} , V_1 is small, of the order of 0.01 eV, and the term in the curly brackets in Eq. (1.3.1h) is estimated to be less than 0.04 eV. Neglect of this term in Eq. (1.3.1h) reduces the equation to

$$\varphi_{Bn} = \gamma(\varphi_m - \chi) + (1-\gamma)(E_g - \varphi_0) - \Delta\varphi_n, \qquad (1.3.1i)$$

$$\text{where } \gamma = \left(1 + \frac{e^2\delta D_s}{\varepsilon_i}\right)^{-1}$$

The γ in Eq. (1.3.1i) is the theoretical slope parameter and is often compared with experimental slope parameter S. Moreover, the symbol S is also used for γ in the literature. The experimental values of γ, φ_0 , and D_s for different semiconductor systems can be obtained by fitting experimental values of φ_{Bn} with Eq. (1.3.1i). For silicon, γ, φ_0, and D_s were obtained to be 0.27±0.05, 0.30±0.36 eV, and 2.7±0.7 $\times 10^{13}$ states/cm^2/eV [32]. For GaAs, γ, φ_0, and D_s were obtained to be 0.07±0.05, 0.53±0.33 eV, and 12.5±10.0 $\times 10^{13}$ states/cm^2/eV.

1.3.2 MIGS, Defect states and Disorder induced gap states models

Heine in 1965 [67] showed that localized surface states as assumed by Bardeen [64] and Cowley and Sze [66], can not exist at the metal-semiconductor interface. However resonance surface states or metal induced gap states (MIGS) can exist which behave for the practical purposes in the same way. This follows from simple considerations of matching the wavefunctions the metal-semiconductor boundary. For an energy E below Fermi energy in the gap of the semiconductor, the solutions of the Schrodinger equation will decay exponentially in the semiconductor but propagate as Bloch states on the metal side of the junction to form the ordinary states of the metal. If the x-axis is taken as perpendicular to the surface then for some value of $\mathbf{k} = \mathbf{k}_{||}$ parallel to the surface, e.g., $k_y = k_z = 0$, we have the bands shown in Fig. 1.3.2a . At energy E, the exponential solution in the semiconductor can always be joined onto the two Bloch states with wave vector ensuring that both ψ and its derivative can be matched at the boundary. Thus for energies in the semiconductor band gap of the states of the metal all have tails in the semiconductor.

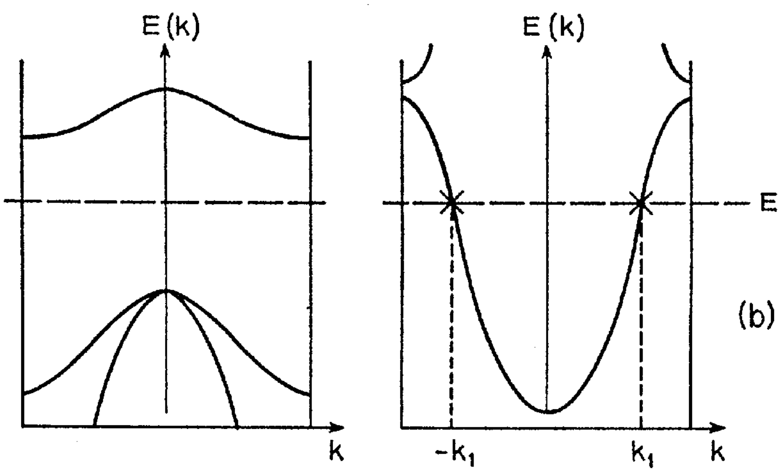

Figure 1.3.2a: *An energy E of a surface state in the band gap of the semiconductor corresponds to two propagating Bloch functions* k_1, $-k_1$ *in the metal.*

Thus resonance states or MIGS are basically the tails of metal wavefunction rather than separate states in the band gap of the semiconductor and Bloch states of the bulk semiconductor with complex wave vector. Since the MIGS are split off from the valence and the conduction band, their character varies across the gap from mostly donor type close to the top of the valence band to mostly acceptor type close to the bottom of the conduction band. The charge transferred between the metal and the semiconductor then pins the Fermi level above, at, or below the charge-neutrality level φ_0 of the MIGS when the electronegativity of the metal is smaller, equal to, and larger than, respectively, the one of the semiconductor. Eq. (1.3.1i) still describes the dependence of *n*-SBH on metal work function. Monch [51] realized that the slope parameter γ (or S) in the MIGS model (Eq. 1.3.1i) depends only on the product of the density of states (D_s) around the charge neutrality level and the width δ of the related dipole layer which is determined by the average band-gap energy of the semiconductor. On the other hand the band-gap of the semiconductor is related to the electronic polarizability (ε_∞-1). As apparent in Figure 1.3.2b, the S values of nineteen different semiconductors follow a pronounced chemical trend when ($1/S$ -1) is plotted over (ε_∞ - 1). A least-square fit to the data yields

$$S = \frac{1}{1 + 0.1(\varepsilon_\infty - 1)^2}, \qquad (1.3.2a)$$

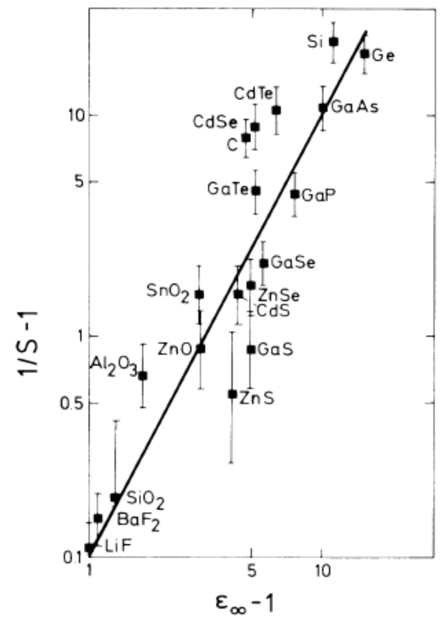

Figure 1.3.2b: *Slope parameter S plotted versus the electronic contribution ε_∞ of the dielectric constant of the semiconductor.*

In 1984, Tersoff [71] suggested a method to calculate the charge neutrality level in the MIGS model. He suggested that the charge neutrality level can be associated with the branch point of the complex band structure in the fundamental gap since MIGS are actually Bloch states of the bulk semiconductor with complex wave vector and charge neutrality level must fall at or near the energy where the gap states cross over from valence to conduction band character. In one dimension this energy corresponds to the branch point of the complex band structure [72]. The branch point in the fundamental gap coincides with the zero of the cell-averaged real-space Green's function calculated along a judiciously chosen crystallographic direction:

$$G(\vec{x},E)=\sum_{n,k}\frac{e^{i\vec{k}\cdot\vec{x}}}{E-E_{n,k}+i\eta}=0$$

Here E is the energy in the fundamental gap, and a small imaginary term $i\eta$ in the denominator insures convergence. The direction $\boldsymbol{x}$ should be chosen to give the slowest decaying evanescent state. To calculate the branch point from the actual calculation of the complex band structure, the band energy $E_n(\boldsymbol{k})$ is considered as a multi-valued function $E(\boldsymbol{k})$ of a complex wave vector $\boldsymbol{k} = \boldsymbol{g} + i\boldsymbol{h}$. The usual band structure is then the $Re(E) - g$

cross-section of the Reimann surface. Starting at the lower energy surface (e.g., the valence band) and going into the complex ***k***-plane around the branch point and back we end up on the next energy surface (i.e., the conduction band). Solutions of the Schrodinger equation with the energy in the band gap thus have complex wave vectors, and are therefore spatially decaying. The character of the solution continuously changes from that of the lower energy band to higher energy band, with branch point serving as a point of cross-over from donor-like states to acceptor-like states. The physical connection between the wave vector at a branch point and the interface dipole was first made by Heine [67], who used its inverse (the penetration dept of the evanescent gap state) to estimate the separation of the positive charge in the metal and negative charge in the surface states. The dipole is $D = 4\pi\sigma t/\varepsilon$, where σ is the charge density per unit area, ε is the dielectric constant, and $t = 1/q$ is the mean separation between the negative charge in the surface states and the positive charge in the metal. Here q is the imaginary wave vector describing the complex band structure in the forbidden energy gap of the semiconductor. When the wave functions are matched at the metal-semiconductor interface, the evanescent wave describes the exponential decay of the metal wave function inside the semiconductor. In other words the metal effectively charges the imaginary wave vector states rather than induces them. Note that the complex band structure is a bulk property of a material, and thus can be calculated without a detailed interface model.

Models based on defect states and disorder induced gap states (DIGS) have also been proposed to explain Fermi level pinning at metal-semiconductor interfaces. The defect states model proposed by Wieder [73] and Spicer [68] *et al* identifies the interface states at the metal-semiconductor contacts as electronic states of native defects which are created during the formation of the junction. The defect states model was motivated by the observations that Schottky barriers on III-V compound semiconductors were found to be insensitive to within 0.2 eV to the metals used and to follow no apparent chemical trend. The DIGS model proposed by Hasegawa *et al* [69] was used to explain the observed Fermi level pinning and correlation between the insulator-semiconductor and metal-semiconductor interfaces.

1.3.3 Limitations of the MIGS model

The MIGS model has been applied to the analysis of SBHs observed at a variety of metal-semiconductor interfaces to deduce MIGS densities [74]. Despite large scatter in the experimental data, reasonable agreement can usually be found for most semiconductors with predictions based on interface gap states, i.e., Eq. (1.3.1i). The widespread application of the MIGS model and its apparent success in the analysis of experimental data belie the fact that several major assumptions of the MIGS model have been shown to be without the basis. Experimental data from epitaxial metal-semiconductor interfaces have shown that the SBH depends on the interface atomic structure [75]. Calculations further showed that the distribution of the MIGS depends strongly on the interface structure [70] and that the charge neutrality condition of the interfacial semiconductor could not be determined by the distribution of electronic states within the fundamental gap alone due to the presence of surface states elsewhere in the semiconductor [76]. Furthermore, it was pointed out [77] nearly two decades ago that MIGS or any other model which assume the interface states to be in thermal equilibrium with only the semiconductor could not be reconciled with the nearly perfect ideality factors observed in current-voltage (*I-V*) experiments. These facts suggest that even though MIGSs are present at every MS interface, they do not lead to an interface dipole in the fashion assumed by existing models and explicitly expressed in Eq. (1.3.1.i).

Theoretical and experimental work on epitaxial metal-semiconductor interfaces show that the SBH between the same metal-semiconductor pair can vary by more than one third of the band gap, with a mere change in the interface structure [78]. This finding suggests first that the SBH at nonepitaxial metal-semiconductor interfaces could be inhomogeneous, a fact which has often been found to be true in experiments [70]. At the same time, a structure-dependent interface dipole also seems to suggest that the SBH likely depends sensitively on the choice of the metal, in conflict with the observed Fermi level pinning effect. Why the SBH which depends so critically on the structure of epitaxial interfaces should appear to assume nearly constant values for polycrystalline metal-semiconductor interfaces is still an unanswered question. Given the discussion above concerning MIGS model's fundamental problems, the question becomes "If not gap states, what else can lead to relationships like Eqs. (1.3.1i)?. Recently Tung [70] has showed quantitatively that chemical bonding at the metal-semiconductor interfaces can lead to the apparent Fermi level pinning effect and is a primary mechanism of the Schottky barrier height. In the following we derive the formula like Eq. (1.3.1i) but with chemical bonding as the primary mechanism rather than the interface gap states.

1.3.4 Theory of SBH based on the interfacial chemical bonding

When a metal is joined by a semiconductor, and thermodynamic equilibrium is reached, chemical bonding has to take place. At an ordinary, polycrystalline metal-semiconductor interface, the bonding geometry likely changes from place to place, leading to a locally varying interface dipole. The measured SBH then reflects some weighted average of this interface dipole. Because of the randomness of the interface structure, there is the expectation that the interface dipole can perhaps be estimated using bulk-derived properties. It therefore makes some sense to analyze the electric dipole at a metal-semiconductor interface using established techniques in chemical physics, developed largely for molecular systems. The total energy of a multi-atomic molecule can be written, neglecting higher order terms, as [79, 80]

$$E_{tot}(Q_A, \ldots\ldots Q_N) = \sum_A \left(E_A^0 + U_A Q_A + \frac{1}{2} Y_A Q_A^2 \right) + \sum_{A \neq B} \frac{Q_A Q_B J_{AB}}{2} \tag{1.3.4a}$$

where E_A^0 is the energy of atom A in the uncharged state, $-eQ_A$ is the net charge on atom A, $U_A = \chi_A/2 + I_A/2$ is the Mulliken potential, $Y_A = I_A - \chi_A$ is the idem-potential, and $J_{AB} = e^2/\varepsilon_0 d_{AB}$ is the Coulombic interaction between two charges which are situated at atomic positions A and B. In the above, χ is the electron affinity, I is the ionization potential, and d_{AB} is the distance between atoms A and B. In thermal equilibrium, one can apply the condition that the chemical potential is a constant for all the atoms in the same molecule, and be able to estimate the charge transfer between atoms. This approach has yielded dipoles for small heteronuclear molecules in good quantitative agreement with experiment [81]. To apply the above method to a metal-semiconductor interface, the conglomerate of the entire metal-semiconductor region can be regarded as a giant "molecule." The truncated lattices of a metal and a semiconductor are assumed to form bonds on an atomically flat interface plane. A density of chemical bonds, N_B, is assumed to form across the metal-semiconductor interface. In general, N_B needs not equal, and is likely less than, the total number of semiconductor (or metal) atoms per unit area on each plane parallel to the interface. Lattice mismatch, structure incompatibility, interface mixing, the formation of tilted bonds, etc., all tend to reduce the number of effective bonds formed across a metal-semiconductor interface. Without loss of generality, we assume chemical bonds to form in a square array with a lateral dimension of $d_B = N_B^{-1/2}$. We can write a total energy equation for the entire metal-semiconductor system. For simplicity, we assume Q's to be nonzero only for those metal and semiconductor atoms on the immediate interface planes which are involved in the bonding. Furthermore, we keep only the interactions between charged atoms which are nearest neighbors.

$$\begin{aligned} E_{MS} = {} & \sum_i \left(E_M^0 + U_M Q_{M_i} + \frac{1}{2} Y_M Q_{M_i}^2 \right) + \sum_i \left(E_S^0 + U_S Q_{S_i} + \frac{1}{2} Y_S Q_{S_i}^2 \right) \\ & + \sum_i Q_{M_i} Q_{S_i} J_{MS} + \sum_{i,j}^{near.neigh} \left[J_{MM} Q_{M_i} Q_{M_j} + J_{SS} Q_{S_I} Q_{S_j} \right] \end{aligned} \qquad (1.3.4b)$$

Now we require the chemical potential of a metal atom at the interface, $\mu_{M_i} = \partial E_{MS} / \partial Q_{M_i}$, to equal that of a semiconductor atom, $\mu_{S_i} = \partial E_{MS} / \partial Q_{S_i}$. Because of symmetry, every bonded metal atom at the interface has the same net charge $-eQ_M$ and every semiconductor atom has a net charge of $+eQ_M$. One thus obtains

$$Q_M = \frac{U_S - U_M}{Y_M + Y_S + 4J_{MM} - 2J_{MS} + 4J_{SS}} , \qquad (1.3.4c)$$

where we have used the fact that there are four in-plane nearest neighbors. In the spirit of analyzing charge transfer between two crystals, rather than between atoms, we can let the atoms acquire bulk characteristics. For a bulk metal, the ionization potential and the electron affinity are both identified as the work function of the metal, φ_M. Thus, $U_M = \varphi_M$ and $Y_M = 0$. For a semiconductor, the ionization potential and the electron affinity, χ_S, differ by its band gap, E_g. Therefore, $U_S = \chi_S + E_g/2$ and $Y_S = E_g$. To account for the fact that the Coulombic interactions take place inside a solid, screening by the respective dielectric medium is also assumed. Equation (1.3.4c) becomes

$$Q_M = \frac{\varphi_M - \chi_S - E_g/2}{E_g + \kappa}, \qquad (1.3.4d)$$

where κ is the sum of all the hopping interactions, i.e., $\kappa = 4e^2/(\varepsilon_S d_B) - 2e^2/(\varepsilon_i d_{MS})$, and d_{MS} is the distance between metal and semiconductor atoms at the interface. The voltage drop across this interfacial dipole layer can now be calculated to be

$$V_{\text{int}} = \frac{-ed_{MS}N_B}{\varepsilon_i}\frac{(\varphi_M - \chi_S - E_g/2)}{E_g + \kappa} \qquad (1.3.4e)$$

where V_{int} is related to SBH (φ_{Bn}) as

$$\varphi_{Bn} = \varphi_M - \chi_s + eV_{\text{int}}, \qquad (1.3.4f)$$

Combining Eqs. (1.3.4e) and (1.3.4f), one gets

$$\varphi_{Bn} = \left[1 - \frac{e^2 d_{MS} N_B}{\varepsilon_i (E_g + \kappa)}\right](\varphi_M - \chi_S) + \frac{e^2 d_{MS} N_B}{\varepsilon_i (E_g + \kappa)}\frac{E_g}{2}, \qquad (1.3.4g)$$

$$\varphi_{Bn} = \gamma_B(\varphi_M - \chi_S) + (1 - \gamma_B)\frac{E_g}{2}, \qquad (1.3.4h)$$

$$\text{where} \quad \gamma_B = 1 - \frac{e^2 d_{MS} N_B}{\varepsilon_i (E_g + \kappa)}$$

Equation (1.3.4h) predicts a dependence of the SBH on the metal work function which is similar to that predicted by interface state models, Eq. (1.3.1i).

In Eq. (1.3.4h), the dielectric constant of the interface region, ε_i, should have a value somewhere between the dielectric constant of the semiconductor, ε_∞, and that of the metal, $\varepsilon_M (= \infty)$. A simple average ($\varepsilon_i^{-1} = \varepsilon_M^{-1}/2 + \varepsilon_\infty^{-1}/2$) leads to an estimate of 2 ε_∞. Here the optical dielectric constant is used because the charge transfer occurs between the semiconductor and the metal, so there should be little ionic contribution to the screening. A plot between experimentally observed slope parameter S in the form of $[\varepsilon_\infty(1-S)]^{-1}$ and band gap of the semiconductor [82] is shown in Fig. 1.3.4a. According to Eq. (1.3.4h), the quantity plotted in Fig. 1.3.4a is $2\varepsilon_0 (E_g + \kappa)/(ed_{MS}N_B)$, which should display a linear behavior if d_{MS}, N_B, and κ do not vary appreciably with semiconductors. Indeed, a roughly linear relationship is observed, which approximately extrapolates through the origin, suggesting that, due to screening, κ is small compared with typical band gaps. A slope of ~0.13 eV^{-1} is deduced from a linear fit, which yields a $d_{MS}N_B$ of ~9 × 10^6 cm^{-1}.

Taking d_{MS} to be 2.5 Å, one gets an N_B of $\sim 4 \times 10^{14}$ cm^{-2} which is a very reasonable estimate of the number of available bonds on a typical semiconductor surface. The polarization of the chemical bonds at the metal-semiconductor interface leads to a weak dependence of the SBH on the work function and a natural tendency for the SBHs to converge toward one-half of the band gap, both of which are in agreement with experimental results. Even though the present theory seems to have captured the essence of the SBH formation mechanism, it is only an approximation and should not be regarded as numerically accurate. For numerical comparison with SBH experiments, one should always rely on first principles calculations for a more accurate treatment of the interface dipole.

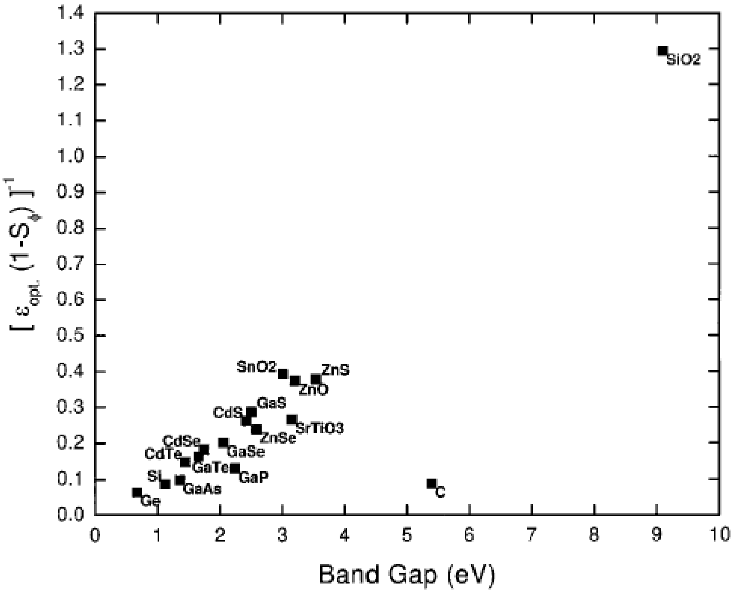

Figure 1.3.4a: *Experimentally observed slope parameters S [82] are used to plot the quantity* $[\varepsilon_\infty(1-S)]^{-1}$ *against the semiconductor band gap,* E_g.

Chapter 2

Methodology

In this chapter we provide a brief discussion of the fundamental equations to describe the systems of interacting electrons and nuclei; and the fist principle methods based on the density functional theory (DFT) [83, 84]. Density functional theory is the most widely used method to calculate the electronic structure of the materials. In particular, we present the plane wave implementation, using ultrasoft pseudopotentials [85] and plane augmented wave (PAW) method [86]. Furthermore, we also discuss the reciprocal space formalism with the use of special k-points, a level broadening technique, the supercell technique for the non-periodic systems and calculation of surface energies, work functions, elastic constants and SBH from first principle methods. A more extensive and detailed discussion of the fundamental techniques and their details can be found in a large number of textbooks and review articles [87-92].

2.1 *Ab-initio* calculations

The objective of *ab-initio* methods is to calculate physical properties of materials without using any experimental input. These calculations from first principles provide the macroscopic properties of a given physical system just from the knowledge of the type and position of the atoms. In particular, using the atomic structure as the only input, the electronic, mechanical, magnetic and optical properties of a condensed matter system can be obtained.

2.1.1 Fundamental equations for interacting electrons and nuclei

Unarguably, the fundamental equations to describe the matter are based on general methods of quantum mechanics and statistical mechanics. The starting point for the theoretical description of any system of electrons and nuclei is the general many body Hamiltonian of the system. Any material or solid can be described as an ensemble of electrons and nuclei which are coupled by coulomb interactions. Denoting the nuclear coordinates by $R := \{R_I \mid I = 1, \ldots N_n\}$, the electronic coordinates by $r := \{r_i \mid i = 1, \ldots N_e\}$ and the conjugate momenta P and p , the Hamiltonian of the system can be written as

$$\hat{H} = \hat{T}_n(P) + \hat{T}_e(p) + \hat{V}_{nn}(R) + \hat{V}_{ee}(r) + \hat{V}_{ne}(R,r) \qquad (2.1.1a)$$

where T_n and T_e are the kinetic energy operators for the nuclei and the electrons. While V_{nn} , V_{ee} and V_{ne} are the coulomb interaction operators respectively. If we adopt Hartree atomic units $\hbar = m_e = e = 4\pi/\varepsilon_0 = 1$, then the operators in the Hamiltonian can be written as

$$\hat{T}_n = -\sum_I \frac{\hbar^2}{2M_I}\nabla_I^2 \quad , \quad \hat{T}_e = -\sum_i \frac{\hbar^2}{2m_e}\nabla_i^2 \quad , \quad \hat{V}_{nn} = \frac{1}{2}\sum_{I \neq J} \frac{Z_I Z_J e^2}{|R_I - R_J|} \quad ,$$

$$\hat{V}_{ee} = \frac{1}{2}\sum_{i \neq j} \frac{e^2}{|r_i - r_j|} \quad , \quad \hat{V}_{ne} = \frac{1}{2}\sum_{i,I} \frac{Z_I e^2}{|r_i - R_I|} \; ;$$

In principle, all the properties of the solid can be described if an exact solution of the many body stationary Schrodinger equation, in terms of many body wavefunction Ψ(r,R)

$$H\Psi(r,R) = E\Psi(r,R) \qquad (2.2.1b)$$

can be obtained. Once Ψ(r,R) is known, expectation value of any observable can be obtained as $\left\langle \hat{O} \right\rangle = \dfrac{\left\langle \Psi \mid \hat{O} \mid \Psi \right\rangle}{\langle \Psi \mid \Psi \rangle}$, where O is an general observable operator .

Then, exact electron density n(r) and ground state energy E can be determined as

$$n(r) = \frac{\left\langle \Psi \mid \hat{n}(r) \mid \Psi \right\rangle}{\langle \Psi \mid \Psi \rangle}; \qquad E = \frac{\left\langle \Psi \mid \hat{H} \mid \Psi \right\rangle}{\langle \Psi \mid \Psi \rangle}$$

where, $\hat{n}(r) = \sum_{i=1,N} \delta(r - r_i)$ is the charge density operator.

However, in reality, it is extremely difficult to solve this equation exactly, even with the best available computer resources. Hence, there arises need to simplify the equation with some justifiable approximations without losing desired accuracy in the final results.

2.1.2 Born-Oppenheimer or adiabatic approximation

A first approximation is justified by the fact, that the nuclei are more than three orders of magnitude heavier than electrons. As a consequence, the time scale of the nuclear motion is orders of magnitude larger than that of the electronic motion. Thus it can be assumed that the electrons are always in their instantaneous ground state determined by the external potential of the nuclei, and that the forces acting on the nuclei are determined by the instantaneous electronic distribution and the nuclear positions of the system. The electrons are considered to be dependent merely on the nuclear positions and not on their velocities. This assumption first introduced by Born and Oppenheimer [93], is known as the adiabatic approximation. Therein, the ionic momenta are assumed to be vanishingly small and the ion positions are taken as fixed external parameters and the ionic part of the Hamiltonian is represented by a fixed external potential.

$$V_{ext}(r) = \frac{1}{N_e} V_{nn}(R) + V_{ne}(r, R),$$

which leads to the following Hamiltonian for the electron system:

$$H_e(r) = -\frac{\hbar^2}{2m} \sum_{i=1}^{N_e} \nabla_i^2 + \frac{1}{2} \sum_{i \neq j} \frac{e^2}{|r_i - r_j|} + \sum_{i=1}^{N_e} V_{ext}(r_i) \quad (2.1.2a)$$

The separation mentioned above between electronic and ionic degrees of freedom is very advantageous since it allows one to treat the ionic degrees of freedom classically while the electrons are to be treated quantum mechanically.

2.2 Density functional theory

Density functional theory [83, 84] is a theory of correlated many-body systems. It has provided the key step that has made possible development of practical, useful independent-particle approaches that incorporate effects of interactions and correlations among particles. As such, density functional theory has become the primary tool for calculation of electronic structure in condensed matter, and is increasingly important for quantitative studies of molecules and other finite systems. The remarkable successes of the approximate local density (LDA) and generalized-gradient approximation (GGA) functionals within the Kohn-Sham approach have led to widespread interest in density functional theory as the most promising approach for accurate, practical methods in the theory of materials. In the following section, we present briefly the fundamental concepts of DFT. For a more extensive treatment, see [90, 91, 92].

2.2.1 Hohenberg-Kohn theorems

The approach of Hohenberg and Kohn [83] is to formulate density functional theory as an exact theory of many-body systems. The formulation applies to any system of interacting particles in an external potential $V_{ext}(r)$, including any problem of electrons and fixed nuclei, where the Hamiltonian can be written as equa. (2.1.2a). Density functional theory is based upon two theorems first proved by Hohenberg and Kohn. The first theorem states that, for any system of interacting particles in an external potential $V_{ext}(r)$, the potential $V_{ext}(r)$ is determined uniquely, except for a constant, by the ground state particle density $n_0(r)$. Since the Hamiltonian is thus fully determined, except for a constant shift of the energy, it follows that the many-body wavefunctions for all states (ground and excited) are determined. Therefore, all properties of the system are completely determined given only the ground state density $n_0(r)$. According to the second theorem, a universal functional for the energy $E[n]$ in terms of the density n(r) can be defined, valid for any external potential $V_{ext}(r)$. For any particular $V_{ext}(r)$, the exact ground state energy of the system is the global minimum value of this functional, and the density $n(r)$ that minimizes the functional is the exact ground state density $n_0(r)$. The Hohenberg-Kohn energy expression for any fully interacting many body system can be written as a functional of density n(r).

$$E_{HK}[n] = T[n] + E_{\text{int}}[n] + \int d^3 r V_{ext}(r) n(r) + E_{II} \qquad (2.2.1a)$$

Where $T[n]$ and $E_{\text{int}}[n]$ are the kinetic energy and interaction energy functional and are the universal functional by construction. E_{II} is the interaction energy of the nuclei.

2.2.2 Kohn-Sham equations

The Kohn-Sham approach [84] is to replace the difficult interacting many-body system obeying the Hamiltonian (2.1.2a) with an auxiliary independent-particle system that can be solved more easily. The Hamiltonian of this auxiliary system is written as

$$H_{aux} = -\frac{-\hbar^2}{2m_e}\nabla^2 + V_{eff}(r) \;; \qquad (2.2.2a)$$

Where $V_{eff}(r)$ is the effective potential seen by an independent electron in the system due to remaining electrons and nuclei. In this approach, the Hohenberg-Kohn expression of ground state energy functional (2.2.1a) is written as,

$$E_{KS} = T_s[n] + \int d^3 r V_{ext}(r) n(r) + E_{Hartee}[n] + E_{II} + E_{XC}[n] \qquad (2.2.2b)$$

Here, $n(r)$, $T_s[n]$, $V_{ext}(r)$, E_{Hartee}, and E_{II} are the electron density, independent-particle kinetic energy, external potential due to nuclei and any other external fields, classical Coulomb interaction energy of the electron density $n(r)$ and interaction energy of the nuclei, respectively. E_{xc} is called the exchange-correlation energy and has all the many-body effects due to exchange and correlation effects in it. If the system has N independent electrons obeying equa.(2.2.2a), with the ground state having one electron in each of the N orbitals $\psi_i(r)$ with the lowest eigenvalues ε_i of the Hamiltonian, then one can write expressions for electron density, kinetic energy and Hartree energy as

$$n(r) = \sum_{i-1}^{N} |\psi_i(r)|^2 \;;\; T_s = \frac{1}{2}\sum_{i=1}^{N} |\nabla \psi_i|^2 \;;\; E_{Hartree}[n] = \frac{1}{2}\int d^3 r d^3 r' \frac{n(r)n(r')}{|r - r'|} \qquad (2.2.2c)$$

The solution of the Kohn-Sham auxiliary system for the ground state is obtained by minimizing the energy functional (2.2.2b) with respect to the density n(r). Since $T_s[n]$ is explicitly expressed as a functional of orbitals but all other terms are considered to be functional of the density, one can also vary the wavefunctions and use the chain rule to derive the variational equation;

$\frac{\delta E_{KS}}{\delta \psi_i^*(r)} = 0$, subject to the orthonormalization constraints $\langle \psi_i | \psi_j \rangle = \delta_{ij}$.

This leads to the Kohn-Sham Schrodinger-like equations:

$$(H_{KS} - \varepsilon_i)\psi_i(r) = 0, \qquad (2.2.2d)$$

where the ε_i are the eigenvalues, and H_{KS} is the effective Hamiltonian

$$H_{KS}(r) = -\frac{\hbar^2}{2m}\nabla^2 + V_{KS}(r),$$

$$\text{with } V_{KS}(r) = V_{ext}(r) + V_{Hartree}(r) + V_{XC}(r)$$

Equations (2.2.2d) are well known Kohn-Sham equations, with the resulting density $n(r)$ and total energy E_{KS} given by 2.2.2b. The equations have the form of independent-particle equations with a potential that must be found self-consistently with the resulting density. These equations are independent of any approximations to the function $E_{xc}[n]$, and would lead to the exact ground state density and energy for the interacting system, if the exact functional $E_{xc}[n]$ were known. The Kohn-Sham equations have to be solved self-consistently since $V_{Hartree}$ and V_{xc} depend explicitly on the charge density $n(r)$, given by the eigenstates ψ_i, which in turn are determined by these potentials. In order to turn this into practice, an initial guess, e.g. a superposition of atomic charges, is used. On the basis of the eigenfunctions of (2.2.2d), the new charge density is obtained by summing over the occupied Kohn-Sham orbitals ψ_i. Afterwards, the Hartree and exchange-correlation potentials are then constructed. This process has to be repeated until convergence is reached. In practice the new charge density is mixed with previous one in order to avoid numerical instabilities. Figure 2.2.2a gives a schematic overview of the iterative algorithm.

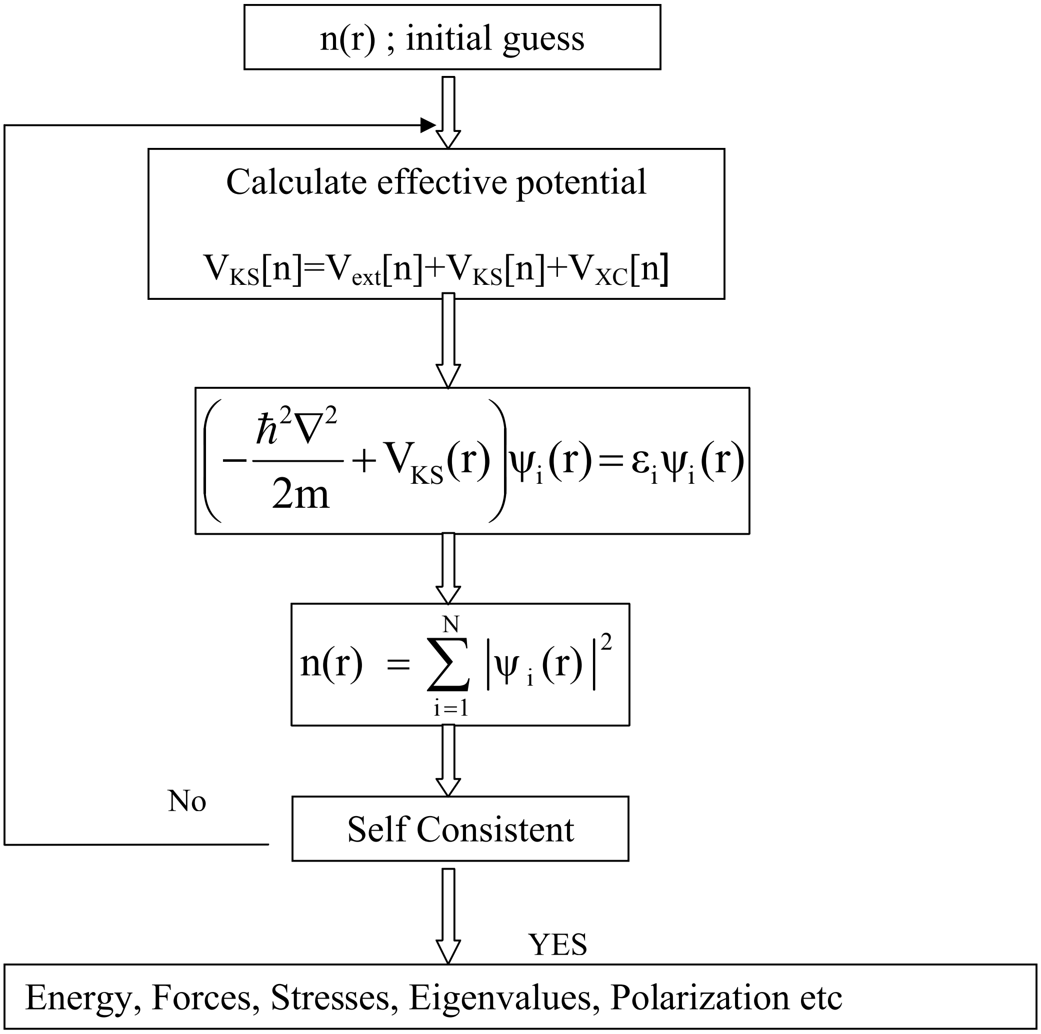

Figure 2.2.2a*: Flowchart of self-consistent Kohn-Sham calculation.*

Once the effective potential and the charge density become self consistent, forces on the each ion can be calculated using Hellmann-Feynman [94, 95] theorem. Afterwards, ions can be optionally moved towards their classical equilibrium positions by minimizing the effective forces on them. In this way equilibrium geometry of the unit cell can be determined.

2.2.3 Local density approximation

In order to solve Kohn-Sham equations, one needs to define exchange-correlation potential. Even though the exact exchange-correlation functional must be very complex, great progress has been made with remarkably simple approximations. The most simple and popular approximation to exchange-correlation functional is the local density approximation [96]. In this approximation, the exchange-correlation energy is simply an integral over all space with the exchange-correlation energy density at each point assumed to be same as in a homogeneous electron gas with that density.

$$E_{XC}^{LDA}[n] = \int d^3 r n(r) \varepsilon_{xc}^{\hom}[n(r)] \qquad (2.2.3a)$$

The exchange-correlation energy $\varepsilon_{XC}^{\hom}[n(r)]$ of a homogeneous electron gas has been calculated by Ceperley and Alder [97] for various densities using quantum Monte-Carlo simulations. Perdew and Zunger [98] have parameterized their results in order to approximate $\varepsilon_{XC}^{\hom}[n(r)]$ over a wide rage of densities. This procedure is exact if and only if the density n(r) is constant. If $n(r)$ varies slowly over distances of the order of the Fermi wavelength, LDA can be expected to provide a good approximation. On the other hand, at crystalline surfaces or for atoms and molecules, where the electronic density varies rapidly, the validity of LDA appears to be questionable. Practice shows however, that LDA yields adequate ground-state properties even for strongly inhomogeneous systems.

2.2.4 Generalized-gradient approximation (GGA)

The first step beyond the local approximation is functional of the magnitude of the gradient of the density as well as the value *n* at each point. In GGA, the functional is written as a generalized form of the LDA expression:

$$E_{XC}^{GGA}[n] = \int d^3 r n(r) \varepsilon_{XC}(n, |\nabla n|, ...) \equiv \int d^3 r n(r) \varepsilon_{X}^{\hom}(n) F_{XC}(n, |\nabla n|, ...)$$

Where F_{xc} is dimensionless and $\varepsilon_{xc}^{\hom}$ (n) is the exchange energy of the unpolarized gas. Numerous forms for $F_{xc}(n)$ have been proposed. Some of the frequently forms used routinely are, Perdew and Wang (PW91) [99] and Perdew, Burke, and Enzerhof (PBE) [100].

2.2.5 Discussion

At this point we want to stress that DFT is a ground state theory and that the Kohn-Sham eigenvalues ε_i have strictly speaking no physical significance and in particular, they do not coincide with quasi-particle excitation energies of the real system. However, it has become standard practice to interpret the ε_i as estimates of quasi-particle energies and compare them in solids with experimental band structures. In order to obtain better approximations of excitation energies, e.g. semiconductor band gaps, a Green's function based approach, which is known as the *GW* approximation, is generally used [101, 102]. Concerning LDA, we mention that it has some systematic errors. Specifically, it underestimates semiconductor and insulator band gaps. Furthermore the description of cohesive energies, weak bonds and of the exchange-correlation potential in the vacuum region outside surfaces, are generally qualitatively not very accurate. An improvement over LDA is the semi-local Generalized Gradient Approximation (GGA) which not only considers the charge density n, but also its gradient Δn. Moreover, it uses non-local exchange-correlation functionals.

2.3 Application to atomic systems (bulk, surfaces, interfaces etc.)

In the following, we provide a brief overview of the method generally used to solve the Kohn-Sham equations for condensed matter systems. For crystalline systems, it is highly beneficial to consider periodic boundary conditions which allow one to expand the problem into a plane wave basis set, which is highly efficient for a numerical solution. At first sight, this seems not applicable to surfaces or interfaces, where the three-dimensional bulk symmetry is broken in one spatial direction. However, as we will discuss later in this section interfaces and surfaces can be investigated with the supercell technique without loosing the advantages of the plane wave approach.

2.3.1 Plane Wave expansion

Using the Bloch theorem [103], we represent the eigenfunctions $\psi_{n,k}$ (r) of the Kohn-Sham equations as a product of a lattice periodic function $u_{n,k}$ (r) and a plane wave with a wave vector k belonging to the first Brillouin zone (BZ):

$$\Psi_{n,\mathbf{k}}(r) = u_{n,\mathbf{k}}(r)\, e^{i\mathbf{kr}} \qquad (2.3.1a)$$

where n is the band index. Since the $u_{n,k}$ are by definition lattice periodic, they can be expanded into plane waves:

$$u_{n,k}(r) = \sum_{G'} \varphi_{n,k}(G')e^{iG'r} \qquad (2.3.1b)$$

Where, G are the reciprocal lattice vectors. For practical purposes the sum in (2.3.1b) is restricted to plane waves with kinetic energy below a given cutoff energy E_{cut}. Thus, defining the set $\Omega(G)$:

$$\Omega(G) := \left\{ G \left| \frac{\hbar^2}{2m} \right| k + G \right|^2 \leq E_{Cut} \right\} \qquad (2.3.1c)$$

we obtain the following expansion of the Kohn-Sham wavefunctions:

$$\psi_{n,k}(r) = \sum_{G \in \Omega(G)} \varphi_{n,k}(G) e^{i(G+r)} \qquad (2.3.1d)$$

The cutoff energy E_{cut} controls the numerical convergence relative to the completeness of the basis set. It depends strongly on the elements which are present in the system under investigation. The plane wave expansion allows very efficient momentum space formalism [104]. The Fourier coefficients $\varphi_{n,k}(G)$, obtained by the diagonalization of the Hamiltonian matrix, contain all relevant information and allow one to calculate all physical properties of interest, as e.g. the total energy, the Hellmann-Feynman [94, 95] forces and the stresses [105, 106]. Also the Poisson equation, which defines the Hartree potential, can be easily solved in reciprocal space.

2.3.2 Pseudopotential approximation

Plane waves, which form a convenient and efficient basis set for the diagonalization of the Hamiltonian, have an essential drawback: they are very efficient in representing slowly varying functions, but they are not suitable to describe the fast oscillations of electron wave functions in the core region. In order to overcome this problem the pseudopotential approximation [107-111] is often used in conjunction with the plane wave expansion. It exploits the fact that core electrons belonging to closed inner shells are tightly localized around their nucleus and do not contribute to inter-atomic chemical interactions. Apart from some exceptions, only valence electrons are influenced by neighboring atoms. Consequently, they determine the chemical properties. This feature is the basis of the frozen core approximation used in quantum chemistry. In the pseudopotential approximation, the influence of core electrons on the valence states is described by an effective potential. The reduction to the description of only valence electrons is an essential prerequisite in order to describe large systems containing several hundred atoms.

Many different schemes have been proposed for constructing pseudopotentials. An extensive review can be found in Ref. [108]. In the norm-conserving, *ab initio* pseudopotentials proposed by Troullier and Martins [112], following properties are fulfilled:

1. The lowest energy valence pseudo wave-functions generated from the pseudopotential do not contain nodes.
2. The eigenvalues associated with the exact and the pseudo wave-functions are equal.
3. Beyond a certain cutoff radius r_c, the atomic pseudo wavefunctions coincide with the exact wave functions obtained by an atomic calculation, where all electrons are taken into account.
4. The charge of the pseudo wavefunctions contained in a sphere of radius r_c equals that of the exact wavefunction.

The quality and transferability, i.e. the independence of the pseudopotential on the given system, are controlled by the choice of the cutoff radius. A small value of r_c corresponds to a high transferability but requires a high energy cutoff to obtain a sufficient numerical convergence. However, r_c has to be larger than the outermost node of all core electron wave-functions in order to fulfill the norm-conserving criterion 3. In general, the generation of 'good' pseudopotentials, i.e. a good compromise between a sufficient smoothness of wavefunctions and a good transferability is a time demanding task. The Troullier-Martins pseudopotentials V^{TM} can be separated into a local part V^{loc} , i.e. solely dependent on the distance *r*, and a non-local part V_l^{nloc} which depends on the orbital momenta *l* of the electronic pseudo wavefunctions:

$$V^{TM}(r) = V^{loc}(r) + \sum_{l,m} \left| Y_{l.m} \right\rangle V_l^{nloc}(r) \left\langle Y_{l,m} \right|$$

Where, Y_{lm} are the spherical harmonics. In the plane wave expansion with *N* plane waves, the matrix elements thus depend on *G* and *G'* and their evaluation therefore scales as N^2. Kleinman and Bylander [113] proposed to transform the non-local components into a form which allows one to factorize entirely the plane wave integrals:

$$V^{KB} = V^{loc} + \sum_{l.m} \frac{\left| \delta V_l \Phi^0_{lm} \right\rangle \left\langle \Phi^0_{lm} \delta V_l \right|}{\left\langle \Phi^0_{lm} \mid \delta V_l \mid \Phi^0_{lm} \right\rangle}$$

where $\delta V_l = V^{loc} - V_l^{nloc}$ and $\Phi_{\mathrm{lm}}{}^0$ are the pseudo wave-functions obtained for V^{TM}. In this form, the evaluation of the matrix elements scales as *N* and not as N^2 as in the original form which is a significant improvement for large systems. However, the non-locality can give rise to *ghost* states [114] which have no physical meaning. By a convenient choice of the local part, the occurrence of ghost states can be avoided [115].

One goal of pseudopotentials is to create pseudofunctions that are as "smooth" a possible, and yet are accurate. For example, in plane wave calculations the valance functions are expanded in Fourier components, and he cost of the calculations scales as a power of the number of Fourier components needed in the calculation. Thus one meaningful of definition of maximizing "smoothness" is to minimize the range in the Fourier space needed to describe the valence properties to a given accuracy. "Norm-conserving" pseudopotentials achieve the goal of accuracy, usually at some sacrifice of "smoothness". In the "ultrasoft pseudopotential" approach, the goal of accurate calculations is achieved by a transformation that re-expresses the problem in terms of a smooth function and an auxiliary function around each ion core that represents the rapidly varying part of density. The transformation proposed by Vanderbilt [111] rewrites the non-local potential in a form involving a smooth function $\tilde{\phi} = r\tilde{\psi}$ that is not norm conserving. A new non-local potential that operates on the $\tilde{\psi}_s$ can now be defined to be

$$\delta \hat{V}_{NL}^{US} = \sum_{s,s'} D_{s,s'} |\beta_s\rangle\langle\beta_{s'}|,$$

where

$$D_{s,s'} = B_{s,s'} + \varepsilon_{s'} \Delta Q_{s,s'} \; ; \quad \Delta Q_{s,s'} = \int_0^{R_C} \Delta Q_{s,s'}(r)dr = \int_0^{R_C} \left(\phi_s^*(r)\phi_{s'}(r) - \tilde{\phi}_s^*(r)\tilde{\phi}_{s'}(r) \right) dr$$

For each reference atomic states s, it is straightforward to show that the smooth functions $\tilde{\psi}_s$ are the solutions of the generalized eigenvalue problem

$$\left[\hat{H} - \varepsilon_s \hat{S} \right] \tilde{\psi}_s = 0,$$

with $\hat{H} = -\frac{1}{2}\nabla^2 + V_{local} + \delta \hat{V}_{NL}^{US}$ and $\hat{S}$ an overlap operator,

$$\hat{S} = \hat{1} + \sum_{s,s'} \Delta Q_{s,s'} |\beta_s\rangle\langle\beta_{s'}|,$$

which is different from the unity inside the core radius. The eigenvalues ε_s agree with the all-electron calculation at as many energies *s* as desired. The full density can be constructed from the functions $\Delta Q_{s,s'}(r)$, which can be replaced by a smooth version of the all-electron density. The advantage of relaxing the norm-conserving condition $\Delta Q_{s,s'} = 0$ is that each smooth pseudopotential $\tilde{\psi}_s$ can be formed independently, with only the constraint of matching the value of the functions $\tilde{\psi}_s(R_c) = \psi_s(R_c)$ at the radius R_c. Thus it becomes possible to choose R_c much larger than for a norm-conserving pseudopotential, while maintaining the desired accuracy by adding the auxiliary functions $\Delta Q_{s,s'}(r)$ and the overlap operator *S*.

2.3.3 Projector augmented Wave (PAW) method

The projector augmented wave (PAW) method [116] is a general approach to solution of the electronic structure problem. The PAW approach keeps the full all-electron wavefunction. Since the full wavefunction varies rapidly near the nucleus, all integrals are evaluated as a combination of integrals of smooth functions extending throughout space plus localized contribution evaluated by radial integration over muffin-tin spheres. In PAW approach, one defines a smooth part of a valence wavefunctions $\tilde{\psi}_i^v(r)$ (a plane wave or an atomic orbital), and a linear transformation $\psi^v = T\tilde{\psi}^v$ that relates the set of all-electron valence functions $\psi_j^v(r)$ to the smooth functions $\tilde{\psi}_i^v(r)$. The transformation is assumed to be unity except with a sphere centered on the nucleus, $T = 1 + T_0$. For simplicity, we omit the superscript *v*, assuming that the ψ_s are the valence states, and the labels i, j. Adopting the Dirac notation, the expansion of each smooth function $\left|\tilde{\psi}\right\rangle$ in partial waves *m* within each sphere can be written,

$$\left|\tilde{\psi}\right\rangle = \sum_m c_m \left|\tilde{\psi}_m\right\rangle,$$

with the corresponding all-electron function,

$$\left|\psi\right\rangle = T\left|\tilde{\psi}\right\rangle = \sum_m c_m \left|\psi_m\right\rangle,$$

Hence the full wavefunction in all space can be written

$$\left|\psi\right\rangle = \left|\tilde{\psi}\right\rangle + \sum_m c_m \left\{\left|\psi_m\right\rangle - \left|\tilde{\psi}_m\right\rangle\right\},$$

If the transformation *T* is required to be linear, then the coefficients must be given by a projection in each sphere

$$c_m = \left\langle \tilde{p}_m \mid \tilde{\psi}\right\rangle,$$

for some set of projection operators satisfy the biorthogonality condition,

$$\left\langle \tilde{p}_m \middle| \tilde{\psi}_{m'}\right\rangle = \delta_{mm'},$$

then the one-center expansion $\sum \left| \tilde{\psi}_m \right\rangle \left\langle \tilde{p}_m \middle| \tilde{\psi} \right\rangle$ of the smooth functions $\tilde{\psi}$ equals $\tilde{\psi}$ itself.

The general form of the PAW equations can be cast in terms of transformation *T*. For any operator $\hat{A}$ in the original all-electron problem, one can introduce a transformed operator $\tilde{A}$ that operates on the smooth part of the wavefunctions

$$T = 1 + \sum_m \left\{ |\psi_m\rangle - \left| \tilde{\psi}_m \right\rangle \right\} \left\langle \tilde{p}_m \right|,$$

$$\tilde{A} = T^+ \hat{A} T = \hat{A} + \sum_{mm'} \left| \tilde{p}_m \right\rangle \left\{ \langle \psi_m | \hat{A} | \psi_{m'} \rangle - \left\langle \tilde{\psi}_m \middle| \hat{A} \middle| \tilde{\psi}_{m'} \right\rangle \right\} \left\langle \tilde{p}_{m'} \right|,$$

The expressions for physical quantities in the PAW approach follow from above two equations.

2.3.4 Brillouin zone integration

For many properties, such as the counting of electrons in bands, total energies, etc., it is essential to sum over the states labeled by *k*. The crucial point is that if one chooses the eigenfunctions that obey periodic boundary conditions in a large crystal of volume $\Omega_{crystal}$ composed of $N_{cell} = N_1 \times N_2 \times \ldots cells$, then there is exactly one value of *k* for each cell. Thus in a sum states to find an intrinsic property of a crystal expressed as “per unit cell” one simply ha a sum over values of *k* divided by the number of values N_k. For a general function $f_i(k)$, where *i* denotes any of the discrete set of states at each *k*, the average value per cell becomes

$$\bar{f}_i = \frac{1}{N_k} \sum_k f_i(k), \quad (2.3.4a)$$

The special property of insulators is that the integrals needed all have the form (2.3.4a) where the sum is over filled bands in the Brillouin zone (BZ). Since the integrand $f_i(k)$ is some function of the eigenfunctions $\psi_{i,\mathbf{k}}$ and eigenvalues $\varepsilon_{i,k}$, it is a smoothly varying, periodic function of *k*. Thus $f_i(k)$ can be expanded in Fourier components

$$f_i(k) = \sum_T f_i(T) e^{ikT}, \quad (2.3.4b)$$

where T are the translation vectors of the crystal. The most important point is that the contribution of the rapidly varying terms at large T decreases exponentially, so that the sum in (2.3.4b) cab be truncated to a finite sum. Special points are chosen for efficient integration of smooth periodic functions. The single most special point is Baldereschi point [117], where the integration reduces to a single point. The general method proposed by Monkhorst and Pack [118] is now the most widely used method because it leads to a uniform set of points determined by a simple formula valid for any crystal:

$$k_{n_1,n_2,n_3} \equiv \sum_i^3 \frac{2n_i - N_i - 1}{2N_i} G_i, \quad (2.3.4c)$$

where G_i are the primitive vectors of the reciprocal lattice.

Metals present an important class of issues for efficient sampling of the desired states in the BZ. The Fermi surface plays a special role in all properties and the integration over states must take into account the sharp variation of the Fermi function from unity to zero as a function of k. This plays a decisive role in all calculations of sums over occupied states for total quantities and sums over both occupied and empty states for response functions and special functions. In order to represent the Fermi surface, the tetrahedron method [119-121] is widely used. If the eigenvalues and vectors are known at a set of grid points, the variation between the grid points can always be approximated by an interpolation scheme using tetrahedra. This is particularly useful because tetrahedra can be used to fill all space for any grid. Tetrahedron methods are are very important in calculations on transition metals, rare earths, etc., where there are exquisite details of the Fermi surfaces that must be resolved.

2.3.5 Supercell technique

The formalism sketched above is very efficient for calculating the electronic properties of periodic systems. The systems investigated in this work, i.e. interfaces and surfaces lack periodicity in one direction. This drawback can be overcome considering periodically repeated thin slabs of alternating materials, i.e. artificial superlattices whose unit cells are called supercells. Depending on the materials and on the physical properties of interest, these supercells can reach large sizes and contain up to several hundred atoms. The supercell defines a unit cell with one axis perpendicular to the interface or surface of interest. The periodic repetition of the supercell leads to an artificial superlattice which allows one to model an interface if the slabs are sufficiently thick. The required thickness depends on the two materials forming the interface and on the physical quantities under investigation, i.e. the interaction between the two slab interfaces has to be sufficiently small. For each property we are interested in, as for example the Schottky barrier or the work function, the convergence has to be tested through several calculations with an increasing number of atomic layers in the slabs. Features related particularly to the finite slab thickness are known as quantum size effects. In this work we normally use 17 atomic layers for the semiconductor and up to 13 atomic layers for the metal, or vacuum, in the case of surfaces, respectively.

2.3.6 Band structure alignment and Schottky barriers

To understand the issues involved in the band-lineup problem, we consider two semiconductors, A and B, with different bandgaps E_g^A and E_g^B, and bring them together at an interface. Since the bandgap is discontinuous, it is clear that the valence and/or conduction bands will also be discontinuous, as illustrated in Fig. 2.3.6a. Note that the bands on either side of the interface are depicted as flat, corresponding to the notion that we are only interested in a region on the order of a few atomic distances around the interface, and that band bending is negligible on this length scale.

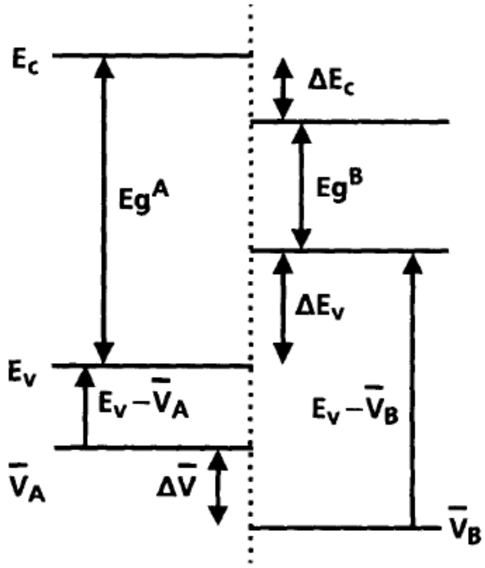

Fig. 2.3.6a: *Schematic illustration of the band structure lineup problem between semiconductors A and B. The positions of valence and conduction bands are indicated, all referred to their appropriate reference level* $\bar{V}$ *in each semiconductor. The distance between* $\bar{V}_A$ *and* $\bar{V}_B$ *determines the band lineup.*

Various theoretical methods are capable of calculating the band structure of a semiconductor; the interface problem amounts to finding a way to line up the two band structures across the interface. The band structure of semiconductor A can be calculated relative to a reference level (usually an average of the electrostatic potential) $\bar{V}_A$. Similarly, the band structure of semiconductor *B* is referred to a level $\bar{V}_B$. For instance, the position of the valence-band maximum, E_v , is a distance E_v - $\bar{V}$ above the position of the average electrostatic potential (see Fig. 2.3.6a). The band offset problem then consists of determining the difference in average electrostatic potentials between A and B, i.e. $\Delta\bar{V}$. The problem would thus be solved if we could determine the positions of the average electrostatic potentials inside A and B on an absolute energy scale, e.g. with respect to the vacuum level. It may seem that if one is able to carry out the band structure calculations for the two semiconductors, then the problem is solved, since these calculations will provide information about the position of $\bar{V}_A$ and $\bar{V}_B$. Unfortunately this is not so. The problem is that there is no absolute reference for the average potential in an infinite solid. This problem is caused by the long-range nature of the Coulomb interaction, which makes the average potential of an infinite system ill-defined [122]. The fact that the average potential in an infinite solid is ill-defined is often described associating single particle-energies with "removal energies". Since in an infinite system there is no "elsewhere" (e.g., a vacuum level) to remove an electron to, it would seem to follow that the single-particle energies in the infinite semiconductor cannot be put on an absolute energy scale. This argument is incomplete, if not wrong, as was pointed out by [123]. If the interactions were finite in range, the average potential inside a macroscopic but finite sample would actually not depend on the shape of the solid or surface effects, and would therefore have a well-defined thermodynamic limit. It is precisely the long range nature of the Coulomb interaction that causes the removal energies to depend on the detailed structure of the surface. Or, in the case of an interface, it is the long-range nature of the Coulomb interaction that causes the presence of a dipole at an interface to shift the energy levels throughout the semi-infinite solid on either side. It follows that a band structure calculation for an individual solid cannot provide information about the absolute position of the average potential. To calculate a band lineup, one has to obtain additional information about the behavior of the potentials in the neighborhood of the interface. This indicates that, at least *in principle,* the details of the atomic structure near the interface may affect the potentials far away and hence the band-lineup. We thus have to accept that when we study a bulk semiconductor, the average electrostatic potential inside the solid is not known on an absolute energy scale, but is defined only to within an arbitrary constant. This arbitrary constant can be fixed by making specific assumptions about the boundary conditions. In order to solve the heterojunction problem, an obvious approach is to specify the boundary condition to be exactly that at the semiconductor interface, i.e., to perform a calculation in which both semiconductors are present and joined at the junction. This ensures that the electrostatic potentials of both materials are expressed with respect to the same reference, and allows direct extraction of $\Delta \bar{V}$ and thus of the band discontinuities [124].

The mathematical approach used in the first principles calculations with in the framework of density function theory typically assumes periodicity. For an interface problem, periodicity can be maintained by considering a superlattice structure, in which layers of the two semiconductors are periodically repeated. Besides directly providing useful information about actual superlattice structures, this approach also yields results for isolated interfaces, provided the layers are sufficiently thick to ensure adequate separation between adjacent interfaces. Experience has shown that to extract band offsets layers of eight to sixteen atoms thick typically are sufficient; charge densities and potentials indeed typically converge quite rapidly to their bulk value away from the interface. It is then possible to identify a "bulk-like" region in the middle of each superlattice layer, where the value of an average potential can be determined. For the purpose of deriving the band-lineup, we are only interested in the behavior of the potential as we move perpendicular to the interface; the remaining two coordinates can be eliminated by averaging in planes parallel to the interface:

$$\bar{V}(z) = \frac{1}{S}\int_S V(x, y, z)dxdy\,, \qquad (2.3.6a)$$

where *S* represents the area of a unit cell in the plane of the interface. We are then left with a one-dimensional function, which still exhibits periodic variations in the direction perpendicular to the interface. This function rapidly recovers its bulk behavior in each of the two materials comprising the junction as one moves away from the interface; however, the positions of the average potentials in the bulk-like regions are shifted with respect to one another, providing exactly the quantity $\Delta \bar{V}$ that we needed to obtain the band-lineup. Indeed, separate bulk calculations for the two semiconductors can be carried out, providing information about individual band positions with respect to the average potential $\bar{V}$. This procedure for obtaining band offsets is actually similar to that followed empirically in X-ray photo spectroscopy (XPS) determinations of the offsets. In XPS, typically, the separation between two representative core levels is measured across the interface; independent measurements on bulk samples are performed to obtain the energy separation between the valence-band maximum and the core levels in each material. The core level separation is then used to line up the valence bands and obtain the band offsets. All-electron calculations can actually mimic this approach, and provide information about core-level lineups as well as band offsets [125]. Pseudopotential calculations cannot directly provide core level lineups, since the core electrons are removed from the problem. However, using average potentials for the lineup is very similar in spirit. It is important to acknowledge that in density-functional theory the calculated eigenvalues do not necessarily correspond to quasiparticle energies. A well known consequence of this deficiency is the failure of density-functional theory to produce the correct band gaps. It is therefore important to realize that corrections beyond density-functional theory may be necessary to obtain the exact band positions (with respect to the average electrostatic potential). We also note, however, that the calculated potential lineup term ($\Delta\bar{V}$) depends only on the charge density of the heterojunction, and as such is a ground-state property that is reliably given by density-functional theory. The corrections to LDA are therefore limited to the positions of the quasiparticle energy levels that are obtained in bulk calculations for the individual materials. Quasiparticle calculations of this nature have been carried out for a wide variety of semiconductors [126]; by comparing the results with LDA band structures, it was found that the average LDA error in the heterojunction valence-band offset was about 120 meV. However, these errors do not enter if one is only interested in *changes* in the band offsets (induced by changes in the interfacial composition and structure), which will only affect the potential-lineup term.

Important information about the heterojunction interface can also be obtained from the qualitative and quantitative discussion of an interface dipole which is defined properly. One definition that is often used, in particular in connection with first-principles pseudopotential calculations, is the following [127]: suppose one takes the difference between the charge density at the interface (obtained from a supercell calculation, and averaged in planes parallel to the interface), and the charge density in the bulk (similarly averaged). One can then use Poisson's equation to calculate a dipole. The dipole, however, is not unique, since it depends critically on where the mathematical surface representing the interface is chosen. The location of the interface determines that on one side, the bulk charge density of semiconductor *A* will be subtracted, and on the other side that of semiconductor *B*. A different choice of the "mathematical" interface can produce a very different dipole. In addition, comparison between different interface orientations makes little sense with this definition. The bottom line is that the concept of interface dipole is best avoided, unless one specifies explicitly which definition is being used, and uses the concept only to identify trends between situations which are sufficiently similar (e.g., same interface orientation) to allow a meaningful comparison. The issue of defining an interface dipole can be appropriately addressed with the technique of macroscopic averaging [128]. Usually, the microscopic potentials and charge densities around an interface fluctuate with a periodicity imposed by the lattice. Concepts such as the discontinuity in average potentials are actually defined on a macroscopic scale, since they involve the difference in potential on either side of the junction, and far away from the interface. These macroscopic quantities can conveniently be extracted by filtering out the microscopic oscillations, which is most easily accomplished by averaging the microscopic quantities over a volume corresponding to the unit cell. Looking at a heterojunction, we know that the average potential will undergo a shift as one passes through the interface from one semiconductor to the other. The shift in the average potential is actually a macroscopic quantity, since it can be observed in measurements far away from the junction. On a microscopic level, however, the potential looks very complicated because it exhibits a periodic variation on the atomic scale. This periodic variation is actually irrelevant for the macroscopic quantity (the potential-lineup) that we are interested in, and we would like to "filter out" these rapid fluctuations in the potential, and only take into account the variation on longer length scales. This type of filtering is a familiar concept in classical electromagnetism for instance in the theory of dielectric polarization. We already know that to extract dipoles and lineups we may perform an average of the potential in planes parallel to the interface, as defined in Eq. (2.3.6a). The quantity ($\bar{V}$) is a one-dimensional function, which still exhibits periodic variations in the direction perpendicular to the interface. For any microscopic quantity $f^{(micro)}(r)$ one can define a macroscopic average $f^{(macro)}(r)$:

$$f^{(macro)}(\vec{r}) = \int w(\vec{r} - \vec{r}\,')f^{(micro)}(\vec{r}\,')dr' , \quad (2.3.6b)$$

where *w(r)* is a properly chosen filter function depending on the geometry and on the characteristics length scale of the problem. Acting directly on the planer average, the filter function can be chosen simply as

$$w(z) = \frac{1}{a}\Theta\left(\frac{a}{2} - |z|\right), \quad (2.3.6c)$$

where Θ is the one-dimensional step function, giving

$$\bar{\bar{V}}(z)) = \frac{1}{a}\int_{z-a/2}^{z+a/2} \bar{V}(z')dz', \qquad (2.3.6d)$$

where *a* is the length of one period in the direction perpendicular to the interface. The same procedure can be applied to the charge density. The lineup is related to the dipole moment of the charge profile:

$$\Delta\bar{V} = \frac{e^2}{\varepsilon_0}\int z\left[\bar{\bar{n}}(z) - n_0\right]dz, \qquad (2.3.6e)$$

where n_0 is the average electronic density of the two bulk materials. This provides an unambiguous definition of the interface dipole, without having to make any assumption about the nature of the interface. The macroscopic average defined above relied on the fact that the periodicity of the microscopic variations would be the same on both sides of the interface. This assumption obviously is not satisfied in the case of an interface between lattice-mismatched semiconductors. Nevertheless, the macroscopic average technique can also be applied between two materials A and B with different periodicities because of lattice mismatch or even structural differences. In order to recover macroscopic features in the bulk regions of both materials, one has to filter twice, using the functions w_A and w_B appropriate to each material in turn. This double filtering can be recast in terms of the single filter function

$$w(r) = \int w_A(\vec{r} - \vec{r}\,')w_B(\vec{r}\,')dr' \ , \qquad (2.3.6f)$$

Often, one is not interested in the absolute magnitude, but in changes in the interface dipole, brought about by some modification of the interface (e.g., the presence of an interlayer), while the semi-infinite bulk materials on either side remain unmodified. The experimentally measured change in the band offset can then be directly associated with a change in the interface dipole. It is then the task of theoretical analysis to try and ascribe this change to a particular modification of the electronic structure, and in the process of doing so care should be taken in the definition and calculation of any interface dipole.

In supercell calculations, the band offset or Schottky barrier can also be evaluated directly from the local density of states (LDOS) *N(ε, z)* defined as

$$N(\varepsilon, z) = \sum_{k,n} \bar{\bar{\rho}}_{k,n}(z)\delta(\varepsilon - \varepsilon_k) \ , \quad (2.3.6g)$$

where the sum runs over the bands *n* and the wavevectors *k* of the BZ of the supercell, $\rho_{k,n}(\vec{r}) = |\psi_{k,n}(\vec{r})|^2$ and $\psi_{k,n}(\vec{r})$ is the electronic wavefunction. Far from the interface, on each side of the junction, the LDOS *N(ε,z)* converges to the bulk density of states of the corresponding crystal. The band offset or Schottky barrier can be obtained thus from the difference between the band edges of the LDOS on the two sides, far from the junction. The LDOS, however, requires supercell computations with a high number of *k* points and a large energy cut-off compared with those needed to determine the charge density and the potential line-up. In addition, larger supercells have to be used, since the LDOS has a spatial convergence to the bulk features slower than that of the charge density. As a result, the LDOS approach is less convenient, in general, than the potential-line-up approach to determine the band discontinuities.

2.3.7. Thermodynamics of surfaces and calculation of surface energies

In order to predict the stability of surfaces under realistic experimental conditions [129], it is necessary to consider the nature of the experiments in order to decide which quantities should be determined from the *ab initio* calculations. So long as the surface is in equilibrium with its surroundings, the stability may be determined following standard thermodynamics [130] from the free energy and the chemical potential μ_i of each type of atom '*i*'. The chemical potentials take into account the fact that the numbers of atoms are conserved in reactions at the surface, so that changes in the total free energy of the system when a constituent atom is interchanged between the surface and a reservoir can be determined. By incorporating the appropriate chemical potentials, we can take into account different experimental conditions and predict the stability of different surface structures. This approach is clearly appropriate when the surface is in equilibrium with the bulk and other relevant reservoirs. However, there may be other cases in which the reactions are not in equilibrium and may be governed by rate limiting kinetic factors.

The chemical potential μ_i is defined to be the derivative of the Gibbs free energy $G = E+PV-TS$ for a given phase with respect to the number of particles of type i: $\mu_i = dG/dn_i$ [130]. Since in equilibrium the chemical potential μ_i of a given atomic species is the same in all its phases which are in contact, each μ_i can be considered as the free energy per particle in each reservoir for *i*. For the condensed state (e.g., GaAs surfaces, bulk GaAs, or bulk Ga or As), the Gibbs free energy is the total energy at zero temperature plus a negative definite temperature dependent term which involves a simple integral of the specific heat [130]. The *PV* term is completely negligible for pressure considered here. Although the temperature dependent term can be included in principle, we ignore it in the present work for the following reasons. First, it is not feasible to calculate the entropies of the various bulk and surface states. Second, the temperature dependent terms tend to cancel for the relevant differences between the free energies of condensed states so that their contributions are small. Third, this approximation has been implicit in all the recent (rather successful) density functional work calculating phase transitions using only the energy at $T = 0$. Thus, for condensed phases, we ignore the temperature dependence and set the chemical potential μ equal to the total energy *E* per atom calculated at $T = 0$.

For gaseous phases, on the other hand, the effect of *T* and *P* upon the chemical potential cannot be ignored. As is well known in gas theory [130], μ depends logarithmically upon the chemical potential *T* and *P* and the large variations in μ can be used to control the state of the condensed phases in equilibrium with the gas. In general, the function $\mu_i(P, T)$ is complicated but can in principle be determined experimentally for any gas. Nevertheless, even without a detailed knowledge of the chemical potentials as a function of *P* and *T*, we can establish ranges for $\mu_i(P, T)$ which are relevant for the determination of the surface structures under equilibrium conditions. Although the gas expressions alone permit any value of the μ_i, there are limits on the allowable range in equilibrium with all possible phases. In particular, the chemical potential for each element cannot be above that of the bulk elemental phase. It may equal the bulk chemical potential (in which case there is in general bulk material present and the surface is in equilibrium with the elemental condensed bulk phase) or it may be below the bulk chemical potential (in which case the bulk is not stable and the surface is in equilibrium with a gaseous phase).

In addition, the bulk solid *AB* is a reservoir which can exchange atoms with the surface. If the surface is in equilibrium with the bulk, pairs of *A* and *B* atoms can be exchanged with the bulk, for which the energy is the total bulk energy pair. This requires that the sum of the μ_i for *A* and *B* equal the bulk energy per pair. It is useful to note that the bulk energy may be equated to the sum of the energies of bulk *A* and bulk *B* minus the heat of formation ΔH_f. (Note that this requirement on the sum of the chemical potentials is modified if one accounts for the fact that the bulk can exchange unpaired *A* or *B* atoms by creating defects. This effect may be large at very elevated temperature but is not relevant under usual growth conditions and temperatures where the small number of bulk defects do not cause gross changes in the surface stoichiometry.) Thus equilibrium with the bulk leads to the relation

$$\mu_A + \mu_B = \mu_{AB(bulk)} = \mu_{A(bulk)} + \mu_{B(bulk)} - \Delta H_f$$

Finally, making use of the above limits on the individual μ_i set by the bulk elements, one finds that the surface can be in equilibrium with its surrounding only if the chemical potentials are within both upper and lower limits:

$$\mu_{B(bulk)} - \Delta H_f \le \mu_B \le \mu_{B(bulk)},$$

$$\mu_{A(bulk)} - \Delta H_f \le \mu_A \le \mu_{A(bulk)},$$

The equilibrium state of the surface as a function of composition is determined by minimizing the function

$$G_{surface}(n_i) - \sum_i \mu_i n_i \approx E_{surface}(n_i) - \sum_i \mu_i n_i$$

Here $G_{surface}(n_i)$ is the surface free energy as a function of the variable composition and the approximate equality above amounts to replacing G by the total surface energy $E(n_i)$ at $T = 0$.

2.3.8 Elastic Constants

The elastic constants determine the stiffness of a crystal against an externally applied strain. For small deformations, we expect a quadratic dependence of the crystal energy E on the strain (Hooke's law). The elastic constants c_{ijkl} describe this quadratic behavior. Consider a displacement $u(R)$ which takes every Bravais lattice point R of the undistorted lattice to a new position R' in the strained lattice,

$$R_i' = R_i + u_i(R), \qquad (2.3.8a)$$

where the index i corresponds to Cartesian coordinates. If we assume the applied strain is homogeneous (uniform throughout the crystal), we can rewrite (2.3.8a) as

$$R_i' = \sum_j \alpha_{ij} R_j \text{ with } \alpha_{ij} = \delta_{ij} + \frac{\partial u_i(R)}{\partial R_j} \qquad (2.3.8b)$$

For a homogeneous applied strain the displacement gradients $\partial u_i(R)/\partial R_j$ are simply constants, independent of R. These displacement gradients define the nine components of a tensor. However, since the total energy E cannot change under rotations of the crystal as a whole, E can only depend on the symmetric part of the deformation, [131] called the strain tensor ε:

$$\varepsilon_{ij} = \frac{1}{2}\left[\frac{\partial u_i(R)}{\partial R_j} + \frac{\partial u_j(R)}{\partial R_i}\right] \qquad (2.3.8c)$$

Expanding the internal energy $E(V,\varepsilon)$ of the crystal with respect to the strain tensor gives[132]

$$E(V,\{\varepsilon_{mn}\}) = E(V) + V\sum_{ij}\sigma_{ij}\varepsilon_{ij} + \frac{V}{2}\sum_{ijkl} c_{ijkl}\varepsilon_{ij}\varepsilon_{kl} + ..., \qquad (2.3.8d)$$

where the stress tensor σ is defined by

$$\sigma_{ij} = \frac{1}{V}\left[\frac{\partial E(V,\{\varepsilon_{mn}\}}{\partial \varepsilon_{ij}}\right]_{\varepsilon=0}, \qquad (2.3.8e)$$

the second order adiabatic elastic constants are given by

$$c_{ijkl} = \frac{1}{V}\left[\frac{\partial^2 E(V,\{\varepsilon_{mn}\})}{\partial\varepsilon_{ij}\partial\varepsilon_{kl}}\right]_{\varepsilon=0} \qquad (2.3.8f)$$

and V is the volume of the unstrained crystal. It is convenient to use Voigt notation which takes advantage of the symmetries of the tensors: $xx \rightarrow 1$, $yy \rightarrow 2$, $zz \rightarrow 3$, $yz \rightarrow 4$, $xz \rightarrow 5$, and $xy \rightarrow 6$. Using this notation (2.3.8d) becomes [1311]

$$E(V,\{e_i\}) = E(V) + V\sum_i \sigma_i e_i + \frac{V}{2}\sum_{ij} c_{ij} e_i e_j + \ldots\ldots\ldots\ldots \qquad (2.3.8g)$$

with the strain tensor given by

$$\varepsilon = \left| \begin{array}{ccc} e_1 & e_6/2 & e_5/2 \\ e_6/2 & e_2 & e_4/2 \\ e_5/2 & e_4/2 & e_3 \end{array} \right|$$

In order to calculate all M elastic constants of a crystal, M independent strains $\varepsilon^{(I)}$ to the unit cell are applied, using (2.3.8b) and (2.3.8e) to determine the atom positions within the strained unit cell. For instance, there are M=3 for cubic Si, Ge and Ni, M=6 and M=9 for orthorhombic NiGe. Each strain I = 1, . . . ,M is parameterized by a single variable γ and the total energy $E^{(I)}$ (γ) is calculated for a number of small values of γ . For these small distortions, $E^{(I)}$ (γ) is fit to a polynomial in γ and then equated to the appropriate elastic constant expression $E(V,\{e_i^{(I)}(\gamma)\})$ in (2.3.8g). From all of the fits, a system of M linear equations for the elastic constants are obtained, which are then solved for the c_{ij}. Since the undistorted crystal is generally taken to be the zero-pressure theoretical equilibrium structure, the applied stress σ is zero and so the second term of (2.3.8d) and (2.3.8g) does not enter in the calculations described here.

The parameterizations used for the three independent strains in the cubic cases of Ni and Ge are given in Table 2.3.8a. Strain I =1 is a volume-conserving stretch along the z axis, the second strain is equivalent to simple hydrostatic pressure, and strain I = 3 corresponds to a volume-conserving monoclinic shear about the *z* axis. Calculations for nine values of γ in the range of -0.01 to 0.01 are carried out for strains 1 and 2. However, for strain 3, nine points in the range from -0.04 to 0.04 are calculated because the changes in the energy were rather small (a maximum of 0.1 mRy for γ = 0.01), leading to larger error estimates in the case of the smaller range. Orthorhombic NiGe has nine independent elastic constants and the nine strains listed in Table 2.3.8b are chosen. For each of the silicide strains, calculations for seven values of γ in the range of -0.01 to 0.01 are carried out.

Strain I	Parameters(unlisted e_i)	$\Delta E/V$ to $O(\gamma^2)$
1	$e_1 = e_2 = \gamma,\ e_3 = (1+\gamma)^{-2}-1$	$3(c_{11}-c_{12})\gamma^2$
2	$e_1 = e_2 = e_3 = \gamma$	$3/2\ (c_{11}+2\ c_{12})\gamma^2$
3	$e_6 = \gamma,\ e_3 = \gamma^2(4-\gamma^2)^{-1}$	$1/2\ (c_{44}\gamma^2)$

Table 2.3.8a: *Parameterizations of the three strains used to calculate the three elastic constants of cubic Ni and Ge. The energy expressions were obtained from (2.3.8g). Strains I = 1 and I = 3 are strictly volume-conserving to all orders in the strain parameter* γ*. If we restrict ourselves to linear order only then* $e_3^{(1)} = -2\gamma$ *and* $e_3^{(3)} = 0$*, with volume conservation preserved to linear order as well.*

Strain I	Parameters(unlisted $e_i = 0$)	$\Delta E/V$ to $O(\gamma^2)$
1	$e_1 = \gamma$	$1/2\ (c_{11}\gamma^2)$
2	$e_2 = \gamma$	$1/2\ (c_{22}\gamma^2)$
3	$e_3 = \gamma$	$1/2\ (c_{33}\gamma^2)$
4	$e_1 = 2\gamma,\ e_2 = -\gamma,\ e_3 = -\gamma$	$1/2(4c_{11} - 4c_{12} - 4c_{13} + c_{22} + 2c_{23} + c_{33})\gamma^2$
5	$e_1 = -\gamma,\ e_2 = 2\gamma,\ e_3 = -\gamma$	$1/2(c_{11} - 4c_{12} + 2c_{13} + 4c_{22} - 4c_{23} + c_{33})\gamma^2$
6	$e_1 = -\gamma,\ e_2 = -\gamma,\ e_3 = 2\gamma$	$1/2(c_{11} + 2c_{12} - 4c_{13} + c_{22} - 4c_{23} + 4c_{33})\gamma^2$
7	$e_4 = \gamma$	$1/2\ (c_{44}\,\gamma^2)$
8	$e_5 = \gamma$	$1/2\ (c_{55}\,\gamma^2)$
9	$e_6 = \gamma$	$1/2\ (c_{66}\,\gamma^2)$

Table 2.3.8b*: Parameterizations of the nine strains used to calculate the nine elastic constants of orthorhombic NiGe. The energy expressions were obtained from (2.3.8g).*

Chapter 3

Electronic structure, surface energies and work functions of PtSi

Metal silicides are used in complimentary metal-oxide-semiconductor (CMOS) devices to form ohmic contacts with source, drain, and gate silicon because of their low resistivity, low contact resistance to Si, reasonable thermal stability, and excellent process compatibility with standard Si technology. Over the past two decades, silicides of Ti, Co and Ni have been successively used in integrated circuit manufacturing. In the deep submicron regime NiSi is now succeeding $CoSi_2$. However, both $CoSi_2$ and NiSi exhibit large (0.5-0.6 eV) Schottky barriers to Si, in addition, NiSi suffers from low thermal stability. This contact resistance already amounts to a quarter of the total parasitic resistance, and will clearly only rise as scaling continues. Recently, PtSi has been found promising to form p-type low resistance contact with Si. It has relatively low (0.2 eV) Schottky barrier on Si (001) and has excellent thermal stability. With the aid of density functional theory we study electronic structure, surface energies, and work functions of PtSi. We also calculate Schottky barrier height (SBH) at Si(001)/PtSi(001) interface. The rest of the chapter is organized as follows. In the next section, we review the bulk properties of PtSi. In section 3.2, we report the comprehensive study of surface energetics and relate it to available data. In section 3.3, we discuss the work functions for several PtSi orientations, and in section 3.4 we report an estimate of the Schottky-barrier height at the Si(001)/PtSi(001) interface.

3.1 Crystal and electronic structure of bulk PtSi

PtSi crystallizes in the primitive orthorhombic structure in a MnP type lattice with space group *Pnma (# 62 in the International X-Ray Tables)* [128, 129] (see Fig.3.1a). In the standard setting experimental lattice constants are a=5.922 Å, b=5.575 Å and c=3.586 Å. Contrary to references [130] and [131] who used c=5.922 Å, we use the standard setting. There are four symmetry-equivalent Pt and four symmetry equivalent Si atoms per primitive orthorhombic cell. There are also four internal in plane parameters, u_{Si}, v_{Si}, u_{Pt}, v_{Pt} for Si and Pt atoms.

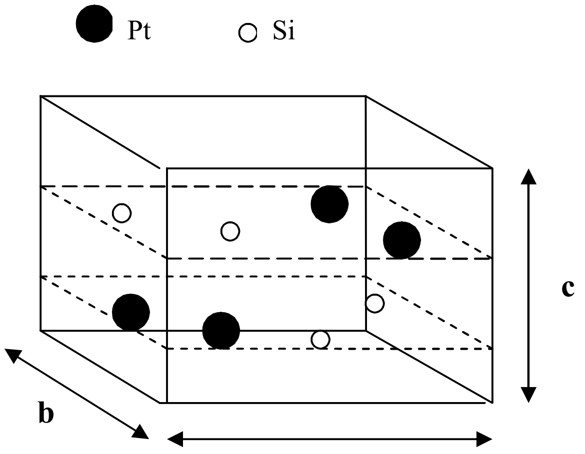

Figure 3.1a: *The orthorhombic unit cell of bulk PtSi. Lattice constants and free internal in plane coordinates are given in Table 3.1a and 3.1b.*

Material		a (Å)	b (A)	C (A)	E_{coh} (eV/atom)	ΔH_f (eV/atom)	Ref.
Pt	theo.	3.973			5.77		
	exp.	3.927			5.84		132
PtSi	theo.	5.986	5.648	3.635	5.84	-0.67	
	exp.	5.922	5.575	3.586	5.85	-0.62	133
Si	theo.	5.466			4.61		
	exp.	5.428			4.63		132

Table 3.1a: *Theoretical and experimental lattice constants (in Å); heat of formations (in eV/atom); cohesive energy (in eV/atom). The experimental standard heat of formation is given for T=298.15 K.*

PtSi	u_{Pt}	v_{Pt}	u_{Si}	v_{Si}	Ref
Experiment	0.1922	0.9956	0.583	0.177	133
Theory	0.1936	0.9945	0.5835	0.1784	

Table 3.1b: *Experimental and calculated free internal in plane coordinates of PtSi. The Pt atoms are located at [u_{Pt}, v_{Pt}, 1/4], [(1/2 -u_{Pt}), (v_{Pt}, – 1/2), 1/4], [(1-u_{Pt}), (1-v_{Pt}), 3/4,] and [(1/2+u_{Pt}), (3/2 –v_{Pt}), 3/4]. While the Si atoms are located at [u_{Si}, v_{Si}, 1/4], [(3/2-u_{Si}), (1/2 + v_{Si}), 1/4], [(u_{Si}-1/2), (1/2-v_{Si}), 3/4] and [(1-u_{Si}), (1-v_{Si}), 3/4].*

Density functional calculations [83, 84] were done using the projected augmented wave (PAW) [86] pseudopotentials as implemented in the VASP [134] code. The PBE form [100] of the generalized gradient approximation (GGA) for exchange and correlation was employed. A standard plane wave basis set was used with the kinetic energy cut off of 350 eV. We used a 16x16x24 k-point mesh in the orthorhombic cell for the Brillouin zone integration. The calculations are converged to 10^{-6} eV/cell and the structure was relaxed until the forces were less than 0.01 eV/Å per atom. Experimental and calculated PtSi lattice constants and internal in plane parameters are given in Tables 3.1a and 3.1b, respectively. In general the agreement between theory and experiment is very good. The caption to Table 3.1b gives the atomic positions in terms of the internal parameters

Energy bands along the high symmetry directions in the Brillouin zone in a 12 eV window around the Fermi level are shown in Fig. 3.1b. In Fig. 3.1c we show the total density of states of PtSi, and in Figures 3.1d and 3.1e, we show the partial density of states projected onto Pt and Si atoms, respectively. It is clear that the states at the Fermi level are derived predominantly from the *5d* orbitals of Pt. Also it is evident that Pt *5d* orbitals are not localized but extend throughout the entire valence band as has been originally pointed out by Beckstein *et al*. [131]. When compared to the total density of states of bulk Pt metal (shown in Fig. 3.1f) the density of states at the Fermi level in the silicide is five times lower, suggesting that PtSi is a poor metal. Note that the Fermi level in PtSi "misses" the high density region of the 5*d*-orbital manifold. This is due to the fact that the volume density of *d*-orbitals in the silicide is almost factor of two lower than that in Pt, while the silicide retains 70% of the electrons per unit volume. This results in a lower work function for PtSi, as we will show later. Our results for the electronic structure of PtSi are consistent with the experimental results [130] and with theoretical calculations previously reported [130,131].

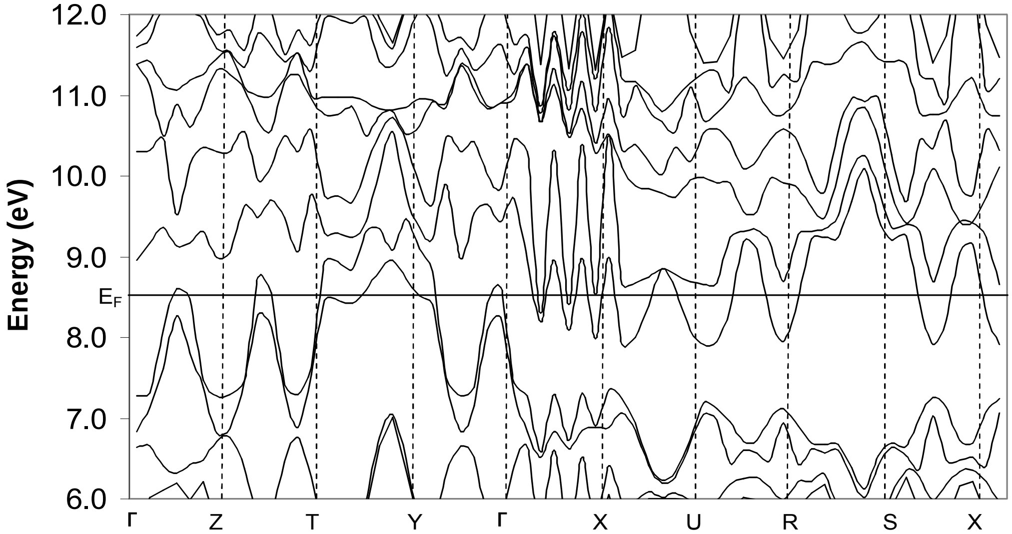

Figure 3.1b: *Band energies at the high symmetry k-points in the Brillouin zone for bulk PtSi.*

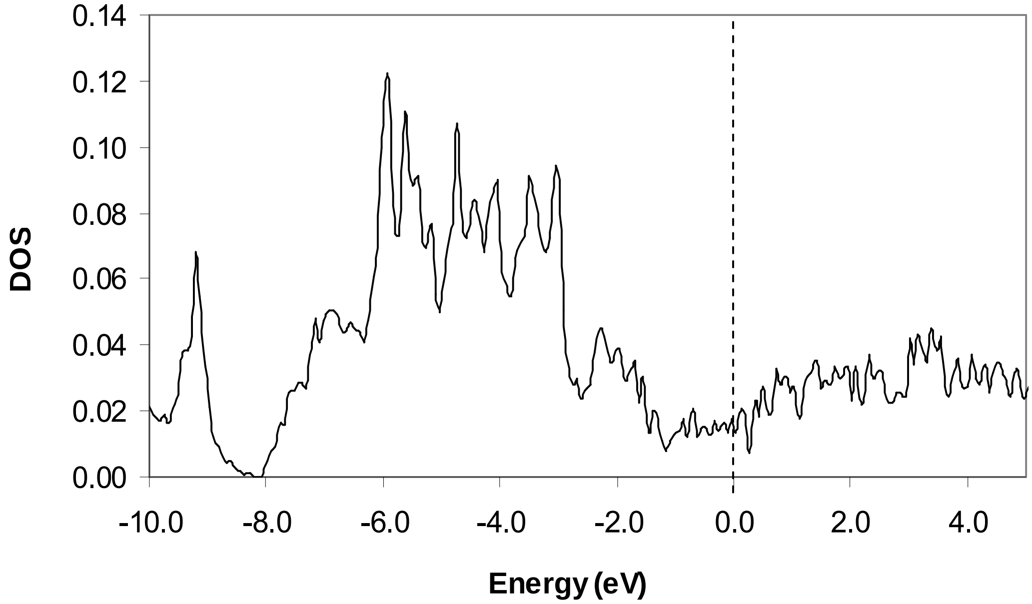

Figure 3.1c: *The density of states of PtSi (in electrons per Å^3 per eV). Fermi energy is indicated by the dashed line.*

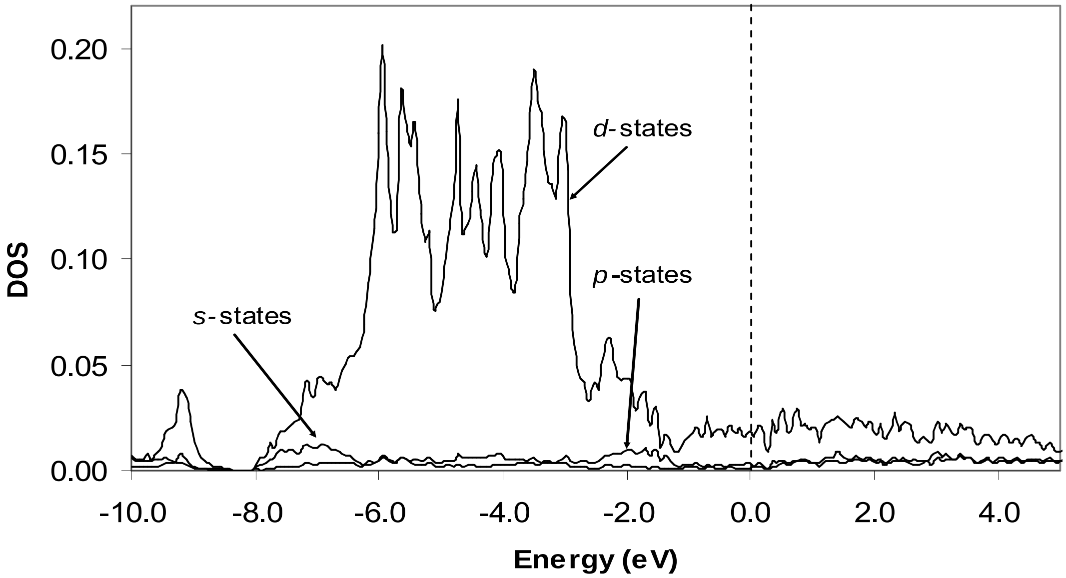

Figure 3.1d: *The density of states in PtSi (in electrons per Å^3 per eV) site projected on Pt atoms.*

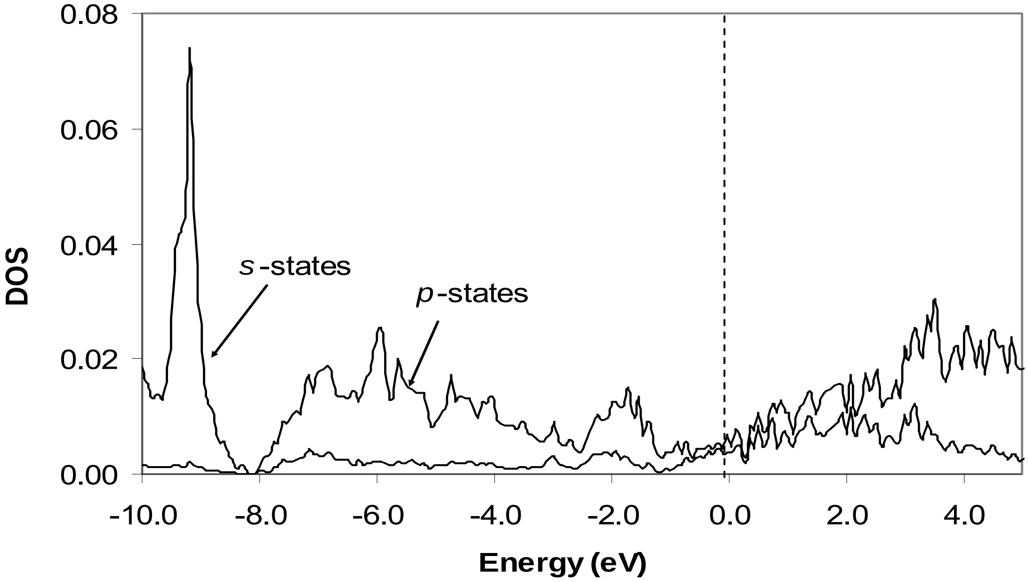

Figure 3.1e: *Projected density of states (in electrons per Å^3 per eV) of Si in PtSi.*

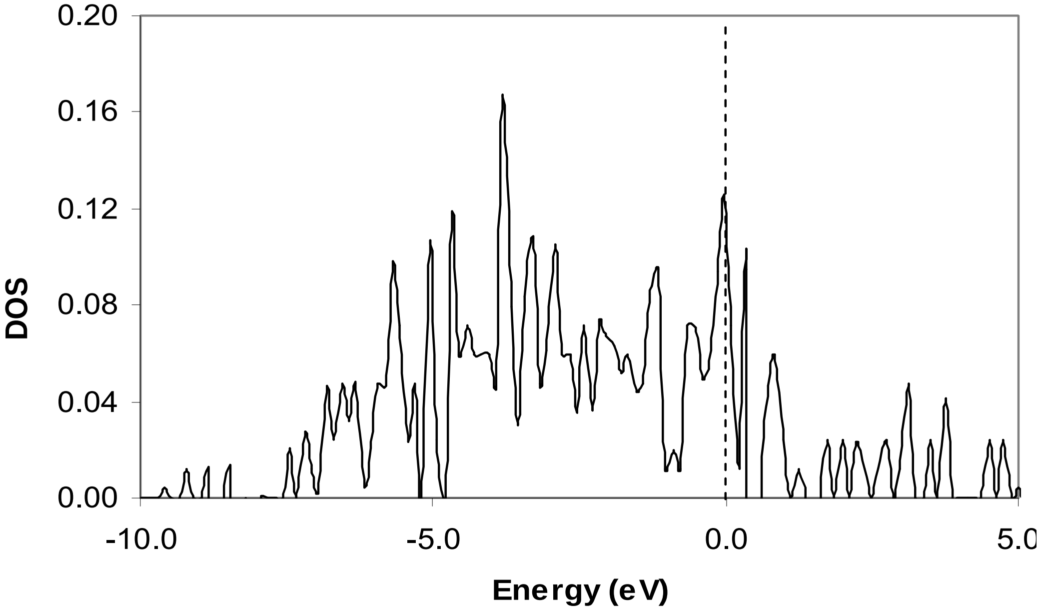

Figure 3.1f: *Density of states (in electrons per Å^3 per eV) of bulk Pt.*

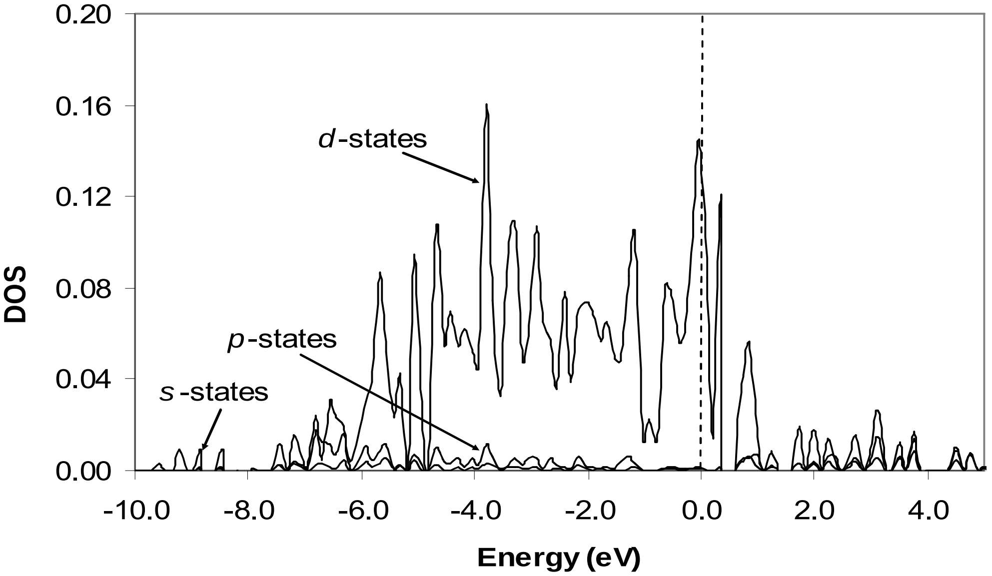

Figure 3.1g: *The density of states in Pt projected onto Pt sites (in electrons per Å^3 per eV).*

3.2 Surface energies of different PtSi surface orientations

We investigate surface energies for (110), (112), (001), (022), (211), (020), (121), (130), (111), (310), (202), (101), and (200) terminations of bulk PtSi. Calculations are done with supercells in a slab geometry (See section 2.3.5 on supercells). Symmetric slabs based on (1×1) surface cells for each termination are used (the lateral lattice constant is fixed to that derived from the calculated bulk value). Due to a relatively large cell size a moderate 4×4×1 k-mesh is employed for the Brillouin zone integration. We have checked the convergence with (6x6x1) and (8x8x1) grids, the energy changes are of the order of 10^{-4} eV/atom. Each supercell is relaxed until the forces reach 0.02 eV/Å or less.

We try to maintain the thickness of all slabs at about 17-20 Å which translates into ten to seventeen layers. The smallest (001)-oriented slab contains 44 atoms; the largest (130)-oriented slab contains 73 atoms. For example, to simulate the PtSi(001) surface, we use eight layers of vacuum over eleven layers of PtSi(001) (shown in Figure 3.2a).

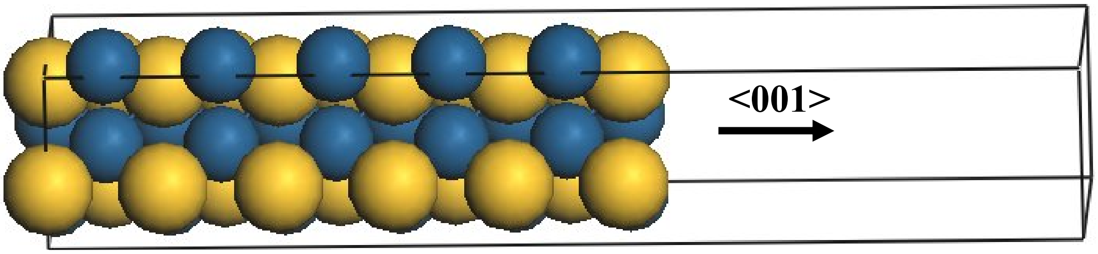

Figure 3.2a: *The Simulation cell for the (001)-oriented PtSi surface slab. Larger light balls are Si atoms, and smaller dark balls are Pt atoms.*

The dimensions of the rectangular surface unit cell are 5.99 Å by 5.65 Å. The PtSi (001)-1×1 surface cell has two Si and two Pt atoms. The unreconstructed surface can be described as zig-zag PtSi chains running along the shorter cell edge with two alternating PtSi intra-chain distances of 2.56Å and 2.44Å. Notice that surface Si atoms in adjacent chains are separated by only 3.456 (compare to 3.84 Å 2nd neighbor distance on the unreconstructed Si (001) surface). We define the rumpling parameter δr_i as in Ref. [135],

$$\delta r_i = (Z_i^{Pt} - Z_i^{Si}) / d_o,$$

Where Z^{Pt} and Z^{Si} are the z coordinates of the Pt and Si atoms in the *i*th layer and d_0 is the bulk interlayer distance (Fig. 3.2b). The results for surface rumpling are presented in Table 3.2a. To measure the average effect of the relaxation on the inter-planar distance in the direction normal to the slab surface, we define the plane position as the average z coordinate of the Pt and Si atoms. Thus in the bulk the inter-planar distance is 1.85 Å. After the relaxation the distance between the top and second layer increased by 5.6 %; the other inter-planar distances stay practically unchanged. In addition, we observe relatively large in-plane atomic displacements in the first two surface layers. The Pt and Si atoms on the first surface layer are displaced by 0.07 Å and 0.11 Å, respectively (see Fig. 3.2c). We did not consider the possibility of a more complex surface relaxation in a larger surface cell.

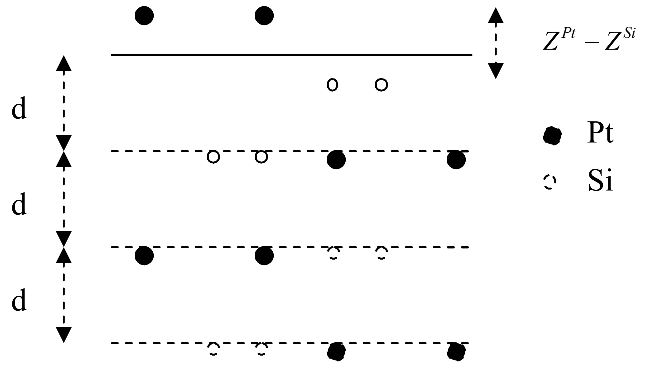

Figure 3.2b: *PtSi (001) surface (side view). Top four layers are shown.*

	δr_1	δr_2	δr_3	δr_4
Calc.	11.5	1.5	1.9	0.8

Table 3.2a: *Surface rumpling in % for PtSi (001) surface.*

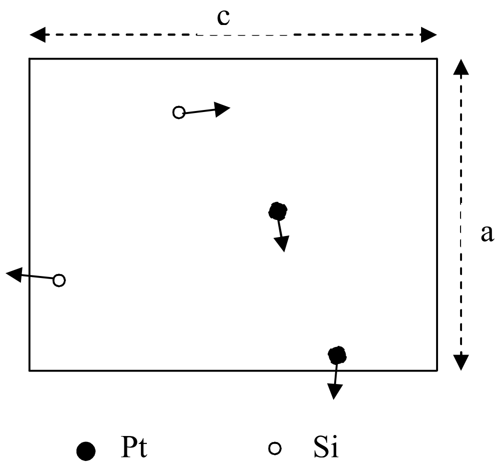

Figure 3.2c: *Top view of the first plane of PtSi (001) surface. Displacements of the atoms after the relaxation are indicated by the arrows.*

The surface energy of a PtSi surface is estimated using the Gibbs free energy approach [136] (see section 2.3.7 on surface energy). This technique allows for comparison of structures containing different number of atoms and is convenient if more than one atomic species is considered. Physically the need for a thermodynamic approach is rooted in the fact that only the energy of a molecular unit (PtSi in our case) rather than an atom (Pt or Si) can be defined in a compound. The surface free energy is given by:

$$E = \tfrac{1}{2}\left(E_{Slab} - N_{Si} \times E_{Si} - N_{Pt} \times E_{Pt} - N_{Si} \times \mu_{Si} - N_{Pt} \times \mu_{Pt}\right); \qquad (3.2e)$$

Here the energy is given per unit surface cell, and a factor of ½ is inserted to account for two surfaces in the supercell. E_{Slab} is the total energy of the supercell, while E_{Si}, and E_{Pt} are the energies per atom of bulk Si and Pt, respectively. N_{Si} and μ_{Si} are the number of Si atoms and Si chemical potential. Likewise, N_{Pt} and μ_{Si} are the number of Pt atoms and Pt chemical potential. Measuring chemical potentials of Pt and Si with respect to their bulk phases and assuming the surface is in equilibrium with bulk PtSi (thus μ_{Si} and μ_{Pt} are related by the equilibrium condition: $\mu_{Si} + \mu_{Pt} = -E_{form}$ (PtSi)), the surface energy can be written as follows:

$$E = \tfrac{1}{2}\left(E_{Slab} - N_{Si} \times E_{Si} - N_{Pt} \times E_{Pt} + N_{Si} \times E_{form} + \mu_{Pt} \times (N_{Si} - N_{Pt})\right); \qquad (3.2f)$$

The surface energies of different PtSi surfaces are tabulated in Table 3.2b. In Fig. 3.2d we show surface energies of different PtSi terminations as a function of the Pt chemical potential. The zero value of the chemical potential corresponds to Pt rich conditions, beyond that point metallic Pt will start forming on the surface. The range is bound by the PtSi formation energy, Si would start forming on the surface should this value be exceeded. As can be seen from Figure 3.2d, under Pt rich conditions the (211) surface is stabilized, after the chemical potential value reaches -0.8 eV the (110) surface orientation is most stable. Note, that since it is a stoichiometric surface the energy is independent of the chemical potential. The reactive growth of silicide on Si does occur under Si rich conditions, and an orthorhombic PtSi(110) peak is always reported [137-139]. On the other hand (200) which is the highest energy surface considered in this paper, is usually barely noticeable above the noise level in powder diffraction spectra. Overall, we find PtSi to have average surface energy, for comparison the surface energy of 2x1-reconstructed (001) Si is 1700 erg/cm^2 [140]. The most important observation, however, is that under Si rich conditions while (110) is still the lowest energy surface, several terminations such as (112), (001), (022), and (211) are very close in energy, and are only 200 erg/cm^2 higher. Indeed, these are the orientations most commonly reported in the literature [137-139]. Thus it appears that thermodynamics plays at least as important a role as kinetics most during the silicide formation. This is an important result, since it suggests a possibility of controlled silicide growth.

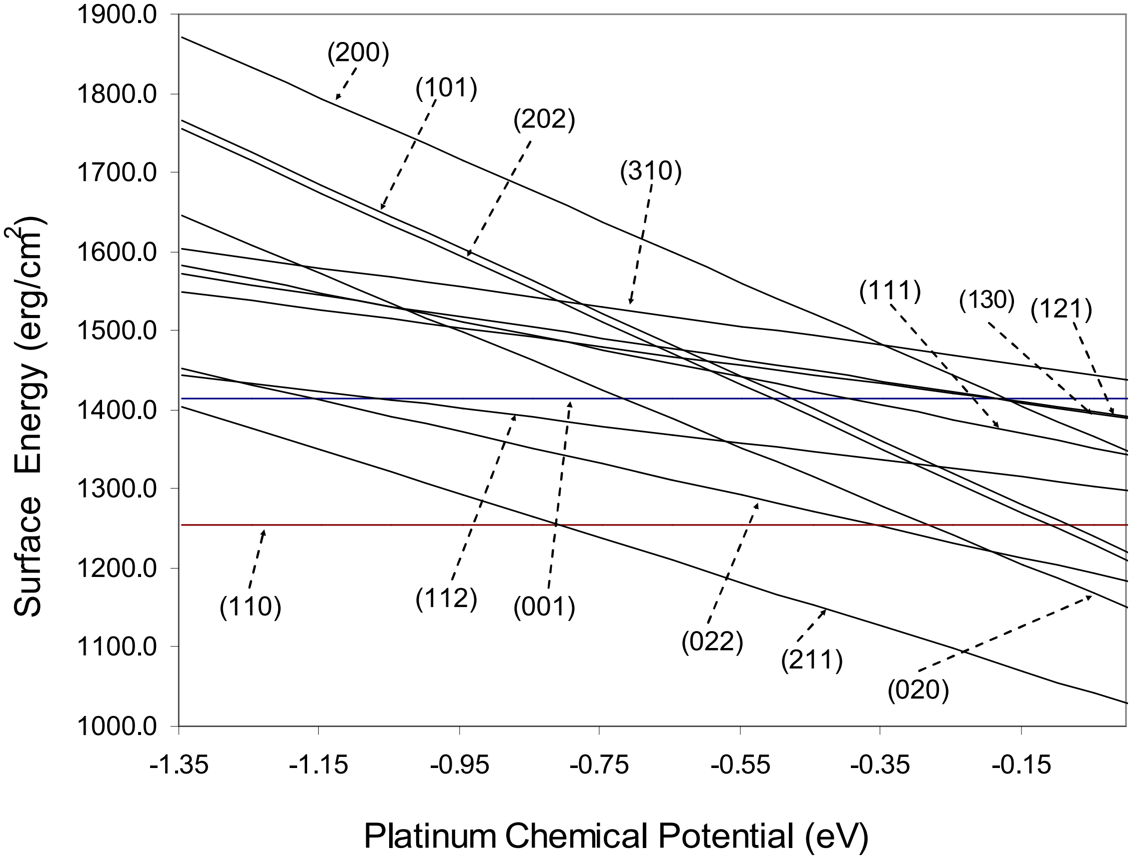

Figure 3.2d: *Surface energies of PtSi surfaces as the function of Pt chemical potential.*

Surface	Surface Energy (erg/cm^2)	Work Func. (eV)
PtSi(001)	1414.02 - 0.0000 μ_{Pt}	4.96
PtSi(020)	1150.59 - 367.68 μ_{Pt}	5.18
PtSi(100)	1347.08 - 389.66 μ_{Pt}	4.99
PtSi(022)	1184.01 - 198.99 μ_{Pt}	4.89
PtSi(111)	1344.04 - 177.22 μ_{Pt}	4.86
PtSi(110)	1254.66 - 0.000 μ_{Pt}	4.97
PtSi(101)	1220.48 - 202.27 μ_{Pt}	4.97
PtSi(202)	1209.92 - 404.53 μ_{Pt}	4.95
PtSi(211)	1029.71 - 278.43 μ_{Pt}	4.98
PtSi(112)	1298.63 - 108.21 μ_{Pt}	4.81
PtSi(121)	1388.58 - 136.05 μ_{Pt}	5.00
PtSi(130)	1392.12 - 116.92 μ_{Pt}	5.02
PtSi(310)	1438.65 - 122.47 μ_{Pt}	4.72
Pt(111)		5.70, 5.70[a]

Table 3.2b: *Surface energies (in erg/cm^2) and Work functions (in eV) for different PtSi surface orientations. [a]Experimental value [141].*

3.3 Work function at different PtSi surface orientations

The work function φ_m at a metal surface is defined as energy needed to remove an electron from the bulk to the vacuum just outside the metal [132]. It is generally known that the work function changes with the orientation of the metal surface by amounts ranging from one-tenth to one eV. This anisotropy is generally attributed to the redistribution of the charge density at the surface resulting in a different dipole barrier. As was first suggested by Smoluchowski [142], there are two competing effects on the dipole layer which tend to raise and lower the magnitude of the work function. The first effect is the charge spilling out at the surface resulting in the formation of a negative dipole layer (dipole pointing inward to the surface) which increases the work function.

The second effect is the tendency to smooth out the surface resulting in the formation of a positive dipole layer which tends to lower the work function. Since these two effects are comparable in magnitude, the net surface dipole magnitude can only be determined numerically. Within the DFT-GGA formalism the work function can be readily calculated in slab geometry as $\varphi_m = E_{Vac} - E_{Fermi}$. Here E_{Vac} and E_{Fermi} are the vacuum energy and the Fermi level. The vacuum energy E_{Vac} is estimated by the value of the total electrostatic potential in the vacuum region separating periodic images of the slab (Fig. 3.3a). The use of the electrostatic component only is justified since the exchange potential can be ignored in the middle of the vacuum region where its true value is zero. The calculated vacuum energy and Fermi energy for the PtSi(001) surface are 9.27 eV and 4.31 eV, respectively, giving work function of 4.96 eV as shown in Fig. 3.3a. Calculated work functions for different PtSi surfaces are tabulated in Table 3.2b. The highest φ_m value is found for the (020) surface and the lowest for the (310) surface, they differ by almost 0.46 eV. However, both the surfaces are relatively high energy terminations of PtSi under all thermodynamic conditions. Unfortunately, we know of no experimental values for the PtSi work functions. To gauge the reliability of our calculated results we calculated the work function of the Pt (111) surface and obtained φ_m=5.70 eV. The experimental value reported in the literature for that surface is 5.70 eV [141]. However, for Si(001)-2x1 reconstructed surface, we find the top of the valence band 5.10 eV below vacuum, while the experimental value is 5.27 eV [143]. Thus we believe the overall accuracy is about a tenth of eV.

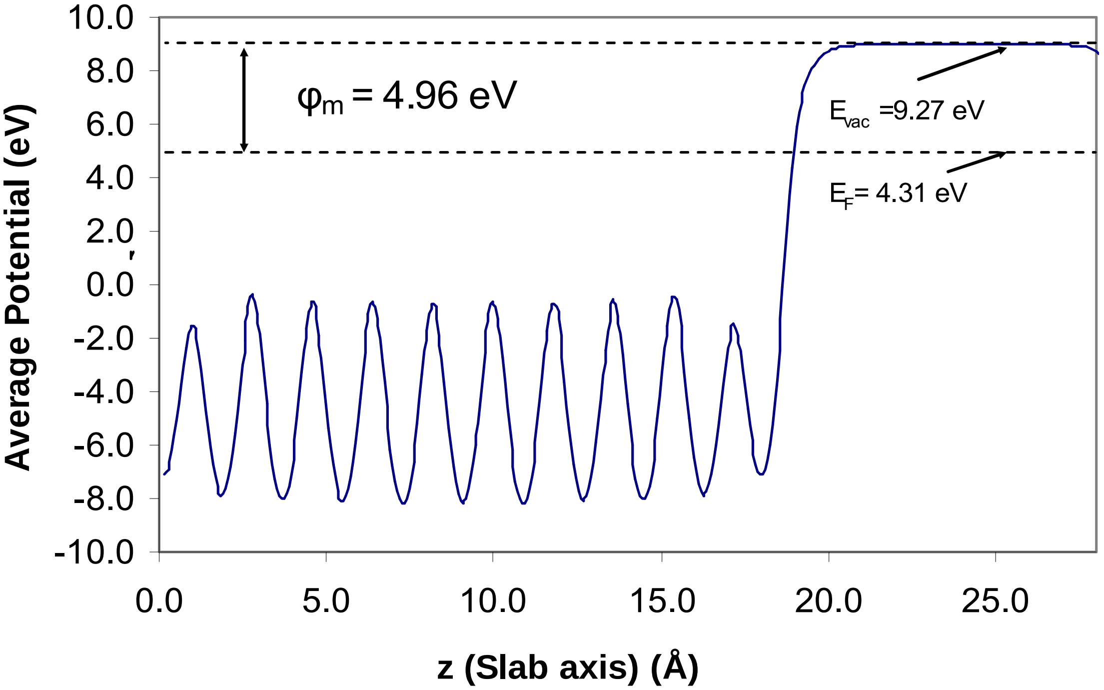

Figure 3.3a: *The planar averaged coulomb potential and work function of the PtSi (001) surface. Z is the direction normal to the (001) surface.*

3.4. Schottky Barrier height at the Si(001)/PtSi(001) interface

In a conventional Schottky model (no Fermi level pinning) (see section 1.3) the *n*-type barrier height at the metal semiconductor interface is given by the difference between the metal work function φ and electron affinity χ of the semiconductor (the energy difference between the conduction band edge and vacuum) (see Fig. 3.4a). Likewise, the p-type Schottky-barrier is the difference between the metal work function and the semiconductor valence band edge, $\chi + E_g - \varphi_m$. With the PtSi(001) work function of 4.96 eV and $\chi + E_g = 5.10$ eV for Si(001), the p-type barrier at the Si(001)/PtSi(001) interface is 0.14 eV in the Schottky limit. Alternatively, in the Bardeen limit (strong pinning) the p-type barrier is the difference between the charge neutrality level (ϕ_{CNL}) and top of the semiconductor valence band (see section 1.3 on SBH). The charge neutrality level in silicon is 0.30 eV above the valence band edge [144]. Thus, in the Bardeen limit the p-type barrier would be 0.30 eV. The barrier height can also be inferred from the metal induced gap states model (MIGS) model (Fig. 3.4a). The MIGS interpolates between the Bardeen and the Schottky limits in a linear fashion, and the p-type barrier ϕ_p, is given by:

$$\phi_p = E_g - S(\phi_m - \phi_{CNL}) - (\phi_{CNL} - \chi); \qquad (3.4b)$$

Here, ϕ_{CNL} is the charge neutrality level measured from the vacuum level and E_g is the valence band gap of the semiconductor and ϕ_m is the work function of the metal. S is the empirical pinning parameter describing the screening by the interfacial states [32, 74]

$$S = \frac{1}{1 + 0.1(\varepsilon_\infty - 1)^2}; \qquad (3.4c)$$

Where, ε_∞ is the high frequency limit of the dielectric constant of the semiconductor. For S=0 and 1 one regains the Bardeen and Schottky limits, respectively. Taking ε_∞ equal to 11.7 for Si, the S factor is 0.08. Using a value of 3.98 eV for the Si electron affinity (obtained by adding the measured energy gap to our calculated valence band maximum), we estimate the p-type barrier to be 0.25 eV, close to the Bardeen limit, as the Fermi level at the Si surface is strongly pinned.

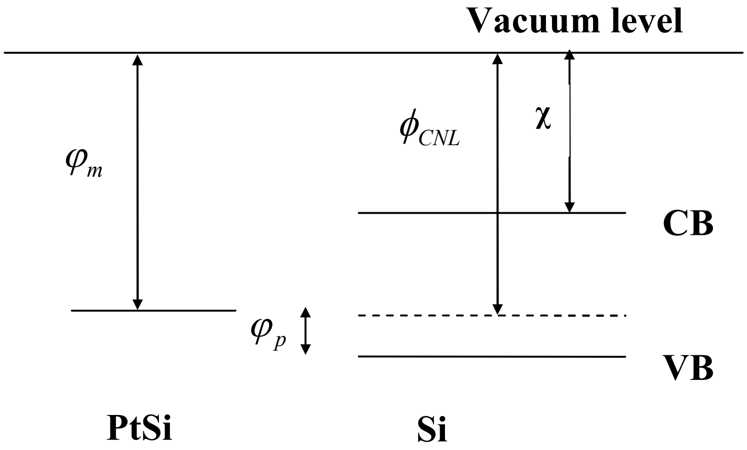

Figure 3.4a: *A schematic of the band alignment at the Si(001)-PtSi(001) interface*

To perform a first principles calculation of the Schottky barrier we build an atomistic model of the Si(001)/PtSi(001) interface. We use a supercell composed of twenty five layers of (001)-oriented Si on top of seven layers of PtSi(001) in a pseudo-epitaxial arrangement (Fig. 3.4b). The choice of the PtSi orientation is driven by its typical work function and relatively low surface energy, as well as a reasonable interfacial structure (see below), and by the cell-size limitations of *ab-initio* methods. Assuming the substrate is Si and the film is silicide, the two lateral lattice constants of PtSi (*a* and *b*) are strained by 8% and 3% respectively, to match with the bulk Si lattice constant. High strain has been suspected in PtSi films on Si (001) [145]. Optimization of the PtSi lattice constant in the direction normal to the interface results in a 4.9 % increase, in good agreement with the elasticity theory estimate. We then optimize all the internal degrees of freedom. Due to high strain we consider this calculation as only an estimate. However, we find that the work function of PtSi(001) under the same strain is increased only by 0.08 eV. The energy of our PtSi(001)/Si(001) interface is 1331.9 erg/cm^2 not too different from the PtSi surface energy, thus bonding at the interface appears quite reasonable, and we believe that the Schottky barrier estimate is relevant. The free energy of the interface at zero Kelvin is estimated using (3.2f). We set the chemical potential of Si in the Si side of the cell to zero (assuming equilibrium with the bulk), and since this particular interface is stoichiometric its free energy is independent of the chemical environment. It is worth noting that the interface energy thus defined is not the energy of separation. It is rather a measure of "combined unhappiness" of Si atoms in the topmost layer of Si to see PtSi above them, plus that of PtSi first layer to see a semiconductor below. The energy thus defined is used when the issues of wetting are of concern [146]. To calculate the Schottky-barrier height we need to know the Fermi level and the Si valence band edge positions. We follow the procedure originally introduced by Bylander and Kleinman [147] with the exception that only the average electrostatic potential is calculated across the supercell (exchange-correlation obtains its bulk value in the centers of the quantum wells and need not be added). We first compute the planar average of the potential and then its macroscopic average $\overline{V}_{Si}$ in the region away from the interface we believe to be bulk-like. Placing the valence band edge with respect to the macroscopic average potential requires a separate calculation for bulk Si, where we find the valence band maximum to be $\Delta E_{ref} = 5.55$ eV above the reference $\overline{V}_{Si}$. In a supercell the average electrostatic potential and Fermi energy are at 1.17 eV and 7.00 eV, respectively (Fig.3.4c). Using the bulk reference to locate the valence band top we calculate the barrier height of 0.28 eV using the formula:

$$\phi_p = E_F - (\overline{V}_{Si} + \Delta E_{ref}), \qquad (3.2f)$$

in strikingly good agreement with the MIGS estimate. In addition, we calculate the barrier height employing ultra-soft potentials with the LDA exchange correlation functional. This gives the value of 0.16 eV. The agreement between the two methods is within the accuracy of the calculation.

One can also infer the Schottky-barrier height analyzing the projected density of states of the Si in Si(001)/PtSi(001) supercell. In this calculation we employ PAW potentials. Fig. 3.4d shows the density of states projected on *s* and *p* states of a Si atom deep in the Si part of the supercell (where it is expected to regain the bulk like properties). The top of the Si valence band is a triple degenerate p-state at the Gamma (Γ) point (if one ignores the spin-orbit coupling). As apparent in Fig.3.2g, the Fermi energy and Si valence band edge are located at 7.00 eV and 6.69 eV. This gives the barrier height of 0.31 eV in close agreement with both Bardeen and MIGS predictions owing to the strong pinning character of Si surface. Experimentally for orthorhombic PtSi on p-type Si (001) the Schottky barrier height is 0.22-0.24 eV, [148], in excellent agreement with our theoretical estimate.

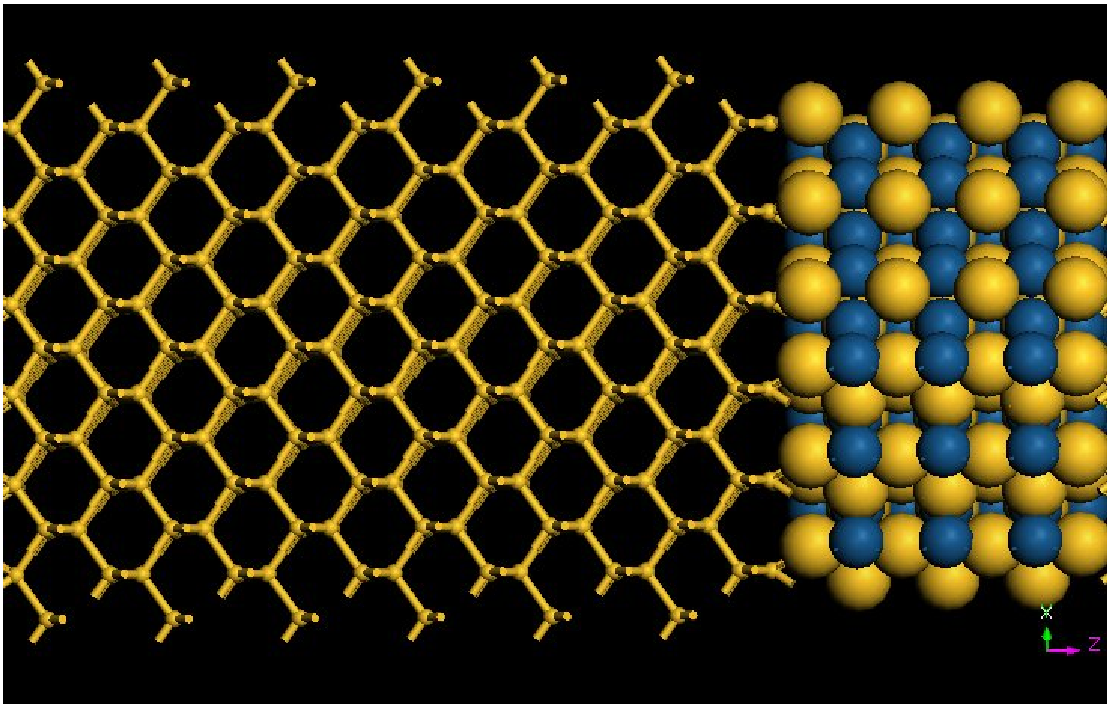

Figure 3.4b: *The Si(001)/PtSi(001) interface structure.*

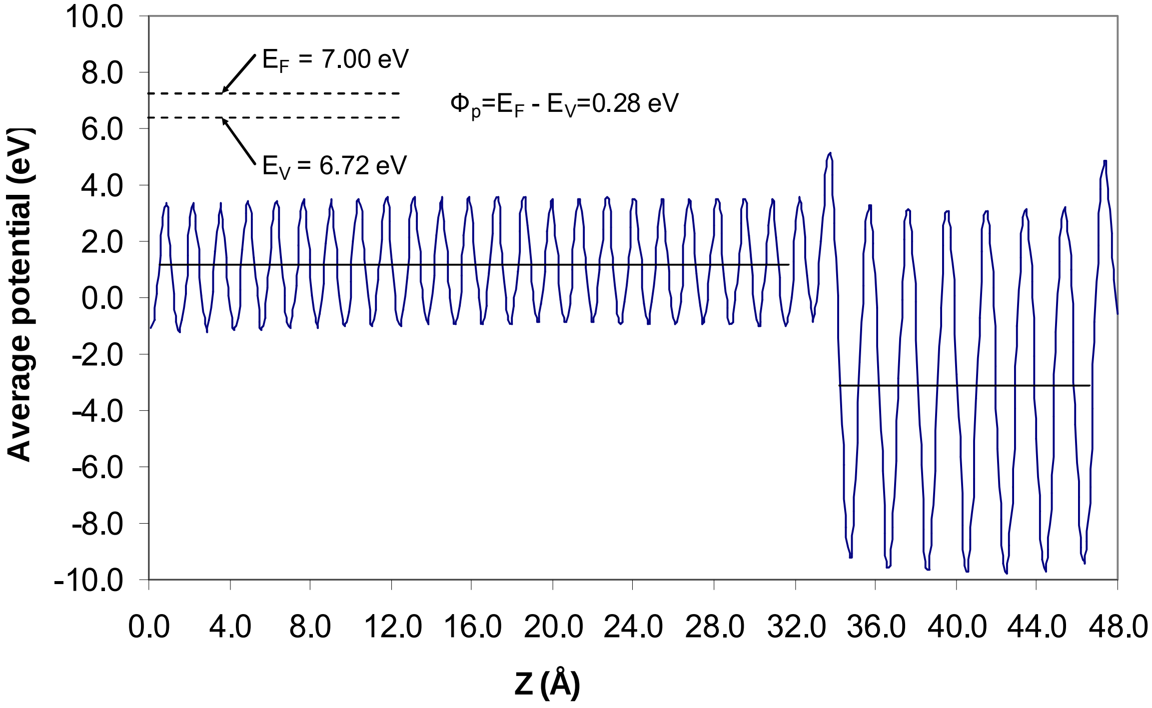

Figure 3.4c: *The average coulomb potential (in eV) of Si and PtSi in Si(001)/PtSi(001) supercell along Z (slab axis).*

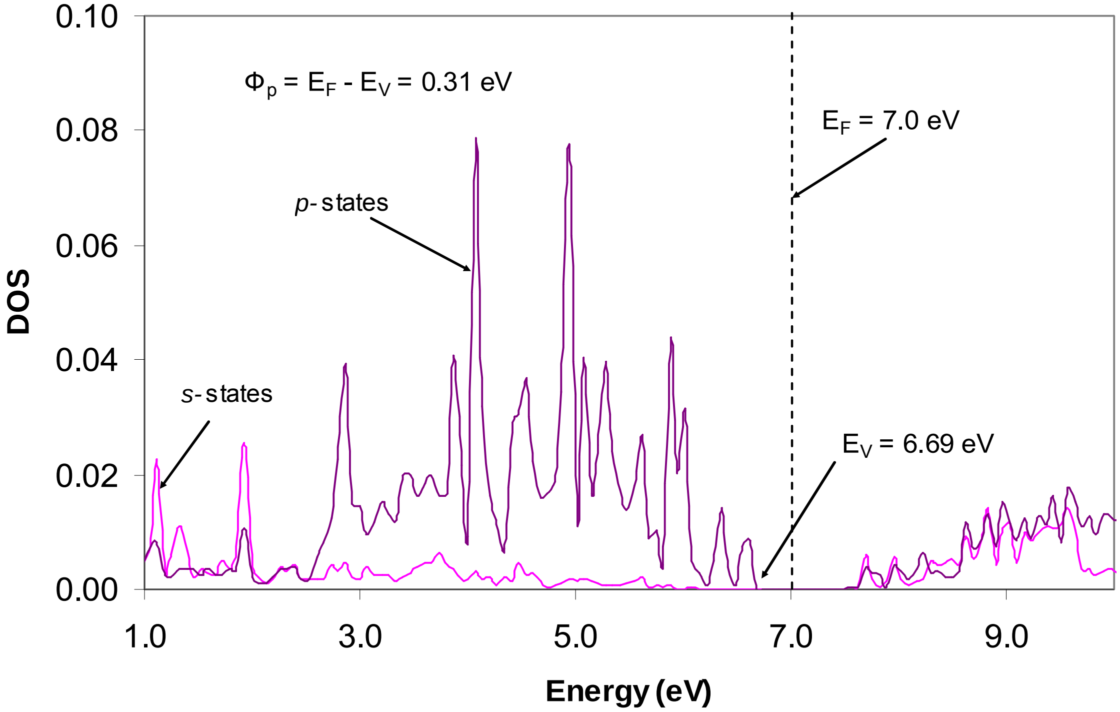

Figure 3.4d: *The density of states (in electrons $\AA^3$ per eV) site projected on a Si atom deep inside the Si side of Si(001)/PtSi(001) interface.*

3.5 Conclusion

With the aid of density functional theory, we have studied the electronic structure of PtSi and calculated work functions and surface energies for various surface terminations. We find that the work function varies by as much as 0.37 eV depending on the orientation. However, only two terminations considered here result in work functions significantly different from the typical value of about 4.97 eV. The two PtSi surface terminations found most stable are (211) under Pt rich conditions, and (110) under Pt poor conditions. The lower energy terminations identified here are those most commonly reported in power diffraction spectra. The calculated Schottky barrier height at the Si(001)/PtSi(001) interface of 0.28 ± 0.1 eV is in good agreement with available experiment and corresponds to the Bardeen limit.

Chapter 4

Electronic structure, surface energies and work functions of NiGe and PtGe

Unlike metal silicides, metal germanides have not, until recently, attracted much attention, presumably, due to the lack of practical applications. However, this is about to change, as scaling of traditional silicon based technology reaches its physical limit, a germanium channel field effect transistor (FET) is generating a lot of interest. The germanium channel metal oxide semiconductor FET (MOSFET) offers high mobility of both carriers (electrons and holes) resulting in higher overdrive current, enhanced transconductance, and higher cutoff frequencies as compared with a Si transistor. Historically, the use of germanium has been limited due to the lack of a stable native oxide and processing technology. Ironically, the emerging use of alternative high-k dielectrics as the gate insulator in Si-based technology may help finally realize the full potential of a germanium MOSFET. Nevertheless, to fully exploit transport properties of germanium, a low resistance contact technology will have to be developed based on metal germanides, much in the same way that self aligned metal silicides are used in a standard complimentary metal oxide semiconductor (CMOS) process today. Thus germanides with low *n*- and *p*-type Schottky barriers to the germanium channel (for use in NMOS and PMOS devices) need to be identified. Germanides are closely related to analogous silicides in respect to their compositions and structures. In the deep submicron regime (22 nm and below) NiGe, PtGe and their alloys appear to be promising as low barrier contacts to p-type germanium. The rest of the chapter is organized as follows. In the next section, we review bulk properties of NiGe and PtGe. In Sec. 4.2, we report elastic constants of both the systems. In Sec. 4.3 and 4.4, we report and discuss the surface energies and work functions for different surface orientations. We further discuss an unusual surface reconstruction of the NiGe(101)-Ge terminated surface.

4.1 Crystal and electronic structure of bulk NiGe and PtGe

Both NiGe and PtGe crystallize in the primitive orthorhombic structure in a MnP type lattice with space group Pnma (#62 in the international x-ray table) [149-152] (Fig 4.1a). For NiGe, the experimental lattice constants are a = 5.84 Å, b = 5.36 Å, c = 3.50 Å [149]. The PtGe, experimental lattice constants are a = 6.159 Å, b =5.832 Å, c = 3.754 Å [150]. There are four symmetry equivalent Ni (Pt) and four symmetry equivalent Ge atoms per primitive orthorhombic cell of NiGe (PtGe) respectively. There are four internal plane parameters, u_{Ge}, v_{Ge}, and u_{Ni} (u_{Pt}), v_{Ni} (v_{Pt}). First we perform the optimization of the orthorhombic cell and internal parameters. Experimental and calculated NiGe and PtGe lattice constants, cohesive energy and heat of formation are given in Table 4.1a. The internal in plane parameters are in Table 4.1b, where the caption gives the atomic position in terms of the internal parameters. The calculated lattice constants are within 1-2% of reported experimental values.

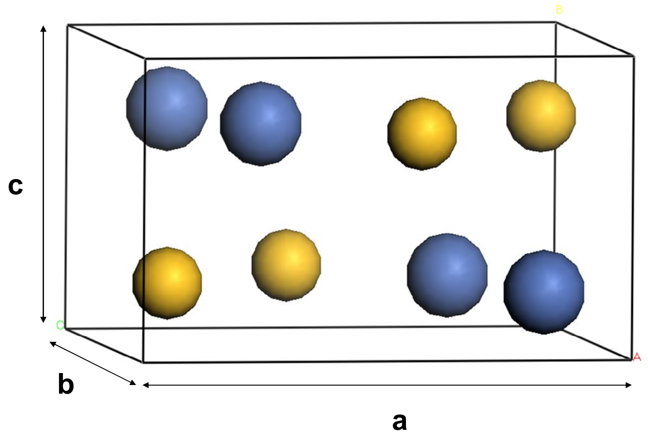

Figure 4.1a: *The orthorhombic unit cell of bulk NiGe and PtGe. The Yellow and blue balls are Ge and Ni atoms respectively. Lattice constants and free internal in plane coordinates are given in Table 4.1a and 4.1b .*

Material		a (Å)	b (A)	c (A)	E_{coh} (eV/atom)	ΔH_f (eV/atom)
Ni	cal.	3.52			5.40	
	exp.[a]	3.52			4.44	
Pt	cal.	3.93			5.77	
	exp.[a]	3.92			5.84	
NiGe	cal.	5.84	5.36	3.50	4.90	-0.32
	exp.[b]	5.79	5.37	3.43		
PtGe	cal.	6.16	5.83	3.75	5.18	-0.48
	exp.[c]	6.09	5.72	3.70		
Ge	cal.	5.75			3.76	
	exp.[a]	5.65			3.85	

Table 4.1a: *Theoretical and experimental lattice constants, heat of formations, and cohesive energy for Ni, Pt, NiGe, PtGe and Ge.* [a] Ref. [132], [b] Ref. [149], [c] Ref [150].

		$u_{Ni\ (Pt)}$	$v_{Ni\ (Pt)}$	u_{Ge}	v_{Ge}
NiGe	exp.	-	-	-	-
	cal.	0.1795	0.9933	0.5770	0.1769
PtGe	exp.[a]	0.1908	0.9995	0.5900	0.1850
	cal.	0.1922	0.9988	0.5884	0.1857

Table 4.1b: *Experimental and calculated free internal in-plane coordinates of NiGe and PtGe. The Ni (Pt) atoms are located at* $[u_{Ni\ (Pt)}, v_{Ni\ (Pt)}, 1/4]$, $[(1/2 - u_{Ni\ (Pt)}), (v_{Ni\ (Pt)} – 1/2), 1/4]$, $[(1- u_{Ni\ (Pt)}), (1- v_{Ni\ (Pt)}), 3/4,]$ *and* $[(1/2+ u_{Ni\ (Pt)}), (3/2 – v_{Ni\ (Pt)}), 3/4]$. *While the Ge atoms are located at* $[u_{Ge}, v_{Ge} , 1/4]$, $[(3/2- u_{Ge}), (1/2 + v_{Ge}), 1/4]$, $[(u_{Ge} -1/2), (1/2- v_{Ge}), 3/4]$ *and* $[(1- u_{Ge}), (1- v_{Ge}), 3/4]$. [a] Ref. [150]

Next we consider the electronic structure of bulk germanides. The energy bands of NiGe and PtGe along high symmetry directions in the Brillouin zone are shown in Fig. 4.1b and 4.1c, respectively. In Figs. 4.1d and 4.1g, we show the total density of states of NiGe and PtGe respectively. In Figs. 4.1e and 4.1f, we show the partial density of states projected onto Ni and Ge atoms. And, in Figs. 4.1h and 4.1i, we show the partial density of states projected onto Pt and Ge atoms, respectively. It is clear that the states at and just below the Fermi level are derived predominantly from the 3*d* (5*d*) orbitals of Ni (Pt) in the NiGe (PtGe) energy bands displayed in Fig. 4.1b and 4.1c. It is interesting to note that the metallicity of PtGe appears almost accidental. The lower Ge *p*-derived band near the Fermi level is occupied only along the Γ-Y direction, and the upper p-derived band "touches" the Fermi level at Z and along R- Γ direction. Elsewhere along the high symmetry directions a clear band gap is observed. Charge density contours for NiGe (001) and Ni (001) planes are shown in Figs. 4.1j and 4.1k. As apparent from Fig. 4.1j, there appears to be relatively strong three center (Ni-Ge-Ni) covalent bonds between Ni and Ge atoms in the (001) plane. This is interesting since NiGe is metallic. It is well known that the bonding of transition metals is almost entirely due to the *d*-electrons. Thus it is not unexpected that the Ni-*d* would hybridize with the Ge-*p* to form covalent bonds. This is very similar to the chemical bonding observed in PtSi [130]. The bonding in PtGe was found to be qualitatively similar to that in NiGe.

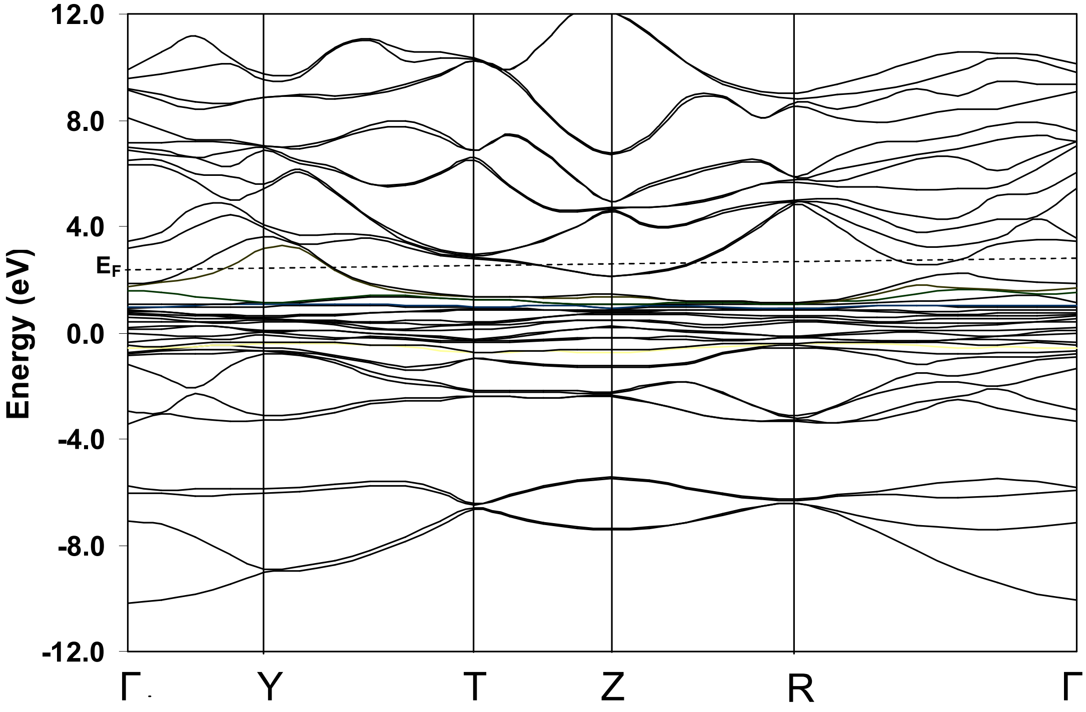

Figure 4.1b: *Energy Bands of bulk NiGe. The symmetry points are labeled according to Slater [Ref. 153].*

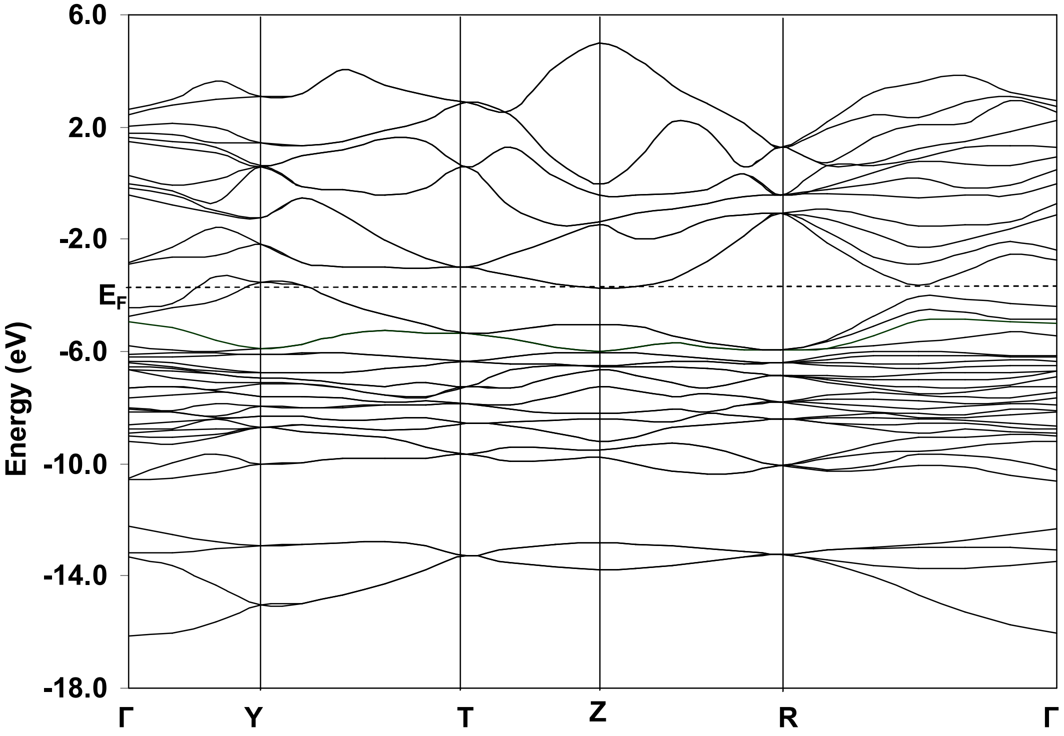

Figure 4.1c: *Energy Bands of bulk PtGe. The symmetry points are labeled according to Slater [Ref. 153].*

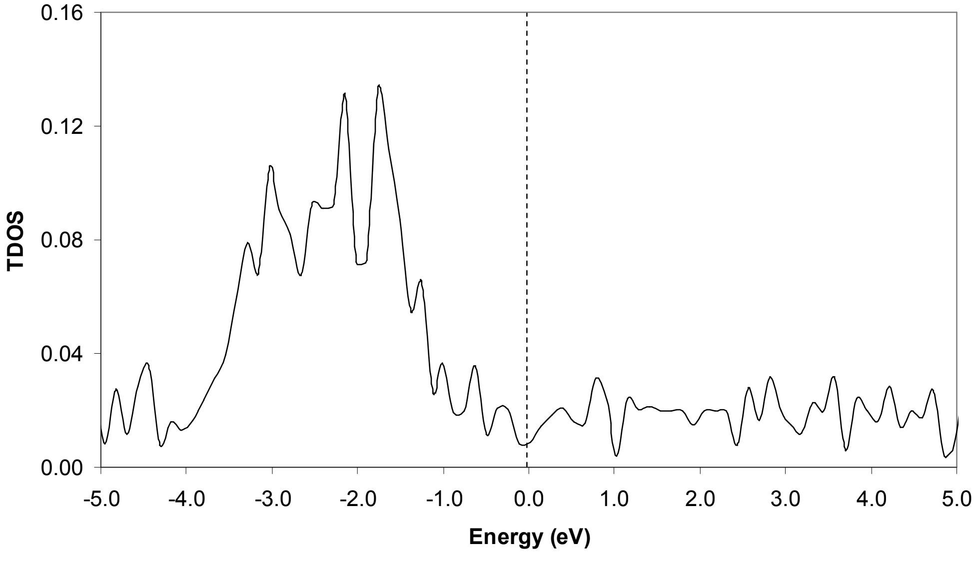

Figure 4.1d: *The total density of states of NiGe (in electrons per Å^3 per eV). Fermi energy is indicated by the dashed line.*

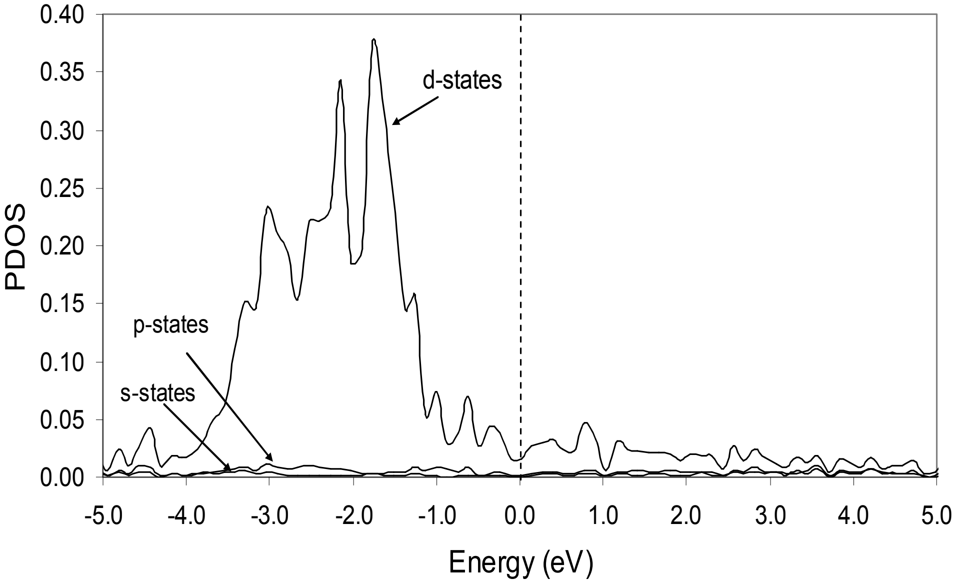

Figure 4.1e: *The partial density of states of NiGe (in electrons per Å^3 per eV) projected onto Ni atoms. Fermi energy is indicated by the dashed line.*

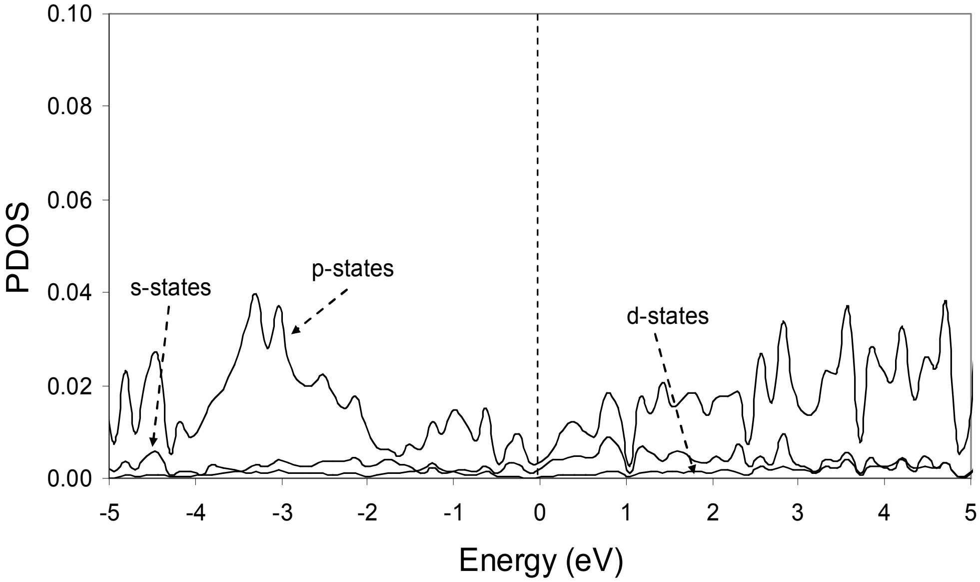

Figure 4.1f: *The partial density of states of NiGe (in electrons per Å^3 per eV) projected onto Ge atoms. Fermi energy is indicated by the dashed line.*

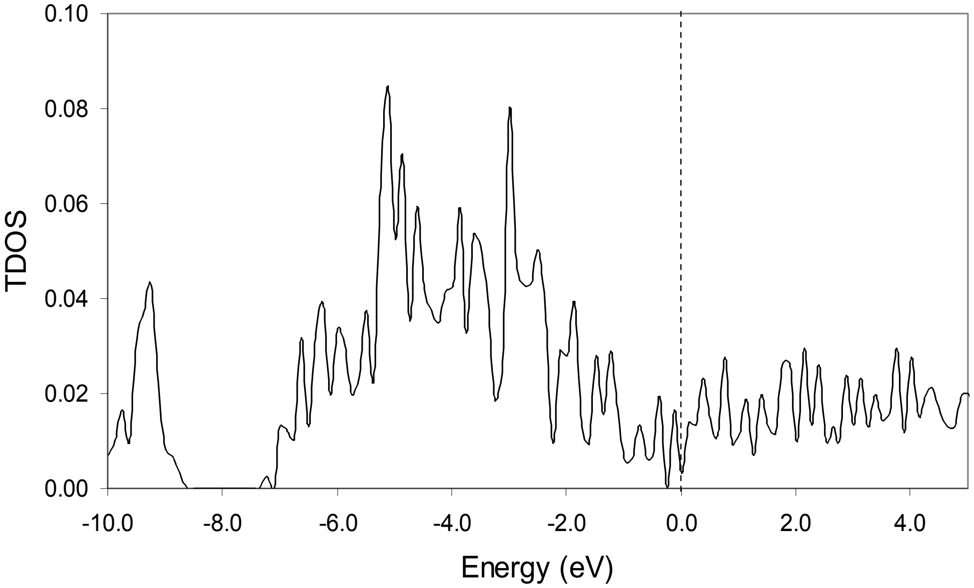

Figure 4.1g: *The total density of states of PtGe (in electrons per Å^3 per eV). Fermi energy is indicated by the dashed line.*

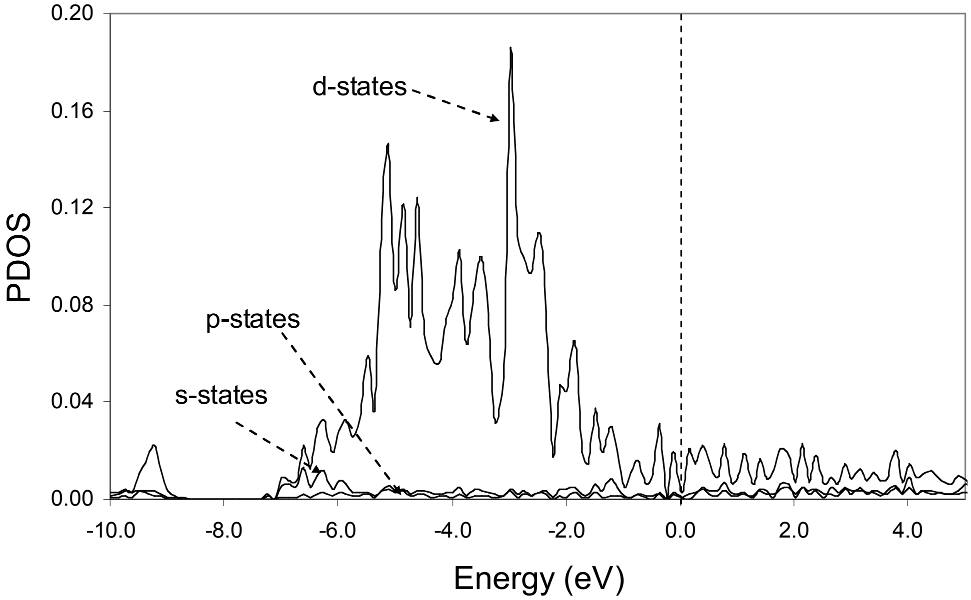

Figure 4.1h: *The partial density of states of PtGe (in electrons per Å^3 per eV) projected onto Pt atoms. Fermi energy is indicated by the dashed line.*

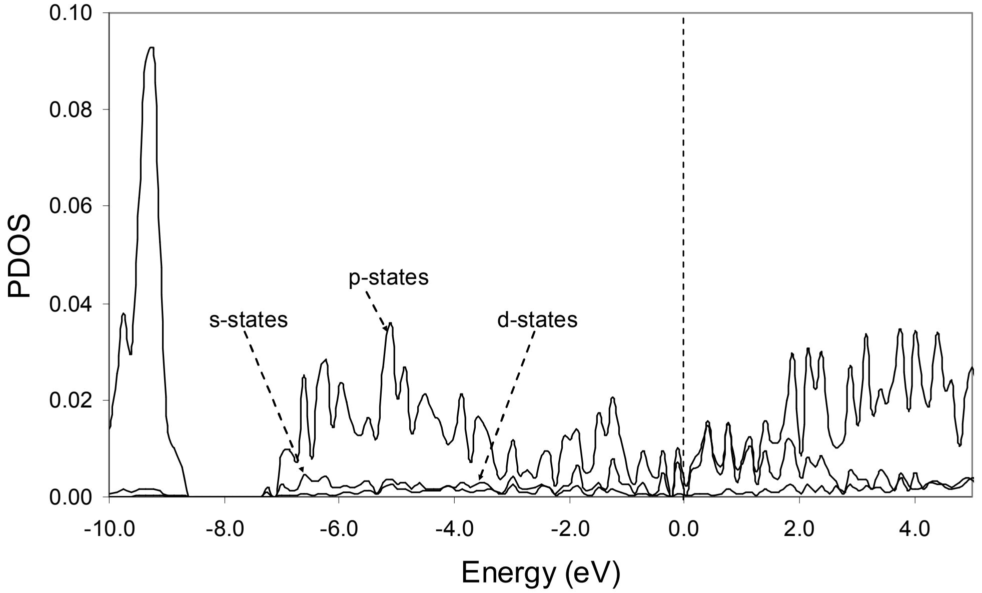

Figure 4.1i: *The partial density of states of PtGe (in electrons per Å^3 per eV) projected onto Ge atoms. Fermi energy is indicated by the dashed line.*

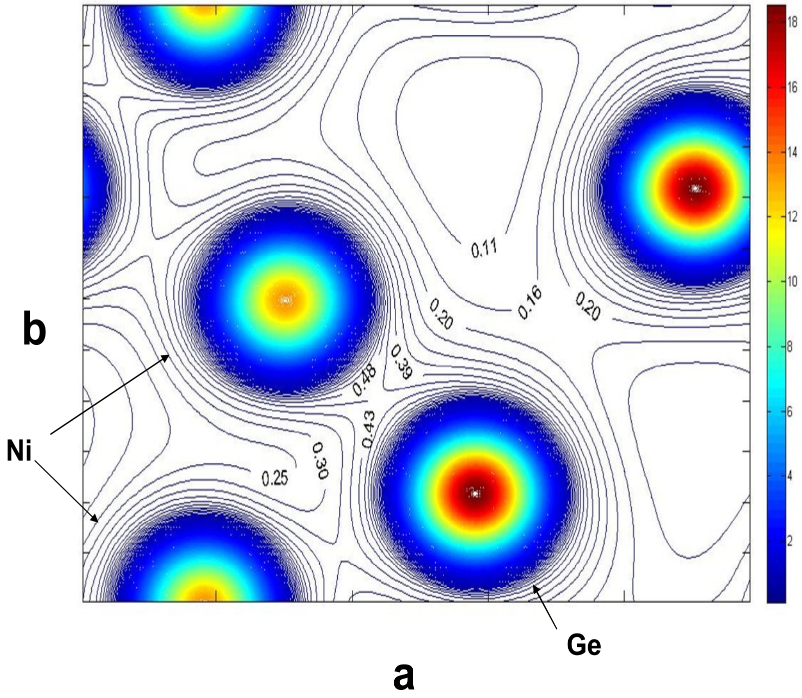

Figure 4.1j: *Valance electron charge density (electrons/Å^3) contours in the (001) plane for NiGe unit cell*

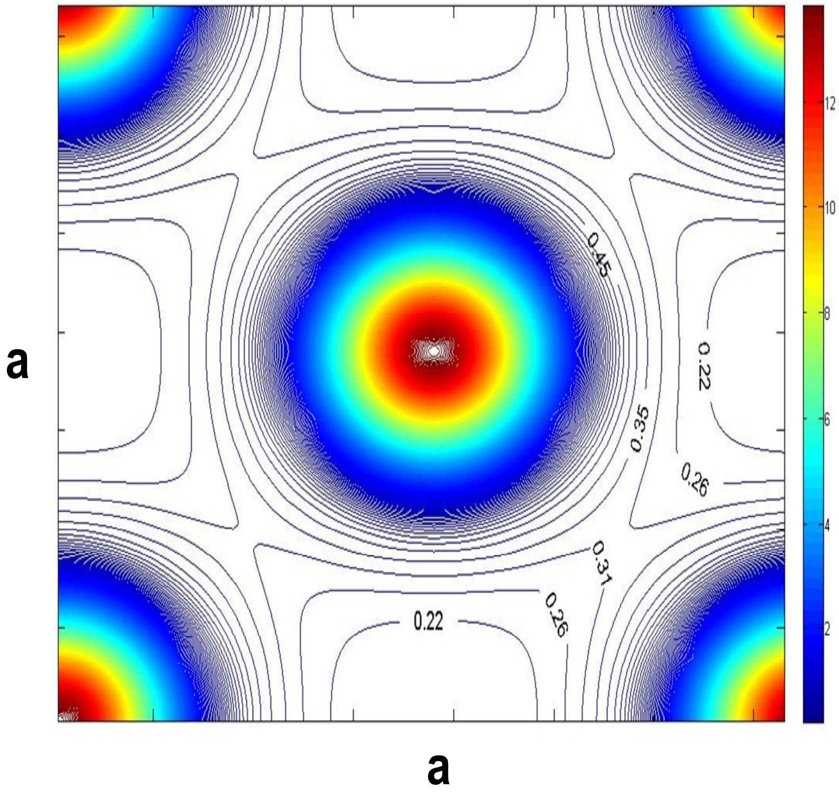

Figure 4.1k: *Valance electron charge density (electrons/Å^3) contours in the (001) plane for Ni unit cell.*

4.2 Elastic constants

Thermal cycling during the Ge process is expected to be gentler than that of the Si (during the activation of dopants the Si wafer is annealed at temperature in excess of 1000° C). Still a wafer will experience significant thermal stress, and knowing the elastic constants of germanide crystals is of practical importance. Nine elastic constants are needed to describe an orthorhombic crystal (compare with only three for a cubic crystal) [154]. Our elastic constants were calculated by fitting the total energy as a function of strain to a parabola. The fit is based on six points separated by ~2 meV, and the applied strain is ~ 1% of the lattice constant. (See section 2.3.8). The experimental and calculated elastic constants of Si, Ge, Ni, Ge (*fcc* crystals) are given in Table 4.2a. The theoretical elastic constants and bulk moduli are within 5% of experiment. The calculated elastic constants of orthorhombic NiGe and PtGe are given in Table 4.2b. Interestingly, despite the difference in crystal structure and nature of bonding the values calculated for mono-germanides are remarkably close to simple averages of the Ge and metal values. We have checked the convergence of the elastic constant C_{44} with respect to the number of **k**-points and plane wave energy cutoff (for NiGe). The value of C_{44} was raised by 0.7 % and 2.1 % as the **k**-point mesh is increased from 6×6×8 to 8×8×12 and 10×10×16. The C_{44} value was raised by 0.3 % and 0.4 % as the energy cutoff was increased from 380 eV to 530 eV and 640 eV respectively. To further check the quality of our calculations we consider the issue of mechanical stability. The Cauchy conditions for an *fcc* crystal restrict the elastic constants in the following way [131]:

$$(C_{11}-C_{12}) > 0,\ C_{11} > 0,\ C_{44} > 0,\ (C_{11}+2\,C_{12}) > 0 \text{ and } C_{12} < B < C_{11}$$

Where, B is the bulk modulus. For *fcc* crystals, such as Ni, Pt, Ge and Si, the bulk modulus can be calculated as $B_0 = 1/3(C_{11}+2C_{12})$. To ensure the internal consistency we also calculate the bulk modulus and equilibrium volume by fitting the total energy as a function of volume to a parabola and a four term Birch-Murnaghan equation of state [155]:

$$E(V) = \sum_{n=1}^{4} c_n V^{-2n/3}\ ;$$

The bulk moduli calculated from the elastic constants, from a parabolic fit and Birch-Murnaghan fit, in addition to experimental values are given in Tables 4.2a and 4.2b. The calculated elastic constants of Ge, Si, Ni and Pt lie well within the allowed range for mechanically stable fcc crystals. Likewise, the elastic constants of mechanically stable orthorhombic crystals are constrained by the following conditions [131]:

$C_{11} > 0, C_{22} > 0, C_{33} > 0, C_{44} > 0, C_{55} > 0, C_{66} > 0, (C_{11} + C_{22} - 2\,C_{12}) > 0,$

$(C_{11} + C_{33} - 2\,C_{13}) > 0,$

$(C_{22} + C_{33} - 2\,C_{23}) > 0,$

$(C_{11} + C_{22} + C_{33} + 2\,C_{12} + 2\,C_{13} + 2\,C_{23}) > 0,$ and

$1/3\ (C_{12} + C_{13} + C_{23}) < B < 1/3\ (C_{11} + C_{22} + C_{33})$.

For orthorhombic NiGe and PtGe bulk modulus is first calculated as $B_0 = 1/9(C_{11}+C_{22}+C_{33}+2C_{12}+2C_{13}+2C_{23})$ [131]. As evident from Table 4.2b, the calculated elastic constants of NiGe and PtGe do obey conditions of mechanical stability. The rather poor agreement (relative to the *fcc* crystals) between the PtGe bulk modulus calculated from the elastic constants and the two bulk moduli calculated assuming hydrostatic pressure, is undoubtedly due to the inner displacements of the atoms and the need to equilibrate the stresses. That the agreement for NiGe is good may be fortuitous.

		Ni[a]	Pt[b]	Ge[c]	Si[d]
C_{11}	cal.	268.4	334.6	124.2	159.8
	exp.	261.2	358	131	165
C_{12}	cal.	159.3	247.1	45.9	60.5
	exp.	150.8	254	44	63
C_{44}	cal.	131.2	72.2	71.3	75.2
	exp.	131.7	77	68.8	79.1
B_0	cal.$^{\text{Birch}}$	194.9	272.2	69.9	94.7
	cal.$^{\text{parabolic}}$	195.3	275.8	70.8	94.2
	cal.$^{\text{elastic}}$	195.7	276.3	72.0	93.6
	exp.	187.6	288.4	76.3	97

***Table 4.2a:** Calculated and experimental elastic constants (in the units of GPa) of Ge, Si, Ni and Pt. Experimental values for Ge, Si, Ni and Pt are extrapolated to 0 K. B_0 is the bulk modulus calculated from elastic constants and from Birch-Murnaghan fit. B_0 is related to elastic constants as $B_0 = 1/3(C_{11} + 2 C_{12})$. Superscript indicates the reference to the experimental values.* [a] *Ref. [132],* [b] *Ref. [156],* [c] *Ref. [157],* [d] *Ref. [158]*]

	NiGe	PtGe
C_{11}	211.69	216.52
C_{22}	183.76	200.57
C_{33}	173.93	206.15
C_{12}	135.70	125.18
C_{13}	99.80	114.42
C_{23}	106.37	113.12
C_{44}	67.20	68.88
C_{55}	106.94	76.02
C_{66}	105.41	53.63
$B_0^{elastic}$	139.24	147.63
$B_0^{Parabolic}$	140.58	153.41
B_0^{Birch}	140.94	154.62

***Table 4.2b:** Calculated elastic constants and bulk modulus (in units of GPa) of NiGe, and PtGe. $B_0^{elastic}$ is the bulk modulus calculated from the elastic constants and is given as $B_0^{elastic} = 1/9(C_{11}+C_{22} + C_{33} + 2 C_{12} + 2 C_{13} + 2 C_{23})$. $B_0^{Parabolic}$ and B_0^{Birch} are the bulk modulus obtained from a parabolic and Birch-Murnaghan fit.*

4.3 Surface energy and reconstruction of NiGe and PtGe

We calculated surface energies for (100), (010), (001), (011), (101), (111), (120), (121), (211) and (021) orientations of bulk NiGe and PtGe for different surface stoichiometries. To simulate the surfaces, we used supercells in slab geometry of thickness 14-20 Å (ten to seventeen layers in addition to vacuum layers). For example, to simulate the NiGe (001) surface, we use eight layers of vacuum over eleven layers of NiGe (001) (see section 3.2). The smallest (001)-oriented slab contains 44 atoms; the largest (121)-oriented slab contains 63 atoms. Symmetric slabs based on (1×1) surface cells for each termination are used (the lateral lattice constant is fixed to that derived from the calculated bulk value). For the Brillouin zone integration, we use a moderate 4×4×1 Monkhorst-Pack [118] mesh, due to relatively large cell sizes. To check the convergence we perform calculations with (6×6×1) and (8×8×1) grids, and find the energy changes are of the order of 10^{-4} eV/atom. Each supercell is relaxed until the forces on each atom reach 0.02 eV/Å or less.

Now we describe the nature of reconstruction of the NiGe (001)-1×1 surface. The NiGe (001) surface has a rectangular surface unit cell of dimensions 5.84 Å by 5.36 Å. There are two Ge and two Ni atoms in the surface. The unreconstructed surface can be described as zigzag NiGe chains running along the shorter cell edge (see Fig. 4.3a). We define the rumpling parameter δr_i as in [135]

$$\delta r_i = (Z_i^{Ni} - Z_i^{Ge}) / d_o ,$$

Where Z^{Ni} and Z^{Ge} are the z coordinates of the Ni and Ge atoms in the ith layer and d_0 is the bulk interlayer distance (Fig. 4.3b). We also define inter-planar relaxation parameter δr_{ij} as

$$\delta r_{ij} = (Z_i - Z_j) / d_a ,$$

Where Z_i and Z_j are the z coordinates of the ith and jth layer and d_a is the bulk interlayer distance. Z_i is calculated by averaging the z coordinate of the Ni (Pt) and Ge atoms. The inter-planar distance in the bulk NiGe is 1.75 Å. The results for surface rumpling and inter-planar relaxation are presented in Table 4.3a. In addition, we observe relatively small in-plane atomic displacements in the first two surface layers. The Ni and Ge atoms on the first surface layer are displaced by 0.01 Å and 0.11 Å, respectively. We did not consider the possibility of a more complex surface relaxation in a larger surface cell.

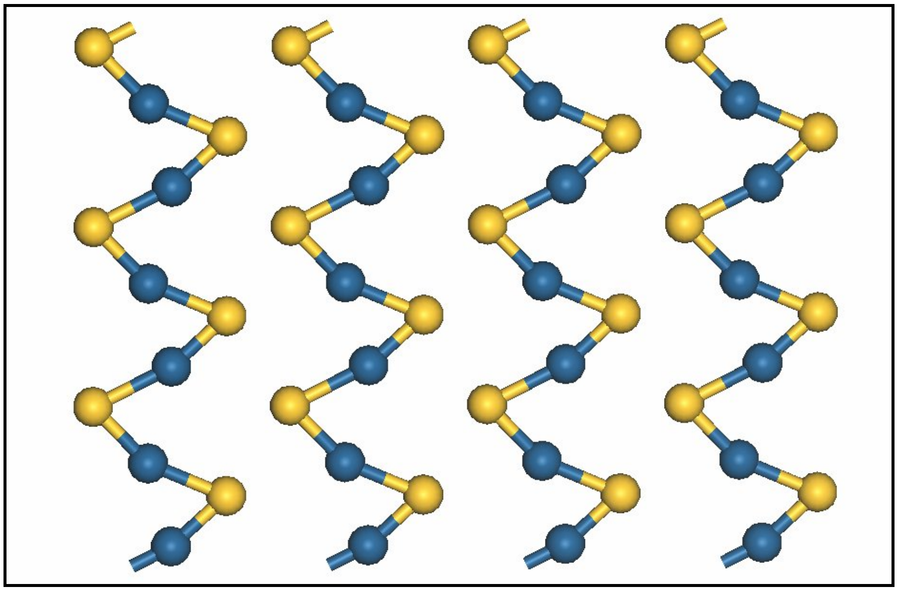

Figure 4.3a: *Top view of the unreconstructed NiGe (001) surface. Blue and yellow balls are Ni and Ge atoms respectively.*

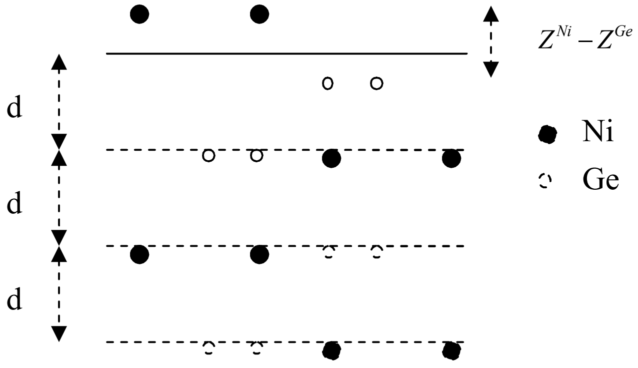

Figure 4.3b: *NiGe (001) surface (side view).*

	δr_1	δr_2	δr_3	δr_4	δr_{12}	δr_{23}	δr_{34}	δr_{45}
Calc.	-9.8	2.0	-2.9	0.7	-4.8	0.6	0.0	0.0

Table 4.3a: *Surface rumpling and inter-planar relaxation in % for the NiGe (001) surface. Rumpling parameter* δr_i *is defined as* $\delta r_i = (Z_i^{Ni} - Z_i^{Ge}) / d_o$, *where* Z^{Ni} *and* Z^{Ge} *are the z coordinates of the Ni and Ge atoms in the ith layer and* d_0 *is the bulk interlayer distance (Fig.8a). Inter-planar relaxation parameter* δr_{ij} *is defined as* $\delta r_{ij} = (Z_i - Z_j) / d_a$, *where* Z_i *and* Z_j *are the z coordinates of the ith and jth layer and* d_0 *is the bulk interlayer distance.* Z_i *is calculated by averaging the z coordinates of the Ni and Ge atoms.*

We have also studied the reconstruction of the germanium terminated NiGe (101)-1×1 surface. As cut the NiGe (101)-Ge terminated surface has two germanium atoms at the top layer and two Ge atoms at the layer 0.97 Å below it (see Fig 4.3c). Due to the strong covalent character of Ni-Ge bonds it is not unreasonable to describe the top-layer Ge atoms as having two “bonds” to Ni atoms in the sub-surface layer and the lower-layer ones as having four (the bond length is ~2.46 Å). The geometry in the top-layer is vaguely reminiscent of as cut Ge (001) (1×1) surface, which, as is well known, is unstable with respect to a (2×1) reconstruction caused by dimerization. As apparent from Fig. 4.3c-4.3g, topmost germanium atoms at the NiGe (101) surface also tend to dimerize! This is rather interesting since dimerization (or any significant surface relaxation) is not very common for metallic surfaces with a notable exception of Au. Note that the cell remains (1×1). The separation between top Ge atoms is decreased from 3.28 Å to 2.71 Å suggesting formation of a dimmer upon reconstruction (see Fig. 4.3d). Overall, however, the reconstruction is more complicated and can be described as follows. In Fig. 4.3e we show the rhombus formed by four unreconstructed surface Ge atoms, note that there are no Ge-Ge bonds. Upon reconstruction, two top Ge atoms bond with each other, and also with two lower Ge atoms (see Fig. 4.3f). As can be seen from Fig. 4.3g the surface Ge-Ge bonds are covalent. In addition, Ge atoms form back bonds to Ni in the sub-surface layer ranging from 2.45 to 2.79 Å in length. Furthermore, the energy gained in this unusual reconstruction process is 1.70 eV or 0.85 eV per surface, which is significant and about 50 % of the cohesive energy of bulk Ge per covalent bond! The results for surface rumpling and inter-planar relaxation are presented in Table 4.3b. Importantly, this surface is also the lowest energy surface of orthorhombic NiGe.

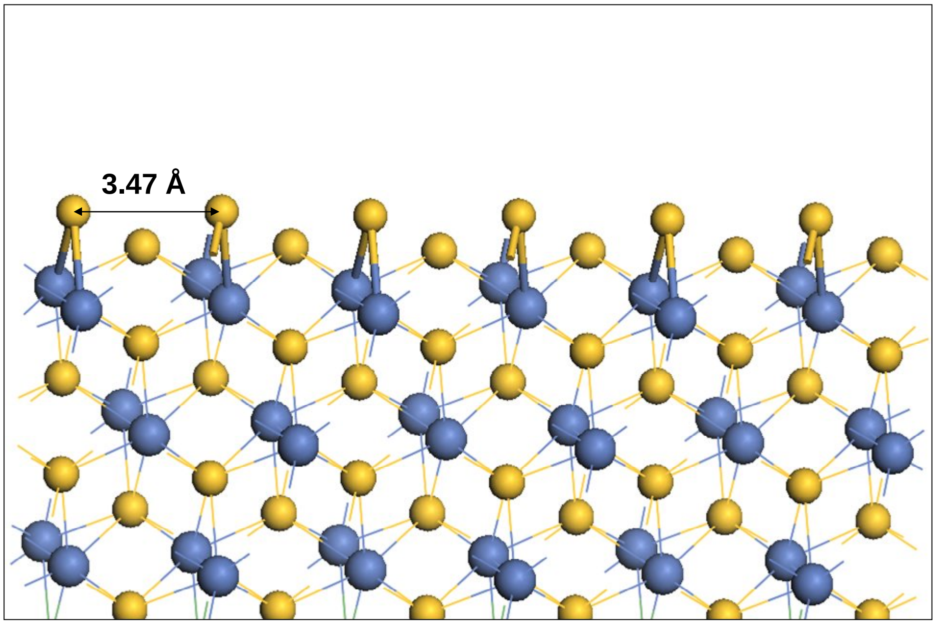

Figure 4.3c: *Side view of the* ***unreconstructed*** *Ge-terminated NiGe (101) surface. Yellow and blue balls are Ge and Ni atoms, respectively. The top layer Ge atoms are two-fold coordinated and Ge-Ge distance is 3.47 Å. The structure is vaguely reminiscent of the Ge (001) un-reconstructed surface (Ge-Ge separation is the second-nearest neighbor distance of 3.99 Å).*

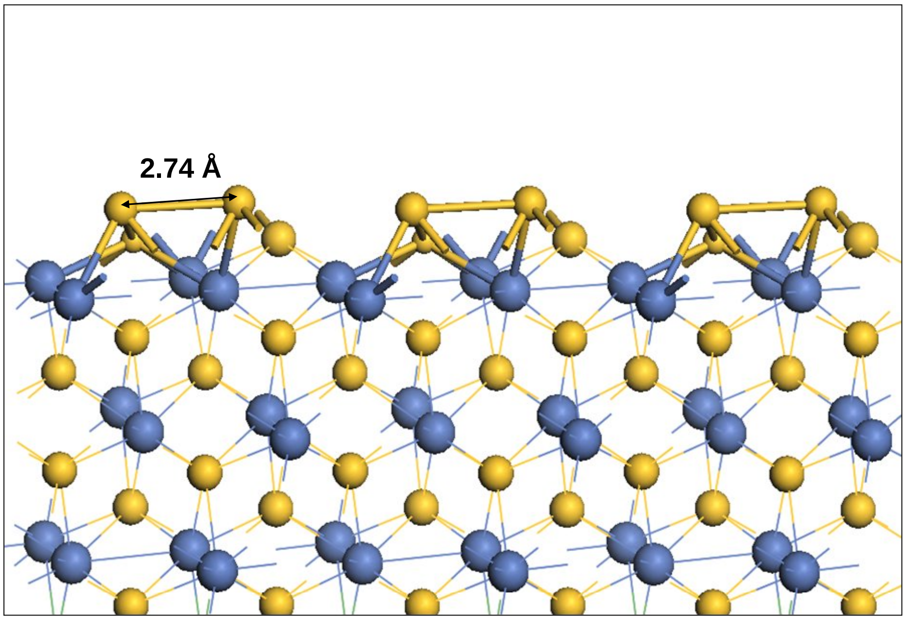

Figure 4.3d: *Side view of the* **reconstructed** *Ge-terminated NiGe (101) surface. Yellow and blue balls are Ge and Ni atoms, respectively. The bonds formed in the surface layer are indicated with balls and sticks, while the rest of the slab is rendered with a wireframe. Top Ge atoms in the surface layer are four-fold coordinated with one bridging dimer bond in the surface plane one bond to the lower Ge and two back bonds to Ni atoms in the sub-surface layer. The lower Ge atoms are five-fold coordinated; in addition to Ge-Ge bond with the top Ge, they form four back-bonds to sub-surface Ni atoms.*

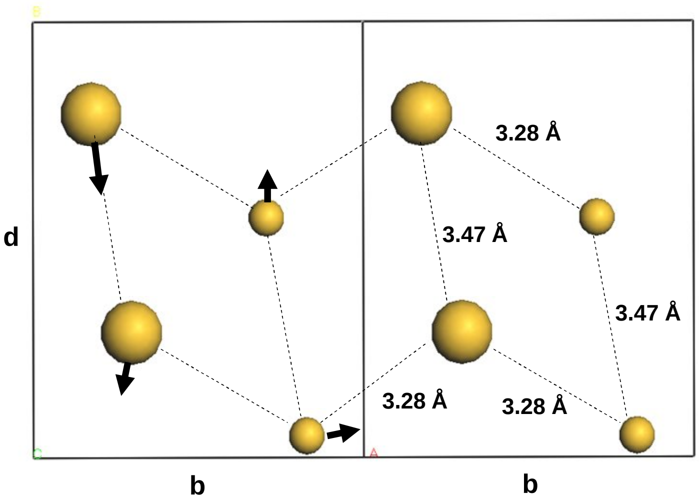

Figure 4.3e: *Top view of the* **unreconstructed** *Ge-terminated NiGe (101) surface. Larger balls represent Ge atoms in the topmost layer, and smaller balls represent Ge atoms that lie in the plane 0.97 Å below. Two surface unit cells are shown, the lattice constants are* **b***=5.36 Å,* **d***=6.81 Å .There are no bonds between Ge atoms before the relaxation. The arrows indicate the movement of the atoms during relaxation.*

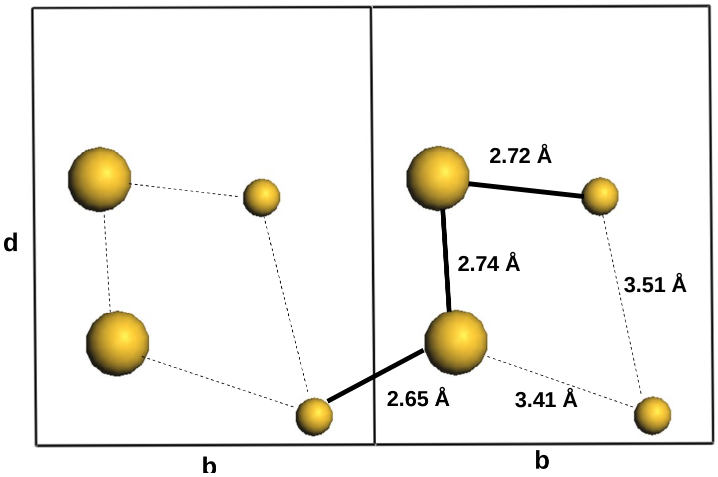

Figure 4.3f: *Top view of the* **reconstructed** *Ge-terminated NiGe (101) surface. Larger balls represent Ge atoms in the topmost layer, and smaller balls represent those in the plane 0.87 Å below. Two surface unit cells are shown for clarity. The surface Ge-Ge bonds are indicated with thick black lines. Top Ge atoms form a 2.74 Å dimer bond with each other, and one similar and one shorter bond to lower plane surface Ge atoms, as well as two back-bonds to Ni atoms below.*

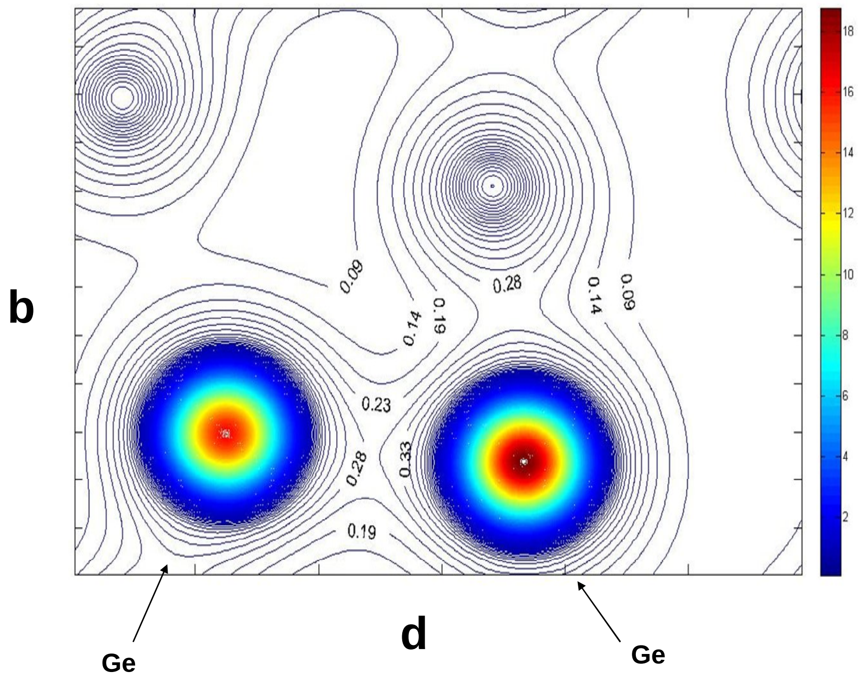

Figure 4.3g: *Valance electron charge density (electrons/$Å^3$) contours at NiGe(101)-1x1 (Ge terminated) reconstructed surface. The surface cell is (**b**,**d**) with 'd' being equal to* $\sqrt{a^2+c^2}$ *. The dimmer Ge-Ge bond is clearly seen between two marked top Ge atoms, also a back-bond to the lower Ge atoms can bee seen.*

	δr_1	δr_2	δr_3	δr_4	δr_5	δr_6	δr_7	δr_{12}	δr_{23}	δr_{34}	δr_{45}	δr_{56}	δr_{67}
Calc.	14	1.3	11.7	10.2	4.8	3.7	0.3	-4.1	7.7	-46.4	14.2	-2.6	4.4

Table 4.3b: *Surface rumpling and inter-planar relaxation in % for the NiGe (101) surface. Subscript 1, 2, 5 and 6 corresponds to Ge layers while subscript 3, 4 and 7 corresponds to Ni layers.*

The surface energy of a NiGe or PtGe surface is estimated using the Gibbs free energy approach (See section 2.3.7 and 3.2). For example, the surface free energy of NiGe is given by:

$$E = \tfrac{1}{2}\left(E_{Slab} - N_{Ge}E_{Ge} - N_{Ni}E_{Ni} + N_{Ge}E_{form} + \mu_{Ni}(N_{Ge} - N_{Ni}\right)$$

Where E_{Slab} is the total energy of the supercell, E_{Ge}, and E_{Ni} are the energies per atom of bulk Ge and Ni, respectively. N_{Ge} (N_{Ni}) and μ_{Ge} (μ_{Ni}) are the number of Ge (Ni) atoms and Ge(Ni) chemical potential, respectively. Chemical potentials of Ni and Ge are taken with respect to the bulk phases and the surface is assumed to be in equilibrium with bulk NiGe (thus μ_{Ge} and μ_{Ni} are related by the equilibrium condition: $\mu_{Ge} + \mu_{Ni} = -E_{form}$(NiGe)). The energy is given per unit surface cell, and a factor of ½ is inserted to account for two surfaces in the supercell.

The surface energies of different NiGe and PtGe surfaces are tabulated in Table 4.3c and 4.3d, respectively. In Fig.4.3h and 4.3i, we show surface energies of different NiGe and PtGe terminations as a function of the Ni or Pt chemical potential. The zero value of the chemical potential corresponds to metal (Ni or Pt) rich conditions, beyond that point metallic Ni (Pt) will start forming on the surface. The range is bound by the NiGe formation energy, Ge would start forming on the surface should this value be exceeded. Not surprisingly, as can be seen from Figure 10a, the germanium-terminated (101) surface remains most stable under most growth conditions while the germanium-terminated (211) surface becoming the most stable under extremely Ni-rich conditions. We also notice that under Ge rich conditions while (101) is still the lowest energy surface, several terminations such as germanium terminated (110), (211), and (100), nickel-terminated (211), and stoichiometric (001) and (021) are very close in energy, and are only 200 erg/cm^2 higher than Ge-terminated (101). Overall, the Ni-rich termination is less stable than the stoichiometric termination, which in turn is less stable than the Ge-rich one throughout the thermodynamically accessible range.

In the case of PtGe, the germanium-terminated (101) orientation appears to be most stable under most of the growth conditions, while Ge and Pt terminated (110) surfaces become more stable when growth conditions are Pt rich (Fig. 4.3i). Under Ge-rich conditions (when germanide formation presumably takes place) the next stable surface is Ge and Pt terminated (110). Again the general trend is the Ge-terminated surface is most stable, followed by the stoichiometrically-terminated and finally metal-terminated surface.

Surface	Surface Energy (erg/cm^2)	Work Func. (eV)
NiGe(100)^n	1879.03 - 426.22 μ_{Ni}	4.31
NiGe(100)^g	1505.90 + 426.22 μ_{Ni}	4.53
NiGe(010)^n	1828.33 - 000.00 μ_{Ni}	4.37
NiGe(110)^n	1460.20 + 000.00 μ_{Ni}	4.51
NiGe(110)^g	1310.63 + 000.00 μ_{Ni}	4.76
NiGe(001)	1401.08 - 000.00 μ_{Ni}	4.57
NiGe(120)^n	1598.74 - 177.78 μ_{Ni}	4.64
NiGe(120)^g	1630.74 + 177.78 μ_{Ni}	4.57
NiGe (211)^n	1419.26 - 150.91 μ_{Ni}	4.55
NiGe(211)^g	1300.27 + 150.91 μ_{Ni}	4.55
NiGe (021)^n	1424.50 - 000.00 μ_{Ni}	4.65
NiGe(101)^n	1975.93 - 875.77 μ_{Ni}	4.39
NiGe(101)^g	1504.37 + 875.77 μ_{Ni}	4.58
Ni(111)		5.09, 5.35[a]

Table 4.3c: *Surface energies and work functions for different NiGe surface orientations. Superscript 'g' and 'n' refers to the Ge and Ni terminated surfaces.*

[a] *Experimental value ref. [159].*

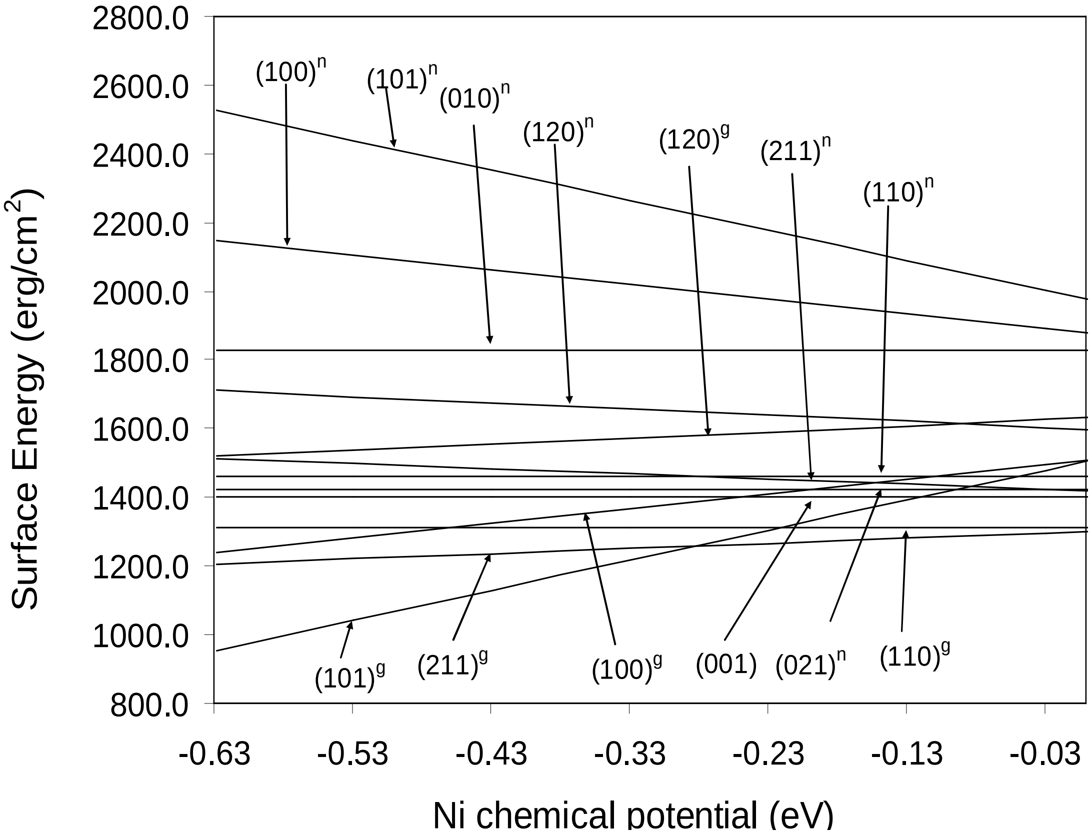

Figure 4.3h: *Surfaces energies of NiGe surfaces as a function of Ni chemical potential. Surfaces with superscript 'n' refer to Ni terminated surfaces while surfaces with superscript 'g' refer to Ge terminated surfaces. Surfaces without any superscripts are stoichiometric.*

Surface	Surface Energy (erg/cm^2)	Work Func. (eV)
$PtGe(100)^p$	$1338.87 - 365.31\ \mu_{Pt}$	4.95
$PtGe(110)^p$	$1112.11 + 000.00\ \mu_{Pt}$	4.88
PtGe(001)	$1110.09 - 000.00\ \mu_{Pt}$	4.83
$PtGe(010)^p$	$1121.33 - 345.95\ \mu_{Pt}$	5.01
$PtGe(111)^p$	$1172.86 - 166.64\ \mu_{Pt}$	4.88
$PtGe(120)^p$	$1143.16 - 156.33\ \mu_{Pt}$	4.93
$PtGe\ (021)^p$	$1102.70 - 000.00\ \mu_{Pt}$	4.97
$PtGe(101)^p$	$1268.19 - 380.30\ \mu_{Pt}$	4.91
$PtGe(101)^g$	$1398.32 + 380.30\ \mu_{Pt}$	4.58
$PtGe(110)^g$	$1015.69 + 000.00\ \mu_{Pt}$	4.87
$PtGe(100)^g$	$1387.50 + 365.30\ \mu_{Pt}$	4.59
Pt(111)		5.70, 5.70[b]

***Table 4.3d**: Surface energies and work functions for different PtGe surface orientations. Superscript 'g and 'p' refers to the Ge and Pt terminated surfaces.*

[b] Experimental value ref. [141].

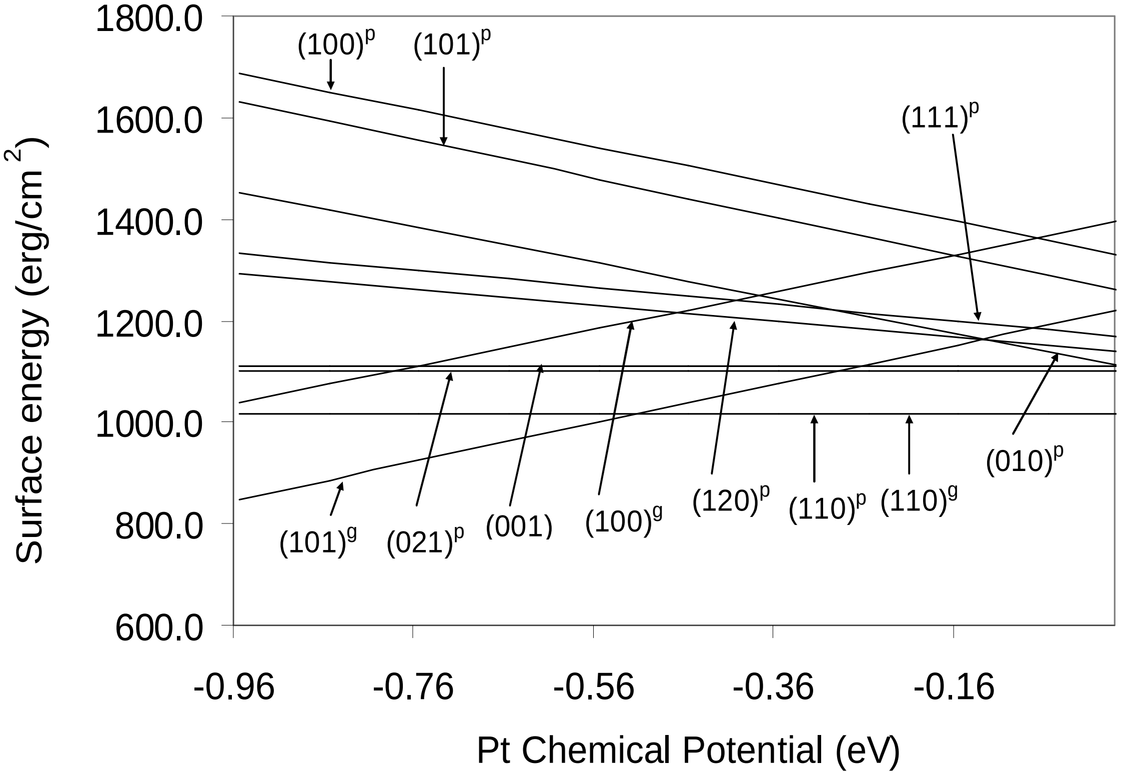

Figure 4.3i: *Surface energies of PtGe surfaces as a function of Pt chemical potential. Surfaces with superscript 'p' refer to Pt terminated surfaces while surfaces with superscript 'g' refer to Ge terminated surfaces. Surfaces without any superscripts are stoichiometric.*

4.4 Work function at different NiGe and PtGe surfaces

We calculate work functions for different surface orientations and terminations of NiGe and PtGe surfaces (listed in Tables 4.3c and 4.3d) using the value of the planar average of the total electrostatic potential at the middle of the vacuum region as E_{Vac} as shown in Fig. 4.4a. For example, the calculated vacuum energy and Fermi energy for the

NiGe (001) surface are 6.22 eV and 1.64 eV, giving the work function of 4.57 eV. The highest φ_m value of 4.76 eV for NiGe is found for the Ge-terminated (110) surface and the lowest of 4.31 eV for the (100) Ni-terminated surface (it has the highest surface energy of all terminations considered), they differ by almost 0.45 eV. Surprisingly, the stoichiometry of the termination (Ge- *vs*. Ni-rich) doesn't show a systematic effect on the work function. The lowest energy NiGe surface Ge-terminated (101) has a work function of 4.58 eV. We find that under the process relevant Ge-rich conditions, three lowest energy terminations: Ge-rich (101), (211) and (100) have practically identical work function of about 4.55 eV.

For PtGe the highest φ_m value of 5.01 eV is found for the (010) metal-rich surface and the lowest of 4.58 eV for the Ge terminated (101) surface, which differ by 0.43 eV. The Ge-terminated surfaces all have lower work functions than the Pt. Also the values for the metal-terminated PtGe surfaces are distributed over a narrow 0.07 eV range around the average value of 4.94eV. However, since the germanide growth takes place under Ge-rich conditions, we expect a lower value of 4.6 eV will be reported. Unfortunately, we know of no experimental data for NiGe and PtGe work functions. To gauge the reliability of our calculated results we calculate the work function of the Ni (111) and Pt (111) surfaces and obtained φ_m= 5.09 eV and φ_m= 5.70 eV. The experimental value reported in the literature for these surfaces are 5.35 eV [159] and 5.70 eV [141] respectively.

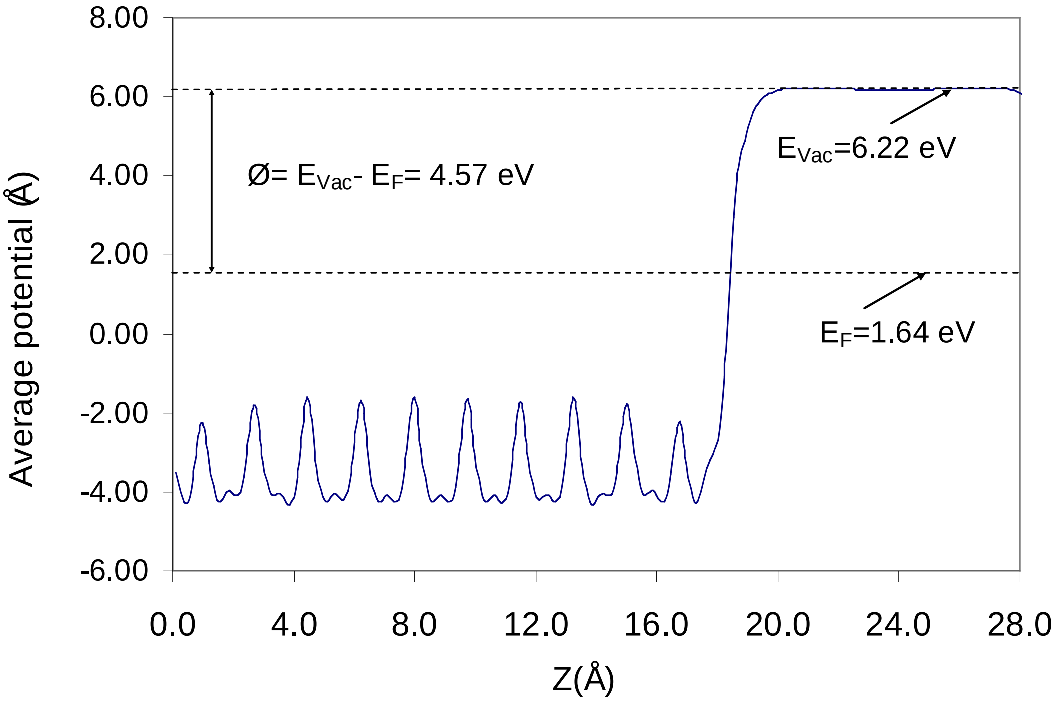

Figure 4.4a: *The planar averaged coulomb potential and work function of the NiGe (001) surface. Z is the direction normal to the (001) surface.*

4.5 Conclusion

With the aid of density functional theory, we have studied the electronic structure of NiGe and PtGe, calculating work functions and surface energies for various surface terminations. Ge-terminated surfaces are found to have lowest surface energies, closely followed by the stoichiometrically terminated surfaces, while metal-rich terminations have much higher energy. We find that the work functions of NiGe and PtGe vary by as much as 0.45 eV and 0.43 eV, respectively, depending on the orientation However, under Ge-rich conditions the lowest energy surface terminations would result in the same work function of about 4.6 eV for both germanides regardless of orientation. For the Ge-rich (101) termination we identify a (1×1) surface reconstruction unusual for metals, which results in the formation of Ge dimers akin those observed on the (100) surface of Ge. The dimer bonding appears to be partially covalent. This reconstruction produces the lowest energy surface.

Chapter 5

Atomic structure and Schottky-barrier height at GaAs/NiPtGe interface

As a result of continuous device scaling silicon-based complementary metal oxide semiconductor (CMOS) technology is rapidly reaching the fundamental limits set by materials properties of Si. This in turn has led to intense research into alternative channel materials. Additionally, the relatively low and disparate mobility of carriers in silicon is a serious obstacle towards the performance goals for CMOS transistors as defined in the International Technology Roadmap for Semiconductors (ITRS) [24]. Recently, III-V compound semiconductors, such as GaAs, InSb, have generated significant attention as potential candidates for a channel material in future CMOS-type devices due to their carrier mobility being much higher than that in silicon [25-27]. Compound semiconductors are also attractive for applications where silicon can not be used, such as optoelectronics, high-power devices, high frequency devices, and high temperature devices. However, despite many advantages, the development of these alternative channel material devices turned out to be quite challenging mainly due to materials related complexities. There are a number of issues which must be addressed before this new strategy can be implemented in CMOS manufacturing. One such issue is related to the contact resistance at the metal-semiconductor interface [28]. To fully exploit transport properties of GaAs and other compound semiconductors, a low resistance contact technology will have to be developed, similar to that based on metal-silicides and used in Si CMOS [1]. Metal germanides have attracted much attention and seem to be very promising in making low resistance contacts since they are closely related to analogous silicides in respect to their composition and structure. The recent renewed interest and active search for suitable germanides are also due to their potential to form ohmic contacts in high performance Ge and $Si_{1-x}Ge_x$ based metal-oxide-semiconductor field effect transistors (MOSFETs). The process is self aligned and relies on a solid phase reaction of Ge and metals [21-23,151,152]. Of several transition metal germanides considered, NiGe and possibly PtGe appear to most promising due to low formation temperature and low resistivity [21-23]. Interestingly, the Ni-Ge system has been used to make contacts in GaAs devices. Further development is required for the nanoscale CMOS device applications, which in turn depends on the understanding and development of high quality GaAs-germanide interfaces.

Using density functional theory we investigate the atomic and electronic structure of the interface and calculate the Schottky barrier height for different GaAs(001) and NiPtGe(001) terminations. Results from first principle calculations are compared to predictions of the widely used metal-induced gap states (MIGS) model. The rest of the chapter is organized as follows. In the next section, we present the calculation methodology and atomic structure of the interface. In section 5.2 we present calculations of Schottky barrier heights at the GaAs(001)/$Ni_{0.5}Pt_{0.5}Ge$(001) and study the effect different GaAs(001) and NiPtGe(001) terminations have on the barrier formation.. In addition, we also estimate SBH at the interface from the simple metal induced gap states (MIGS) model. In section 5.3 we comment upon the details of the electronic structure of the interface.

5.1 Interface Structure

NiGe and PtGe crystallize in the primitive orthorhombic structure in a MnP type lattice with space group Pnma (#62 in the international x-ray table). The Ni (Pt) atoms are six fold coordinated with Ge atoms. The experimental and calculated lattice constants of bulk NiGe, PtGe, $Ni_{0.5}Pt_{0.5}Ge$ and GaAs along with internal plane parameters of Ni, Pt and Ge are presented in Table 5.1a. A more detailed study of electronic structure, elastic properties, surface energies and work functions for various crystal orientations is given in chapter 4

Material		a (Å)	b (A)	c (A)	$u_{Ni\ (Pt)}$	$v_{Ni\ (Pt)}$	u_{Ge}	v_{Ge}
GaAs	cal.	5.76						
	exp.[a]	5.65						
NiGe	cal.	5.84	5.36	3.5	0.1795	0.9933	0.577	0.1769
	exp.[b]	5.79	5.37	3.43	-	-	-	-
PtGe	cal.	6.16	5.83	3.75	0.1922	0.9988	0.5884	0.1857
	exp.[c]	6.09	5.72	3.7	0.1908	0.9995	0.59	0.185
$Ni_{0.5}Pt_{0.5}Ge$	cal.	6.03	5.59	3.65	0.1708	0.9861	0.5987	0.1763
	exp	-	-	-	-	-	-	

[a] Ref. [132], [b] Ref. [149], [c] Ref [150].

Table 5.1a: *Theoretical and experimental lattice constants and internal in-plane coordinates of NiGe, PtGe and* $Ni_{0.5}Pt_{0.5}Ge$*. The Ni (Pt) atoms are located at* $[u_{Ni\ (Pt)}, v_{Ni\ (Pt)}, 1/4]$, $[(1/2 - u_{Ni\ (Pt)}), (v_{Ni\ (Pt)} - 1/2), 1/4]$, $[(1- u_{Ni\ (Pt)}), (1- v_{Ni\ (Pt)}), 3/4,]$ *and* $[(1/2+ u_{Ni\ (Pt)}), (3/2 - v_{Ni\ (Pt)}), 3/4]$*. While the Ge atoms are located at* $[u_{Ge}, v_{Ge} , 1/4]$, $[(3/2- u_{Ge}), (1/2 + v_{Ge}), 1/4]$, $[(u_{Ge} -1/2), (1/2- v_{Ge}), 3/4]$ *and* $[(1- u_{Ge}), (1- v_{Ge}), 3/4]$*.*

We use supercell geometry to simulate the GaAs(001)/NiPtGe(001) interfaces, composed of seventeen layers of alternating planes of Ga and As with thirteen layers of $Ni_{0.5}Pt_{0.5}Ge(001)$ on top in a pseudo-epitaxial arrangement as shown in Figure 5.1b. Figure 5.1a shows the (001) surface (1x1) unit cells of GaAs(001) and $Ni_{0.5}Pt_{0.5}Ge(001)$ surfaces. At the NiPtGe(001) surface, Ni (Pt) atoms are four-fold coordinated with Ge atoms, while Ge atoms are four-fold coordinated with Ni and Pt atoms. The surface unit cell of NiPtGe (001) contains two Ni (Pt) and two Ge atoms. In this work, we study interfaces of Ga- and As-terminated GaAs(001) with NiGe and PtGe terminated $Ni_{0.5}Pt_{0.5}Ge(001)$ surfaces. We also study interfaces with Ge vacancies. The choice of the NiPtGe orientation is driven by its typical work function, relatively low surface energies of NiGe and PtGe (see section 4.3), a reasonable interfacial structure, and by the cell-size limitations of *ab-initio* methods used here. The composition of the germanide alloy is selected to minimize strain in the epitaxial film. Assuming GaAs to be a substrate for a NiGe film the two lateral in-plane lattice constants of NiGe (*a* and *b*) would have to be strained by 1.3% and 7.3%, respectively, to match the bulk GaAs lattice constant. However, strain can be reduced to only 3.04 % and -4.47 % by alloying Pt into NiGe and forming $Ni_{0.5}Pt_{0.5}Ge$. We have tried several other compositions, but limited by the cell size this by far is the best. We have also tested the change in alloy lattice constants by placing two platinum atoms at other substitutional Ni sites, the lattice constants vary only by 0.01 Å or less. Our bulk $Ni_{0.5}Pt_{0.5}Ge$ unit cell contains two Ni, two Pt and four Ge atoms with alternating planes of NiGe(001) and PtGe(001) along the *c* axis. In addition to strain reduction, the alloying of NiGe and PtGe also allows for tuning of the work function of the alloyed metal film (section 4.3). As calculated in section 4.3, NiGe work functions vary between 4.31 eV and 4.76 eV, while PtGe work functions vary between 4.58 eV and 5.01 eV depending on the surface orientation. In our calculations, the in-plane lattice constants of the semiconductor (GaAs) and metal alloy (NiPtGe) films are set to bulk semiconductor lattice constant value. The resulting compressive and tensile strains in the NiPtGe films are accommodated by elongation along the growth direction. The corresponding NiPtGe lattice constant ***c*** along the growth direction is calculated by minimizing the total energy of the strained NiPtGe unit cell. For the inter-planer distance at the interface in the un-relaxed supercell we use the average between the inter-planer distances in the semiconductor and in the metal. We, then, optimize all the internal degrees of freedom and inter-planer distances along the growth direction.

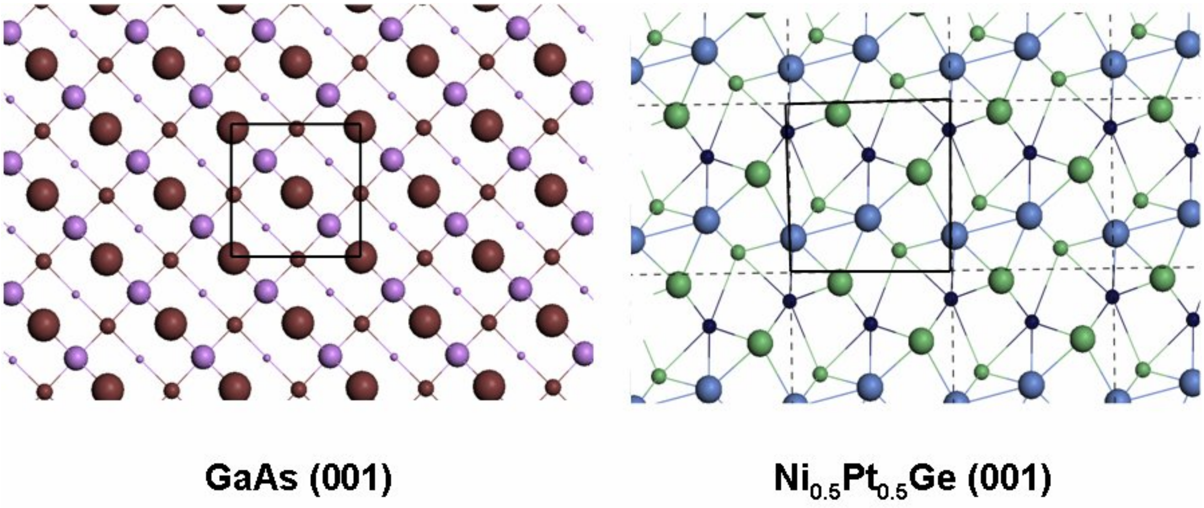

GaAs (001)

$Ni_{0.5}Pt_{0.5}Ge$ (001)

Fig. 5.1a: *Top view of GaAs (001) and NiPtGe (001) surfaces and surface unit cells. Red and violet balls are Ga and As atoms, while green and blue balls are Ge and Ni (Pt) atoms respectively. (Large and small blue balls are Ni and Pt atoms). The NiPtGe(001) surface unit cell contains two Ni (Pt) and two Ge atoms.*

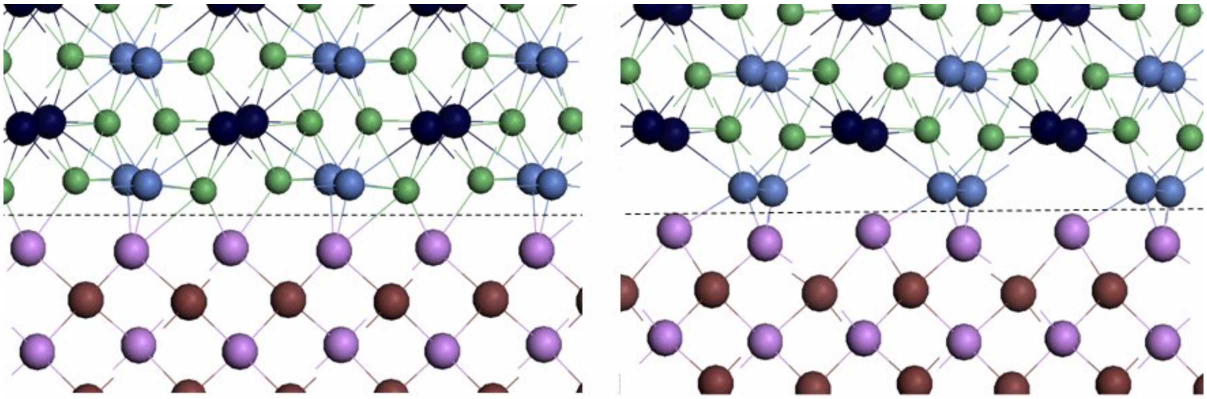

Fig. 5.1b: *(Left) Side view of GaAs (001)/NiPtGe(001) interface with As-terminated GaAs(001) and NiGe terminated NiPtGe (001) surface. (Right) Side view of GaAs (001)/NiPtGe (001) interface with Ge vacancies.*

5.2 Schottky barrier height at the GaAs/NiPtGe interface

We first estimate the Schottky barrier height at the GaAs/NiPtGe interface using semi-empirical models. In a conventional Schottky model (section 1.3) (no Fermi level pinning) the n-type barrier height at the metal-semiconductor interface is given by the difference between the metal work function φ and electron affinity χ of the semiconductor (the energy difference between the conduction band edge and vacuum). Likewise, the p-type Schottky-barrier is the difference between the metal work function and the semiconductor valence band edge, $\chi + E_g - \varphi_m$. The calculated work functions of NiGe-terminated and PtGe terminated $Ni_{0.5}Pt_{0.5}Ge(001)$ surfaces are 4.52 eV and 4.80 eV. It is interesting to note that these work functions are very close to NiGe(001) and PtGe(001) work functions of 4.57 eV and 4.83 eV (Section 4.3). With, $\chi + E_g = 5.50$ eV for GaAs(001) [26], the p-type barriers at the GaAs(001)/NiPtGe(001) interfaces are 0.98 eV and 0.70 eV in the Schottky limit, for the two terminations of the NiPtGe(001). In the Schottky limit, the p-SBH changes with the metal work function in a linear fashion. Section 4.3 lists the NiGe and PtGe work functions at various surface terminations. For instance, NiGe work functions vary between 4.31 eV and 4.76 eV, while PtGe work functions vary between 4.58 eV and 5.01 eV. Thus, in the Schottky limit, the p-SBH at the GaAs-NiPtGe interface can vary by few tenths of a volt depending on the work function of NiPtGe surface. Alternatively, in the Bardeen limit (strong pinning) (section 1.3) the p-type barrier is the difference between the charge neutrality level (ϕ_{CNL}) and the top of the semiconductor valence band. The charge neutrality level in GaAs is 0.70 eV above the valence band edge [160]. Thus, in the Bardeen limit the p-type barrier would be 0.70 eV. In the Bardeen limit, the p-SBH does not depend on the metal work function and is constant for all metal-GaAs interfaces. However, the experimental barrier height at the GaAs-metal interface does weakly depend on the metal work function (section 1.3) and doesn't agree well with either Schottky or Bardeen limit. A more reasonable value of p-SBH can be inferred from the metal induced gap states (MIGS) model (section 1.3). The MIGS model interpolates between the Bardeen and the Schottky limits in a linear fashion, and the p-type barrier ϕ_p, is given by:

$$\phi_p = E_g - S(\phi_m - \phi_{CNL}) - (\phi_{CNL} - \chi);$$

Here, ϕ_{CNL} is the charge neutrality level measured from the vacuum level and E_g is the valence band gap of the semiconductor and ϕ_m is the work function of the metal. S is the empirical pinning parameter describing the screening by the interfacial states (section 1.3)

$$S = \frac{1}{1 + 0.1(\varepsilon_\infty - 1)^2};$$

where, ε_∞ is the high frequency limit of the dielectric constant of the semiconductor. For S=0 and 1 one regains the Bardeen and Schottky limits, respectively. Taking ε_∞ equal to 10.7 for GaAs [143], the S factor is 0.096. Using a value of 4.07 eV for the GaAs electron affinity, we estimate the p-type barrier to be 0.71 eV, close to the Bardeen limit. This is expected since the Fermi level at the GaAs surface is strongly pinned (as described by the pinning factor S). The MIGS estimate of the p-SBH depends very weakly on the work function of the metal because of the very small value of the pinning factor S. For instance, a variation of 0.5 eV in the metal work function would change the MIGS estimate of p-SBH by less than 0.05 eV. We are not aware of any experimental value of p-SBH at a GaAs-NiPtGe interface. However, experimentally p-SBH at metal-GaAs interfaces is found to lie between 0.4 eV and 0.6 eV depending on the metal work function [28]. Since, the estimated value of the NiPtGe(001) work function is 4.70 eV, we can expect an experimental value of ~0.5 eV for p-SBH at the GaAs-NiPtGe interface. We must note that there are number of limitations with the MIGS and other empirical models as described in detail in Ref [70]. Generally, semi-empirical models are unable to describe the dependence of the SBH on the interface structure and hence *ab-initio* calculations of the SBH can be very helpful [70]. *Ab-initio* calculations properly take into account the interface bonding and provide the dependence of the SBH on the interface atomic structure.

To perform a first principles calculation of the Schottky barrier, we use a supercell as described earlier in the section 5.2. To calculate the Schottky-barrier height we need to know the Fermi level and the GaAs valence band edge positions. We follow the procedure originally introduced by Bylander and Kleinman [147] with the exception that only the average electrostatic potential is calculated across the supercell [124]. We first compute the planar average of the electrostatic potential and then its macroscopic average $\overline{V}_{GaAs}$ in the region away from the interface we believe to be bulk-like. Placing the valence band edge with respect to the macroscopic average potential requires a separate calculation for bulk GaAs, where we find the valence band maximum to be $E_{VBM} = 2.06$ eV above the reference $\overline{V}_{GaAs}$. In the case of GaAs(001)/NiPtGe(001) supercell with As-terminated GaAs(001) and Ni-Ge terminated NiPtGe(001), the average electrostatic potential and Fermi energy are at 4.01 eV and 1.43 eV, respectively (Figure 5.2a). Using the bulk reference to locate the valence band top, we calculate the barrier height of 0.52 eV from the formula:

$$\phi_p = E_F - (\overline{V}_{Si} + E_{VBM}),$$

We also calculate p-SBH at GaAs/NiPtGe interfaces with different GaAs(001) and NiPtGe(001) terminations and Ge vacancies. The calculated p-SBH are listed in Table 5.2a. As listed in Table 5.2a, the p-SBH varies as much as by 0.18 eV.

Interface	**GaAs(001)**	**NiPtGe(001)**	**p-SBH (eV)**
GaAs/NiPtGe	As-terminated	Ni-Ge terminated	0.52
GaAs/NiPtGe	As-terminated	Ni-terminated (Ge vacancies)	0.46
GaAs/NiPtGe	Ga-terminated	Ni-Ge terminated	0.47
GaAs/NiPtGe	Ga-terminated	Ni-terminated (Ge vacancies)	0.64
GaAs/NiPtGe	As-terminated	Pt-Ge terminated	0.52
GaAs/NiPtGe	Ga-terminated	Pt-Ge terminated	0.59

Table 5.2a: *Calculated p-Schottky barrier height at the GaAs/NiPtGe interface with different GaAs(001) and NiPtGe(001) termination.*

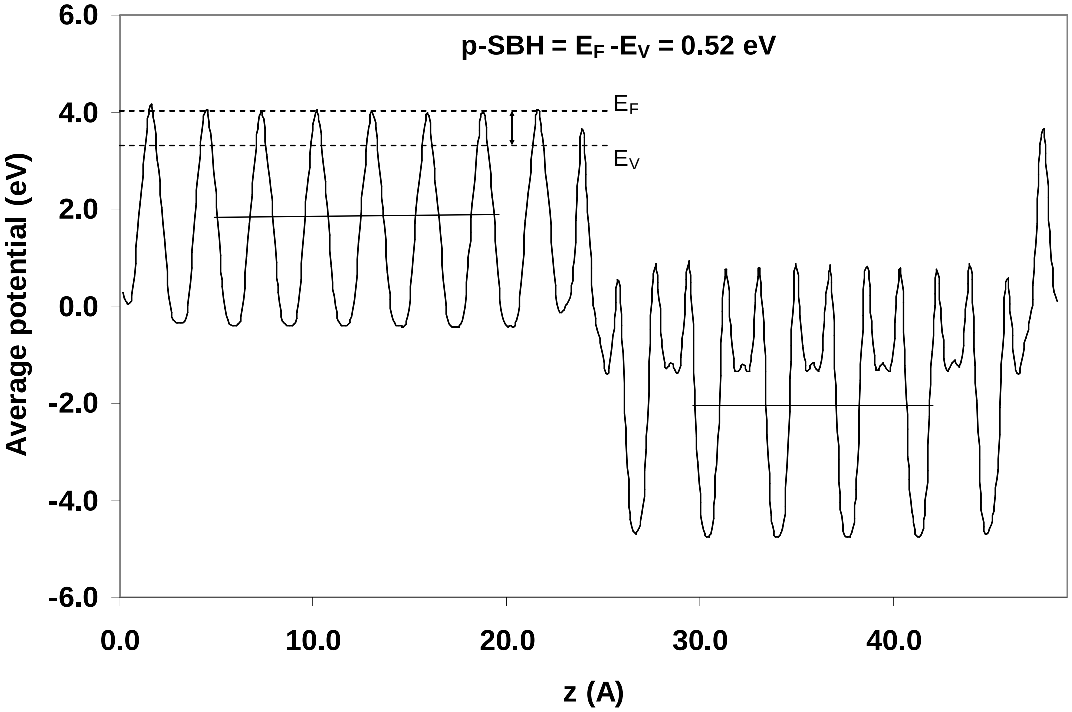

Figure 5.2a: *The average coulomb potential (in eV) in GaAs(001)/NiPtGe(001) supercell along Z (growth axis). The GaAs(001) is As-terminated and NiPtGe(001) is NiGe terminated.*

5.3 Electronic structure of GaAs(001)/$Ni_{0.5}Pt_{0.5}As$(001) interface

Figure 5.1b shows the relaxed GaAs(001)/NiPtGe(001) interface for the case of As-terminated GaAs(001) and NiGe terminated NiPtGe(001). At the relaxed interface, Ni atoms are four-fold and one-fold coordinated with Ge and As atoms, respectively. The first As atom is two-fold coordinated with Ga atoms and with Ni atoms while another As atom is two-fold coordinated with Ga atoms and with Ge atoms. The Ge atoms are four and one fold coordinated with Ni-Pt atoms and As atom, respectively. The bond length between Ni and As atoms is 2.41 Å, close to the bond length between nearest neighbor Ni and As atoms in bulk NiAs. Likewise bond lengths between Ge and As atoms are 2.50 Å and 2.65 Å which is close to the experimental Ge-As bond length of 2.52 Å. Figure 5.3a shows the partial density of states (PDOS) projected onto the *p* states of As atoms located in different layers in the GaAs side of the As-terminated GaAs(001)/NiPtGe(001) supercell. The PDOS of As atoms at the interface differ significantly from those of bulk As atoms. Fig. 5.3a also shows the density of states projected on the Ni atoms (*d* states), Ge atoms (*p* states), Ga atoms (*p* states) and Pt atoms (*d* states) located in different layers in the GaAs (001)/NiPtGe(001) supercell. PDOS of these atoms in different layers are not changed significantly from the bulk states. Figure 5.3b shows a two dimensional band structure along the symmetry lines of GaAs/NiPtGe interfaces together with the projected band structures of bulk GaAs (dark area) and NiPtGe (grey area). The Fermi energy is indicated by a dashed line. Bold lines in the figure indicate interface states. Figure 5.3c shows all the interface states in the semiconductor band gap around the Fermi level. Interfaces states can be either localized or resonance states. Localized interface (Figure 5.3e) states can exist in the mutual gaps of the projected band structure of the two bulk materials. On the other hand resonance states (Figure 5.3d) are degenerate with bulk states of one or both materials. The energy states in the GaAs (semiconductor) band gap can be classified into two categories. One category is interface states whose wave functions are localized near the interface (localized states) and decay on both sides of the interface. The other category is metal induced gap states (MIGS) whose wave functions decay only on the semiconductor side. MIGS form only in the energy region where the bulk band of the metal is projected. Since the two-dimensional energy structure of metal depends on the interface orientation, MIGS depend on the projected metal band structure at the metal-semiconductor interface. Fig. 5.3b indicates that localized states occur deep in the valance band of semiconductor around 8 eV and 12 eV below the Fermi level. The interface state in the mutual band gap at around -8 eV is mainly formed by Ge *p* orbitals, while the state at around -12 eV is from from As *s* orbitals. The interface states in GaAs band gap are formed mainly by As *p* orbitals and Ni *d* orbitals. As apparent from Table 5.2a, As-Ge bonds at the GaAs/NiPtGe interface cause the Fermi level pin strongly. The *p*-SBH variation is least when Ge and As atoms are bonded at the interface. For instance, calculated *p*-SBH is 0.52 eV when GaAs(001) is As terminated and NiPtGe(001) is NiGe or PtGe terminated. With Ge vacancies, the *p*-SBH varies by as much as 0.17 eV.

In case of the GaAs/NiPtGe interface with Ga-terminated GaAs(001) and Ni-Ge terminated NiPtGe(001), the bond lengths between Ga atoms and Ni atoms are 2.38 Å and 2.49 Å. The bond lengths between Ga and Ge atoms are 2.62 Å and 2.98 Å. Figure 5.3f shows the PDOS projected onto Ga atoms (*p* states), Ni atoms (*d* states), and Ge atoms (*p* states) located in the different layers from the interface. The interface states in GaAs band gap are derived from Ga and As *p* orbitals with contribution of Ni *d* orbitals.

In case of the GaAs/NiPtGe interface with As- and PtGe termination of GaAs(001) and NiPtGe(001) surfaces, the bond lengths between Pt and As atoms relax to 2.51 Å. The bond lengths between As atoms and Ge atoms relax to 2.41 Å and 2.91 Å. Figure 5.3g shows the PDOS projected on to different atoms located in the different layers from the interface. As apparent, the interface states in GaAs band gap are formed by As *p* states.

5.4 Conclusion

We have studied the atomic and electronic structure and calculated *p*-SBH of GaAs/NiPtGe interfaces with different GaAs(001) and NiPtGe (001) terminations, within the framework of density functional theory. The calculated *p*-Schottky barrier values vary by as much as 0.18 eV around average value of 0.5 eV. We find that Ge-As bonds at the interface result in strong Fermi level pinning. In addition we also estimate *p*-SBH in Schottky and Bardeen limits and MIGS model. From the calculated work functions of NiPtGe surfaces we further estimate an empirical value of ~0.5 eV for *p*-SBH at GaAs/NiPtGe interface, from the available data on *p*-SBH at different metal/GaAs interfaces.

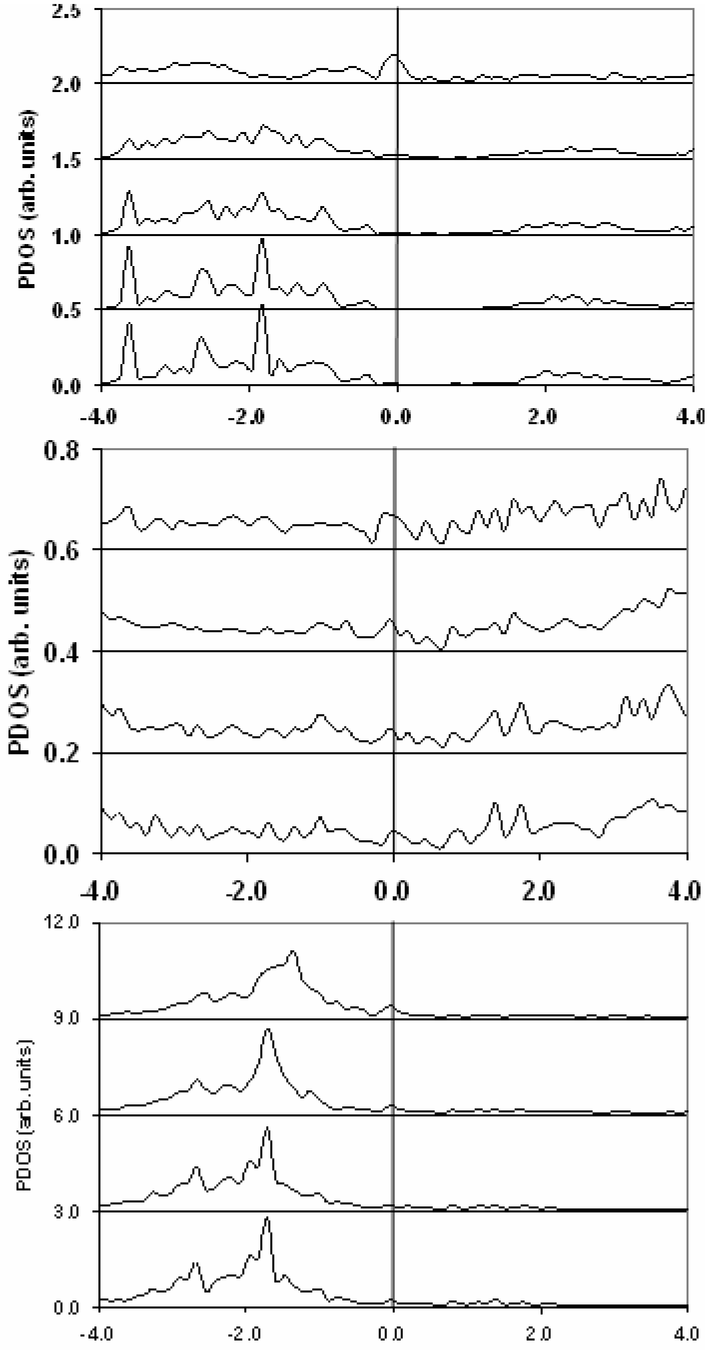

Figure 5.3a: *Density of states projected on p-orbitals of As and Ge atoms, d-orbital of Ni atom located in different layers from the NiPtGe/GaAs interface in the supercell (GaAs(001) is As-terminated and NiPtGe is NiGe terminated). Topmost DOS denotes nearest while bottom-most denotes farthest from the interface.*

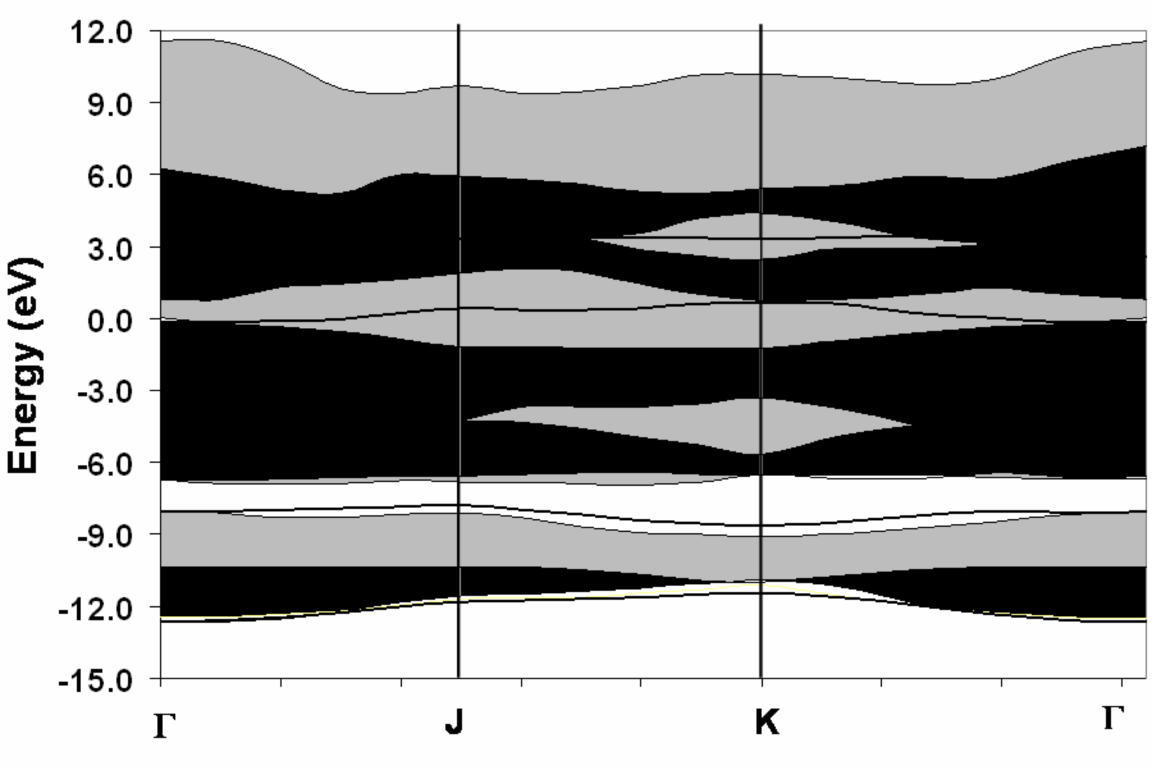

Figure 5.3b: *Two dimensional band structure for GaAs/NiPtGe interface (GaAs(001) is As-terminated and NiPtGe is NiGe terminated). Bulk band structure of GaAs (dark area) and NiPtGe (gray and dark areas) projected along [001] is also shown. Interface bands are shown by dark lines. Fermi energy is at 0 eV.*

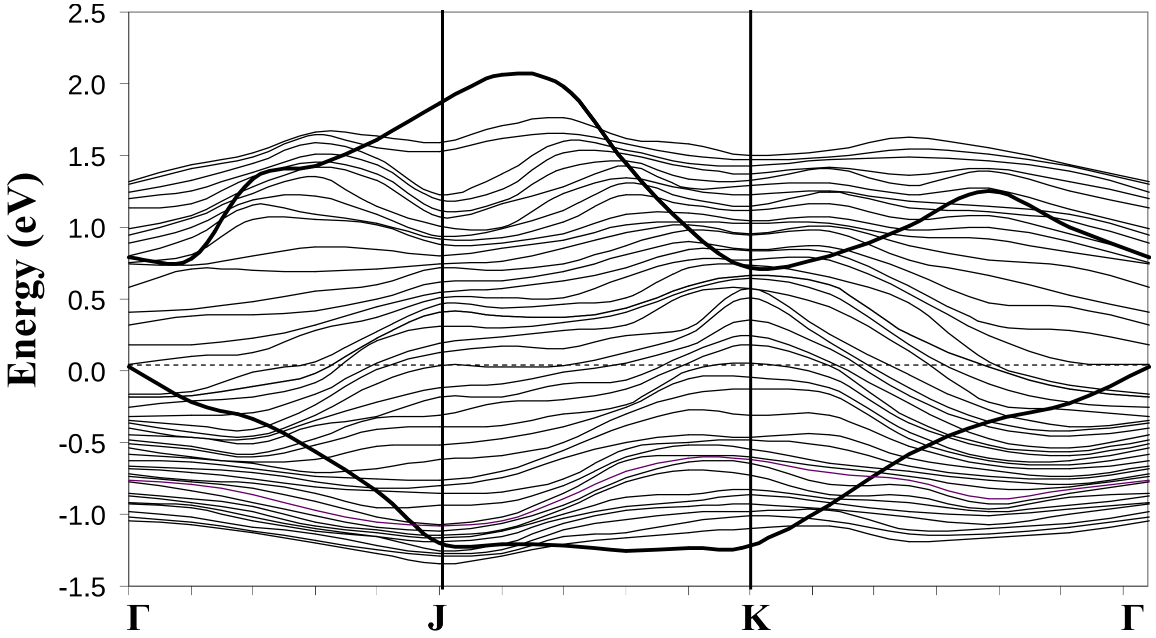

Figure 5.3c: *GaAs/NiPtGe interface bands (light lines) around the Fermi level (dashed line). Dark lines are boundary of GaAs band structure projected along [001]. (GaAs(001) is As-terminated and NiPtGe is NiGe terminated). Complete band structure is shown figure 5.3b*.

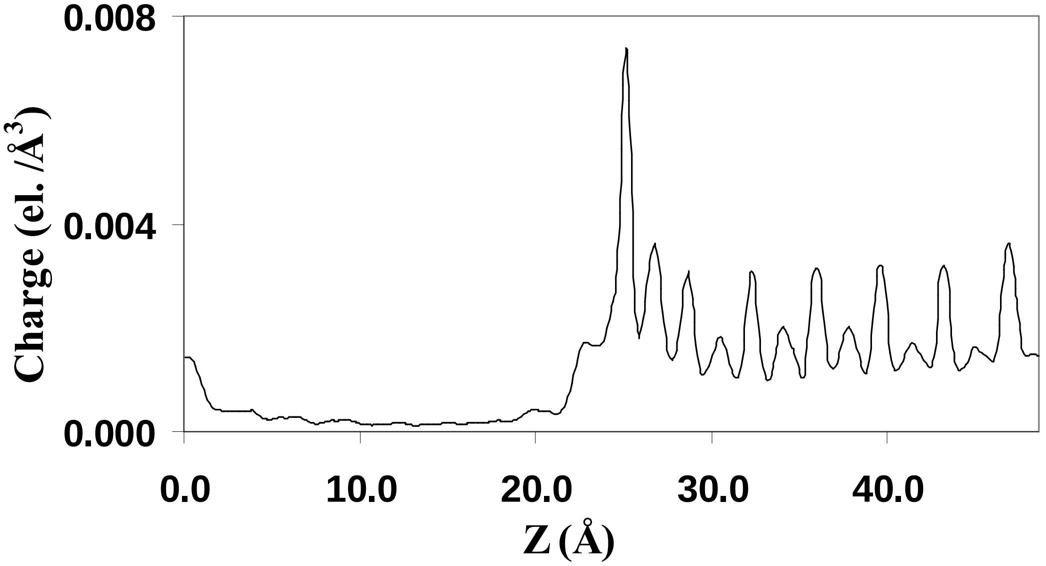

Figure 5.3d: *Charge density along the slab axis for the band (shown in Figure 5.3b) between 0 to 1 eV.*

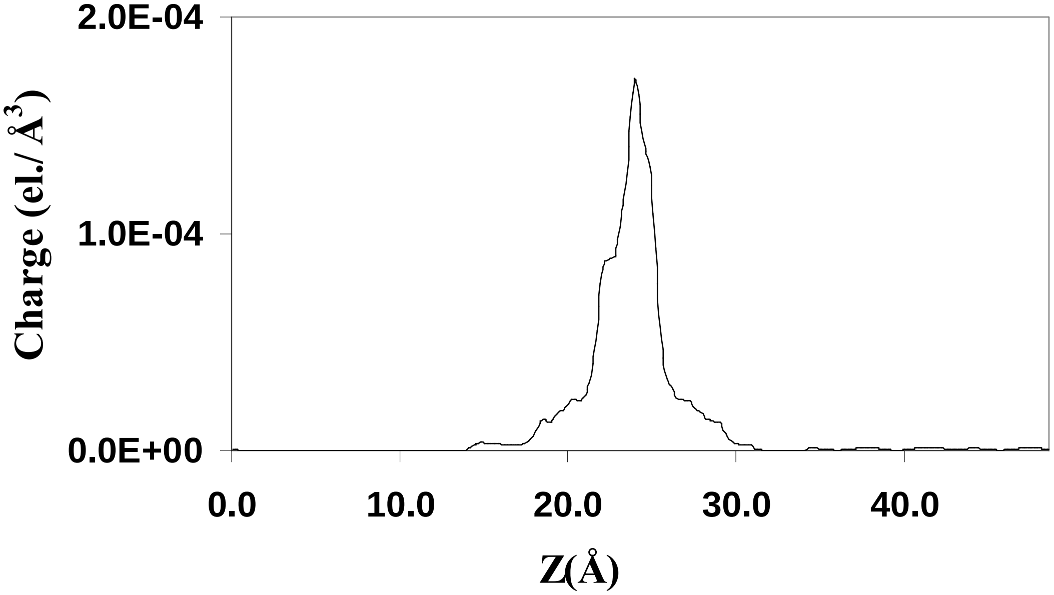

Figure 5.3e: *Charge density along the slab axis for the band (shown in Figure 5.3b) around 8 eV.*

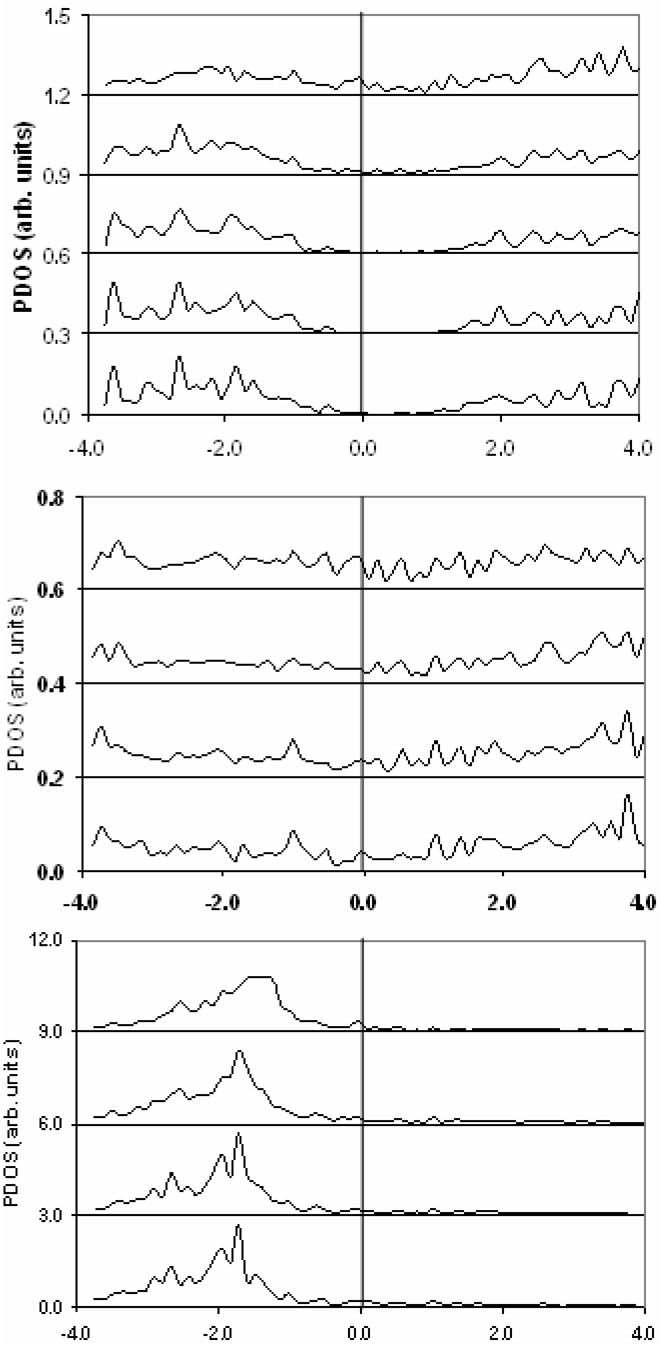

Figure 5.3f: *Density of states projected on p-orbitals of Ga and Ge atoms, d-orbital of Ni atom located in different layers from the NiPtGe/GaAs interface in the supercell (GaAs(001) is Ga-terminated and NiPtGe is NiGe terminated). Topmost DOS denotes nearest while bottom-most denotes farthest from the interface.*

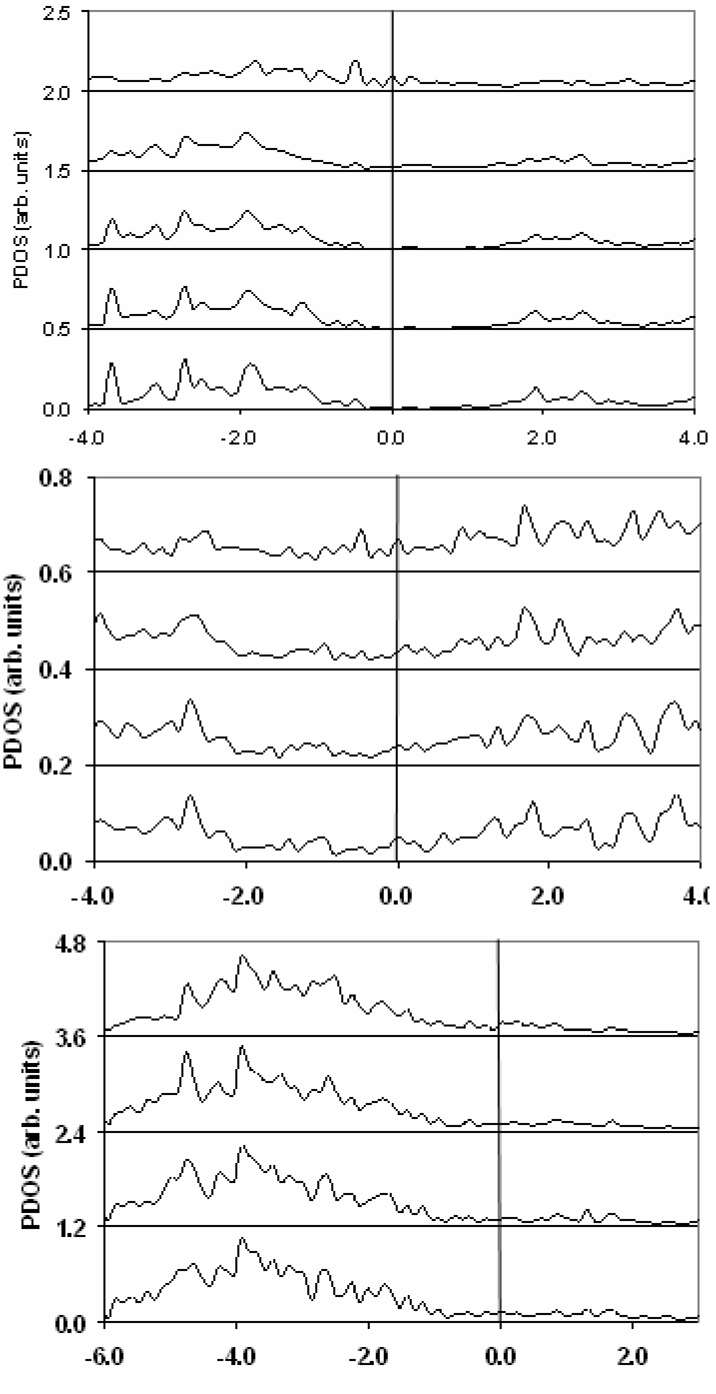

Figure 5.3g: *Density of states projected on p-orbitals of As and Ge atoms, d-orbital of Pt atom located in different layers from the NiPtGe/GaAs interface in the supercell (GaAs(001) is As-terminated and NiPtGe is PtGe terminated). Topmost DOS denotes nearest while bottom-most denotes farthest from the interface.*

Chapter 6

Magnetic state of *β*-MnAs

α-MnAs (Fig. 6a) was studied 100 years ago [161] and found to be ferromagnetic seven years later [162]. There has been recent renewed interest in MnAs because of its possible spintronic applications. Ramsteiner *et al.* [163] have studied spin injection from MnAs layers into GaAs while Tanaka *et al.* [164, 165] have measured the epitaxial orientation and magnetic properties of MnAs thin films grown on GaAs. Although we know of no calculations of *β*-MnAs, there are three calculations [166-168] of the properties of zinc-blende MnAs, a phase which has never been grown and which was shown [7] could not be stabilized either by lattice stretching or compression. More interesting to us is the *β* phase (Fig 6a), which is not ferromagnetic and which experiment has suggested is neither paramagnetic nor antiferromagnetic. The transition from the hexagonal NiAs (space-group number 194) a phase to the orthorhombic MnP (space-group number 62) *β* phase is first order and occurs at 40 °C (Ref. 169) or 44 °C (Ref. 170), the difference probably resulting from slightly different sample stoichiometries. Extrapolation of the magnetization versus temperature curve gives a Curie temperature [171] for the *α* phase of about 127 °C. The resistivity of the *β* phase at 100 °C is about 3.3 times that of a phase at 35 °C [172, 173]]. Ney *et al.* [174] have found that the *α* and *β* phases coexist between 10 and 40 °C in heteroepitaxially constrained MnAs/ GaAs(001) films. The fact that *β*-NiAs transforms to the paramagnetic *γ* phase (with the same NiAs structure as the *α* phase) at 130 °C, essentially the extrapolated Curie temperature of the a phase, together with the anomalous behavior of the inverse susceptibility of the *β* phase, led Guillaud [173] to speculate that *β*-MnAs is antiferromagnetic. However, no long-range magnetic order has been detected by neutron diffraction [169, 175]. Unlike *β*-MnAs, *γ*-MnAs shows normal Curie-Weiss behavior [173]. There have been three different explanations for the *α* to *β* transition. Kittel [176] proposed two ferromagnetic sublattices whose exchange coupling changed sign at the transition temperature leading to a ferromagnetic-antiferromagnetic transition. This theory was rejected by Goodenough and Kafalas [171] because no antiferromagnetic order had been observed. Rodbel *et al.* [177, 178] purported to show with theory and experiment that the transition was ferromagnetic to paramagnetic. Their theory showed how such a phase transition could be first order in a very compressible material with a strongly volume-dependent exchange interaction. The $\alpha \rightarrow \beta$ transition with increasing pressure has been measured by others [171] as has the β to α transition with increasing magnetic field [170, 179]. Goodenough [171, 180] pointed out how the α to β and β to γ transition could be explained by a high spin Mn configuration in the α and γ phases and a low spin Mn configuration in the β phase. Andresen *et al.* [181] found a spiral density wave in β-MnAs. They worked at 4.2 and 80 K without stating whether it was present at both temperatures. The β phase, created with 12.6 kbar of pressure, remains metastable below 160 K at 1 bar. The β phase can also be stabilized by substituting a small amount of V, Cr, Fe, Co, or Ni for the Mn, or P for the As, resulting in a Néel temperature of 200-230 K. Thus, it is unlikely (especially since it has never been observed) that β-MnAs above 40 °C would support a spiral spin-density wave. We now restate the facts concerning the β phase and then give the only description of the β phase consistent with these facts and with Occam's razor. β-MnAs is not ferromagnetic. It is unlikely to be paramagnetic because it does not have Curie or Curie-Weiss behavior. Unlike the α to β transition, Jahn-Teller structurally driven phase transitions go from lower to higher symmetry with increasing temperature. Thus, except for the fact that no antiferromagnetic order has been seen in the β phase, this transition would seem to be magnetically driven, from the high symmetry ferromagnetic state to a lower symmetry antiferromagnetic state. Our solution to this conundrum is that β-MnAs consists of antiferromagnetic planes of Mn but that the exchange coupling between planes is so weak that the ordering of the planes is random, i.e., an up spin in one plane is equally likely to be below an up or a down spin in the plane above. This randomness accounts for the failure of neutron scattering to detect long-range antiferromagnetic order. In the next section we show that this description is consistent with the results of density functional calculations.

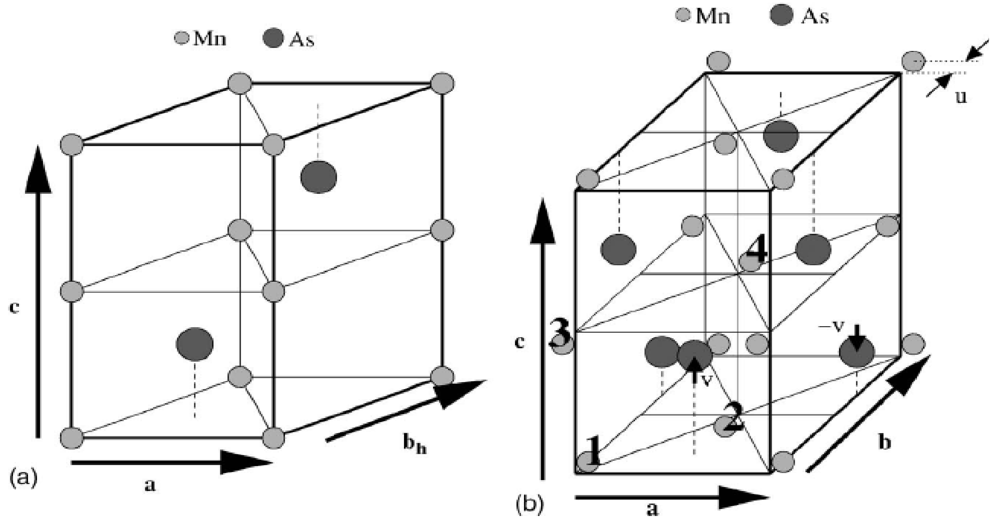

Figure 6a: *(a) α-MnAs (B81) unit cell containing two Mn and two As atoms, (b) β-MnAs (B31) unit cell containing four Mn and four As atoms.*

6.1 Calculations and results

These ultrasoft pseudopotential [85] calculations were done using the PWSCF package of Baroni *et al.* [182]. We sampled a 12×12×8 **k**-point mesh in the hexagonal Brillouin zone (cf. 3×3×3 in Ref. 167) and a 12×8×8 in the orthorhombic. The PBE (Ref. 100) exchange-correlation density functional was used and plane waves up to 35 Ry were used in the expansion. The partial core correction [183] was used on the As atoms, but, in lieu of one on Mn, the Mn 3*s* and 3*p* semicore states were included in the calculations. The hexagonal calculations were converged to 10^{-8} Ry while the orthorhombic calculations were converged to 10^{-5} Ry. The orthorhombic lattice constants and atomic displacements were calculated starting from the experimental values and iterating until all forces were less than 0.4 mRy/bohr and all stresses less than 0.22 mRy/bohr^3. A plot of minus the cohesive energy (obtained by subtracting the energy of spin-polarized atoms from the total energy) and the magnetization of α-MnAs versus volume is displayed in

Fig. 6.1a. One sees that it requires about a 47% reduction in the volume from its equilibrium value to cause the magnetization to disappear in what appears to be a second-order phase transition.

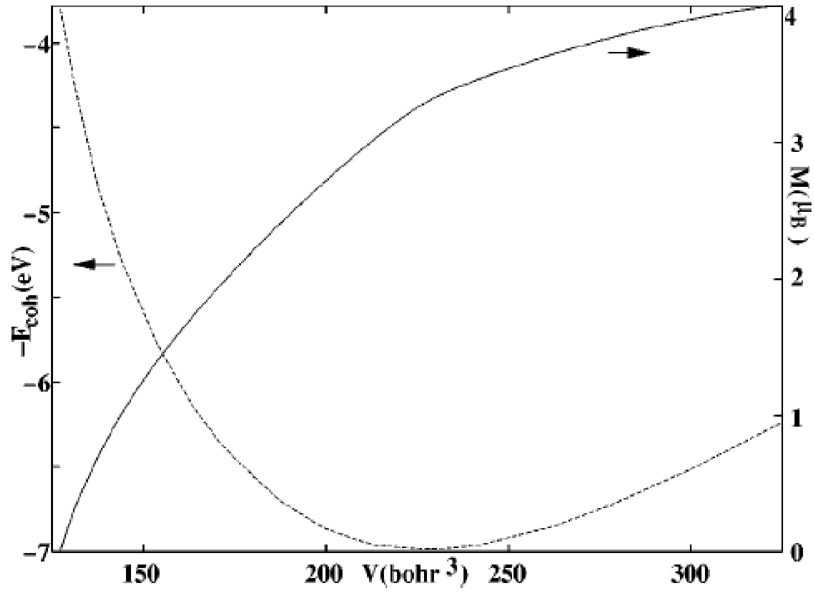

***Figure 6.1a:** Magnetization of a-MnAs in bohr magnetons per MnAs (solid line) and negative of the cohesive energy per MnAs in eV (dashed line) as a function of volume.*

Although there would be a transition to the *β* phase before this occurred, the volume dependent magnetization theory of Rodbell *et al.* [177, 178] does not require a structural transition. Because the *β*-phase volume is only 2% smaller [169] than the *α*, it is highly unlikely that the theory of Rodbell *et al.* is applicable to the phase transition in MnAs. In Table 6.1a, we compare the equilibrium volume, cohesive energy, *c*/*a* ratio, bulk modulus, and magnetization with experiment for *α*-MnAs. The volume and *c*/*a* were measured [181] at 4.2 K. Our 0.96% discrepancy with the experimental volume is extremely small for a density functional calculation while our *c*/*a* ratio is no better than fair agreement with experiment. The *c*/*a* ratio decreased monotonically with volume from 1.76 at V=254.5 bohr^3 to 1.39 at V=649.0 bohr^3. Because of the nonlinearity of the exchange-correlation potential, our excellent agreement with the experimental [171] magnetization might have been slightly worse had more core electrons been included in the calculation. Our zero-temperature bulk modulus seems not inconsistent with the 273-K experimental [184] value. We could find no experimental value for the cohesive energy, but our calculated cohesive energy is quite consistent with our bulk modulus. For example, scandium has a bulk modulus of 43.5 GPa (Ref. 132) and a cohesive energy of 7.8 eV (Ref. 132) per two atoms. Figure 6.1b is a plot of the spin density of states (DOS) at the calculated equilibrium volume. The split off low energy states are the As 4s bands while the higher lying states come from the hybridizing As 4*p* and Mn 3*d* bands.

	Vol	E_{coh}	c/a	M	B
Calc.	456.21	6.982	1.488	3.32	44.5
Expt.	460.62[a]	1.519[a]	3.4[b]	35.8[c]	

TABLE 6.1a: *Equilibrium unit-cell volume (in bohr*^{3}*), cohesive energy (in eV per MnAs), c/a ratio, magnetization (in bohr magnetons per Mn atom), and bulk modulus (in GPa) compared with experiment for α-MnAs. Superscripts a, b and c refers to References [181], [171] and [184] respectively.*

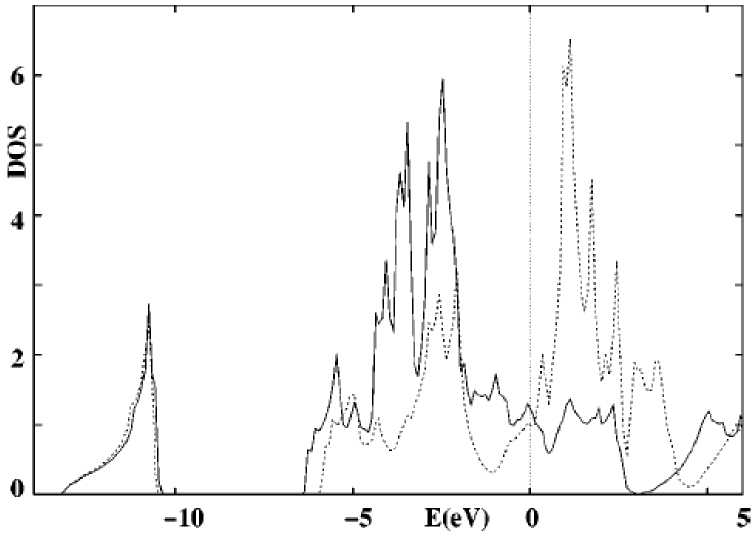

Figure 6.1b: *Majority (solid line) and minority spin (dashed line) densities of states in electrons per eV per unit cell of α-MnAs. The Fermi energy is at E=0.*

The β-MnAs unit cell is obtained from the α by small distortions as follows. A hexagonal lattice has a centered rectangular unit cell with $b = \sqrt{3}a$ and twice the area. b and a each relax by about -1%, almost, but not quite, maintaining their $3^{1/2}$ ratio, while c does not relax at all [169]. Although the unit cell is almost hexagonal, there are sizable inner displacements of the atoms which destroy the almost hexagonal symmetry. We have defined a, b, and c to be consistent with the hexagonal lattice. To get the standard definition used in Ref. [169] (abc)→(bca).

In Table 6.1b we list the cohesive energy and magnetization for ferromagnetic, paramagnetic, and three different antiferromagnetic structures of β-MnAs (Fig 6.1c). The two (001) planes of Mn are ferromagnetic but oppositely polarized in AFI. In AFII the planes are antiferromagnetic with up (down) spins in one plane below up (down) spins in the other, and in AFIII the down (up) spins are below the up (down). The results are listed for the fully relaxed positions as well as for the starting high-temperature [169] lattice constants and inner displacements which are listed in Tables 6.1c and 6.1d. It is interesting to note that with the experimental lattice parameters the ferromagnetic state is still the ground state. It relaxes back to α-MnAs. It is also interesting to note that in spite of their smaller volume, all three antiferromagnets appear to have a larger magnetization than the ferromagnet. This is because all ferromagnets of which we are aware have their magnetization reversed in their interstitial regions. Had we listed the integrated absolute value of the magnetization per Mn atom for the ferromagnetic case as we did for the antiferromagnetic, *M* would have been 3.72 μ_B. The paramagnetic crystal has by far the largest volume relaxation and thus the biggest increase in cohesive energy. Even so, its cohesive energy remains 430-meV below that of AFIII. Thus, there are three reasons to discard it as a possible candidate for β-MnAs above 40 °C: its small cohesive energy, its volume which is much smaller than experiment, and its unusual magnetic susceptibility.

	Ferro	Para	AFI	AFII	AFIII
Expt.	6.973	5.998	6.88	6.909	6.904
Rlx.	6.982	6.507	6.896	6.936	6.937

TABLE 6.1b: *Cohesive energy (per MnAs) calculated at the experimental high-temperature lattice constants and inner displacements as well as with lattice constants and inner displacements relaxed to their equilibrium values for ferromagnetic, paramagnetic, and three antiferromagnetic structures (Fig 6.1c) described in text.*

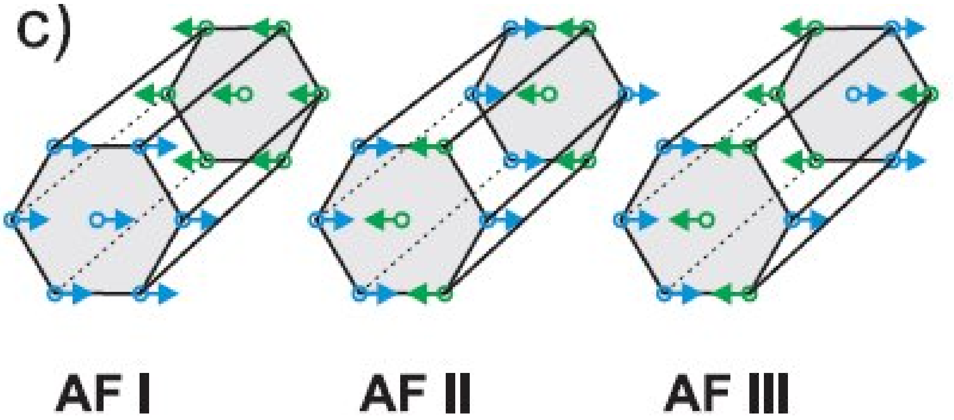

Figure 6.1c: *Antiferromagnetic models of β-MnAs used for calculations.*

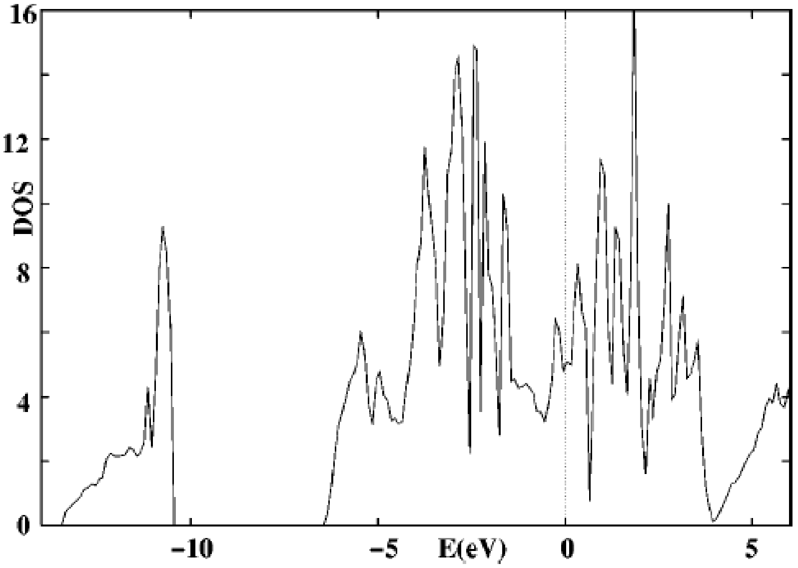

Figure 6.1d: *Total density of states in electrons per eV per unit cell of β-MnAs. The Fermi energy is at E=0.*

In Table 6.1c we note that the relaxed lattice constants of all three antiferromagnetic structures are smaller than the experimental values at 55 °C, as expected, but that they are larger than those measured at 4.2 K under 12.6 kbar of applied pressure while the paramagnetic lattice constants are much smaller than the experimental ones under 12.6 kbar. Table 6.1d displays the displacements of the atoms in the orthorhombic structure away from their positions in the hexagonal structure. One peculiarity is that the atomic displacements of AFI away from hexagonal are much smaller than those of AFII and AFIII but its b/a=1.745 is much further from the hexagonal $\sqrt{3}$ than the 1.731 of both AFII and AFIII. Figure 6.1d is the DOS of AFIII. If we divide these in half (because the unit cell is twice as large) and compare them with the sum of spin DOS of Fig. 6.1b, we see that at the Fermi energy the β-phase DOS is about 8% larger than the α. Thus, the 3.3 times larger resistivity of the β phase [172, 173] must be due to other sources, such as the 65-K higher temperature at which it was measured, in addition to the postulated disorder of its antiferromagnetic planes.

.

	a	b	c	V	M
Ferro.	7.070	12.246	10.522	910.99	3.32
Para.	6.405	11.427	10.215	747.69	0.00
AFI	6.830	11.915	10.768	876.29	3.38
AFII	6.879	11.907	10.732	878.98	3.56
AFIII	6.866	11.888	10.716	874.73	3.40
55°C[a]	6.931	12.032	10.809	901.40	
4.2K[b]	6.603	11.641	10.547	810.70	

TABLE 6.1c: *Calculated orthorhombic lattice constants (in bohr), volume (in bohr^3), and magnetization (in bohr magnetons per MnAs) for the five crystals in Table 6.1b, compared with experimental values at 55 °C and 4.2 K with an applied pressure of 12.6 kbar. Note that b= $3^{1/2}$ a for the ferromagnetic case which has hexagonal symmetry. Superscript a and b refers to references [169] and [181] respectively.*

	α	β	γ	δ
Ferro.	0	0	0	0
Para.	0.0528	0.0056	0.0069	0.0539
AFI	0.0100	0.0014	0.0001	0.0082
AFII	0.0475	0.0135	0.0049	0.0447
AFIII	0.0435	0.0030	20.0019	0.0444
Exp[a]	0.0271	0.0047	0.0020	0.0245

***TABLE 6.1d:** Calculated positions of the atoms within the unit cells of Table 6.1c compared with experiment at 55 °C. The Mn atoms are at [1/4, ¼ - α, -β], [3/4, 3/4 + α, +β], [3/4, 3/4 - α, ½ +β], [1/4, ¼ + α, ½ -β] and the As atoms are at [1/4, -1/12 + γ, ¼ + δ], [3/4, 1/12 - γ, 3/4 + δ], [3/4, 5/12 + γ, ¼ - δ], [1/4, 7/12 - γ, 3/4 + δ]. Superscript 'a' refers to reference [169].*

6.2 Conclusion

We believe that our calculation is sufficiently accurate to discard the possibility of β-MnAs being paramagnetic even without considering its non-Curie-Weiss magnetic susceptibility. Since it is not ferromagnetic, that leaves only the possibility of its being a planar antiferromagnet with planes randomly ordered to account for the lack of observed antiferromagnetic order or its being in some more complicated state that we have not considered. A spin glass seems highly unlikely for an ordered compound and a spin-density wave or spiral spin-density wave would have been detected by neutron scattering. The question then remains, how consistent is this random antiferromagnetic state with our calculations? We see that AFIII (aligned planes) and AFII (staggered planes) are degenerate, which makes it very likely that their free energies at 40 °C will be very close to degenerate and that rather than be staggered or aligned, the planes will be random. We found the random antiferromagnet state lies 40 meV below AFI with its alternating ferromagnetic planes. It also lies 45 meV above the hexagonal ferromagnetic state. The fact that the α → β transition occurs with increasing temperature indicates that there are contributions to the entropy which favor the antiferromagnetic β phase over the ferromagnetic α phase. We can only speculate what these might be. The almost perfect hexagonal lattice symmetry indicates that the inner displacements of Table 6.1d select 1 of 6 equivalent sets of atomic sites. If some of the energy barriers between these sites are small, they could cause there to be very low-frequency phonon modes in the β phase which are not present in the α phase [185]. These, together with the uncertainities of density functional theory, should be sufficient to account for the 45 meV in the free energy needed to account for the transition to the disordered antiferromagnetic state. Therefore, we believe that our proposed disordered antiferromagnetic state is consistent with these calculations and is the most likely state for *β*-MnAs.

REFERENCES

[1] S. Zhang and M. Ostling, Crit. Rev. in Solid State and Mat. Sci. **28**, 1 (2003)

[2] C. Detavernier, A.S. Özcan, J. Jordan-Sweet, E.A. Stach, J. Tersoff, F.M. Ross and C. Lavoie, Nature **426**, 641 (2003).

[3] C. Detavernier and C. Lavoie, Appl. Phys. Lett. **84**, 3549 (2004).

[4] J. Iwai, T. Ohguro, and S. Ohmi, Microel. Eng. **60**, 157 (2002).

[5] S. R. Murarka, *Metallization: Theory and practice for VLSI application* (Butterworth-Heinemann, Boston, 1993).

[6] S. R. Murarka, *Silicides for VLSI Applications* (Academic, New York, 1983)

[7] C. Blair, E. Demirlioglu, E. Yoon, and J. Pierce, *Silicides, Germanides and their interfaces,* edited by R. W. Fathauer, L. Schowalter, S. Mantl, and N. K. Tu, MRS Symposia Proceedings No. 320 (Materials Research Society, Pittusberg, 1994).

[8] W. J. Taylor, M. J. Rendon, E. Verret, J. Jiang, C. Capasso, D. Sing, J. Y. Nguyen, J. Smith, E. Luckowski, A. Martinez, J. Schaeffer, Phil Tobin, Mat. Res. Soc. Symp. Proc. Vol. **810** (2004).

[9] C. Detavernier, C. Lavoie, R.L. Van Meirhaegh e, Thin. Solid Films **468**, 174 (2004)

[10] R.N. Wang and J.Y. Feng, J. Phys.: Condens. Matter **15**, 1935 (2003).

[11] M. Liehr, P.E. Schmid, F.K. Le Gouse, and P.S. Ho, Phys. Rev. Lett. **54**, 2139 (1985).

[12] D. –X. Xu, S. R. Das, L. Erickson, and A. Naem, *Materials Reliability in Microelectronics V,* edited by A. S. Oates, W. F. Filter, R. Rosenberg, A. L. Greer, and K. Gadepally, MRS Symposia Proceedings No. 391 (Materials Research Society, Pittsburgh, 1995), p. 223

[13] D. –X. Xu, J. P. McCaffrey, S. R. Das, G. C. Aers, and L. E. Erickson, Appl. Phys. Lett. **68**, 3588 (1996).

[14] M. L. Lee, E. A. Fitzgerald, M. T. Bulsara, M. T. Currie, and A. Lochtefeld, J. Appl. Phys. **97**, 011101 (2005).

[15] H. Shang, H. Okorn-Schimdt, J. Ott, P. Kozlowski, S. Steen, E. C. Jones, H. –S.P Wong and W. Hanesch, IEEE Electron Device Lett., **24** , 242 (2003).

[16] H. Shang, K. -L Lee, P. Kozlowski, C. D'Emic, I. Babich, E. Sikorski, I. Meikei, H. –S. P. Wong, K. Guarini and W. Haensch, IEEE Electron Device Lett., **25** , 135 (2004).

[17] A. Ritenour, A. Khakifirooz, D. A. Antoniadis, R. Z. Lei, W. Tsai, A. Dimoulas, G. Mavrou, and Y. Panayiotatos, Appl. Phys. Lett. **88**, 132107 (2006).

[18] N. Wu, Q. Zhang, C. Zhu; D. S. H Chan, A. Du, N. Balasubramanian, M. F. Li, A. Chin, J. K. O. Sin, D. –L. Kwong, IEEE Electron Device Lett. **25**, 631 (2004).

[19] J. Bardeen and W.H. Brattain, Phys. Rev. **74**, 230 (1948).

[20] G.D. Wilk and R.M. Wallace, and J.M. Anthony, J. Appl. Phys. **89**, 5243 (2001).

[21] Huang *et. al*, Tech. Dig. Int. Electron Devices Meet., 13.4.1 (2003).

[22] S. Zhu, L. Rui, S. J. Lee, M. F. Li, A. Du, J. Singh, C. Zhu; A. Chin, D. L. Kwong, IEEE Electron Device Lett., **26** , 81 (2005).

[23] D. Z. Chi, R. T. P. Lee, S. J. Chua, S. J. Lee, S. Ashok, and D.-L. Kwong, J. Appl. Phys. **97**, 113706 (2005).

[24] Int. Technol. Roadmap for Semiconductors, 2005 Edition [http://public.itrs.net] (SEMATECH, 2005)

[25] S. Datta, T. Ashley, J. Brask, L. Buckle, M. Doczy, M. Emeny, D. Hayes, K. Hilton, R. Jefferies, T. Martin, T. Philips, D. Wallis, P. Wilding, R. Chau, IEDM Tech. Dig. 2005, 34.1-34.4.

[26] S. Datta, Microelec. Engineering, **84**, 2133 (2007)

[27] R. Droopad, K. Rajagopalan, J. Abrokwah, P. Zurcher, M. Passlack, Microelec. Engineering, **84**, 2138 (2007)

[28] M. Murakami and Yasuo Koide, Crit. Rev. in Solid State and Mat. Sci. **23**, 1 (1998).

[29] Y. Taur and T. H. Ning , *Fundamentals of modern VLSI devices*, Cambridge University Press (1998).

[30] K. K. Ng and W. T. Lynch, IEEE Trans. Electron Devices **ED-34**, 503 (1987).

[31] K. A. Jenkins, J. N. Burghartz, and P. D. Agnello, IEEE Trans. Electron Devices **ED-43**, 759 (1996).

[32] W. Monch, *Electronic structure of metal-semiconductor contacts* (Kluwer, Dordrecht, 1990).

[33] R. T. Tung, Materials Science & Engineering R-Reports, **35**(1-3), 1 (2001).

[34] Crowell, C. R. and Rideout, V. L., Solid State Electron*.,* 12, 89, 1969.

[35] Stratton, R. and Padovani F. A., Solid State Electron*.,* 10, 813, 1967.

[36] Robinson, G. Y., in *Physics and Chemistry of III-V Compound Semiconductor Interfaces,* Wilmsen, C. W., Ed., Plenum Press, New York, 1985, 195.

[37] Sze, S. M., *Physics of Semiconductor Devices,* Wiley, New York, 1981, 245.

[38] G. Margaritondo. *Electronic structure of semiconductor heterojunctions* (Kluwer, Dordrecht, 1988).

[39] G. Margaritondo. Reports on Progress in Physics, **62**(5), 765 (1999).

[40] L. J. Brillson. *Contacts to semiconductors fundamentals and technology* (Noyes Publications, Park Ridge, New Jersey, 1993).

[41] E. H. Rhoderick and R. H. Williams. *Metal-semiconductor contacts* (Clarendon Press, Oxford, 1988), 2nd edition.

[42] E. G. Clarke and A. W. Czanderna, Surface Science, **49**(2), 529 (1975).

[43] L. J. Brillson., Applied Surface Science, **11-2**(JUL), 249 (1982).

[44] A. Zangwill and A. C. Redfield, Journal of Physics F-Metal Physics, **18**(1), 1 (1988).

[45] F. Braun. *Ueber die Stromleitung durch Schwefelmetalle*. Annalen der Physik und Chemie, **153**, 556 (1874).

[46] W. Schottky and W. Deutschmann. *Zum Mechanismus der Richtwirkung von Kupfergleichrichtern*. Physikalische Zeitschrift, **30**, 839 (1929).

[47] E. H. Rhoderick, Journal of Physics D-Applied Physics, **5**(10), 1920 (1972).

[48] A. G. Milnes and D. L. Feucht. *Heterojunctions and metal-semiconductor junctions* (Academic Press, New York, 1972).

[49] F. Capasso and G. Margaritondo (editors). *Heterojunction band discontinuities physics and device applications* (North-Holland, Amsterdam, 1987).

[50] E. H. Rhoderick, Journal of Applied Physics, **46**(6), 2809 (1975).

[51] H. Kroemer, Surface Science, **132**(1-3), 543 (1983).

[52] N. Newman, M. Vanschilfgaarde, T. Kendelwicz, M. D. Williams, and W. E. Spicer, Physical Review B, **33** (2), 1146 (1986).

[53] J. R. Waldrop, Journal of Vacuum Science & Technology B, **2**(3), 445 (1984).

[54] M. Prietsch. *Ballistic-Electron-Emission Microscopy (BEEM) - Studies of Metal-Semiconductor Interfaces with Nanometer Resolution*. Physics Reports-Review Section

of Physics Letters, **253**(4), 164 (1995).

[55] W. J. Kaiser and L. D. Bell, Physical Review Letters, **60** (14), 1406 (1988).

[56] L. D. Bell, W. J. Kaiser, M. H. Hecht, and F. J. Grunthaner, Physics Letters, **52** (4), 278 (1988).

[57] L. J. Brillson. *Surfaces and Interfaces: Atomic-Scale Structure, Band Bendeing and Band Offsets*. In *Handbook on semiconductors* (edited by T. S. Moss), volume 1, pages 281–417 (North-Holland, Amsterdam, 1992)

[58] W. Schottky. *Halbleitertheorie der Sperrschicht*. Naturwissenschaften, **26**(52), 843 (1938).

[59] N. F. Mott, Proceedings of the Cambridge Philosophical Society, **34**, 568 (1938).

[60] S. Kurtin, T. C. Mcgill, and C. A. Mead, Physical Review Letters, **22**(26), 1433 (1969).

[61] M. Schl¨uter, Physical Review B, **17** (12), 5044 (1978).

[62] M. Murakami and Y. Koide, Critical reviews in Solid state and material sciences, 23(1), (1998)

[63] J. Bardeen, Physical Review, **71**, 717 (1947).

[64] I. Y. Tamm. ¨ *Uber eine m¨ogliche Art der Elektronenbindung an Kristalloberfl¨achen*. Physikalische Zeitschrift der Sowjetunionen, **1**, 733 (1932).

[65] W. Shockley, Physical Review, **56**, 317323 (1939).

[66] A. M. Cowley and S. M. Sze, Journal of Applied Physics, **36**(10), 3212 (1965).

[67] V. Heine, Physical Review, **138**(6A), 1689 (1965).

[68] W. E. Spicer, P. W. Chye, P. R. Skeath, C. Y. Su, and I. Lindau, Journal of Vacuum Science & Technology, **16**(5), 1422 (1979).

[69] H. Hasegawa and H. Ohno, Journal of Vacuum Science & Technology B, **4** (4), 1130 (1986).

[70] R. T. Tung, Physical Review Letters, **84** (26), 6078 (2000).

[71] J. Tersoff, Physical Review Letters, **52** (6), 465 (1984).

[72] J. J. Rehr and W. Kohn, Phys. Rev. B **9**, 1981 (1974)

[73] H. H. Wieder, Journal of Vacuum Science & Technology, **15** (4), 1498 (1978).

[74] W. Monch, J. Vac. Sci. Technol. B **17**, 1867 (1999)

[75] R. T. Tung, Phys. Rev. Lett. **52**, 461 (1984)

[76] R. G. Dandrea and C. B. Duke, J. Vac. Sci. Technol. B **11,** 1553 (1993)

[77] J. L. Freeouf, Appl. Phys. Lett. **41**, 285 (1982).

[78] R. T. Tung, J. Vac. Sci. Technol. B **11**, 1546 (1993).

[79] R. P. Iczkowsky and J. L. Margrave, J. Am. Chem. Soc. **83**, 3547 (1961).

[80] A. K. Rappe and W. A. Goddard III, J. Phys. Chem. **95**, 3358 (1991).

[81] R. Winkler and S. T. Pantelides, J. Chem. Phys. **106**, 7714 (1997).

[82] M. Schlüter, Phys. Rev. B **17**, 5044 (1978)

[83] P. Hohenberg, and W. Kohn, Phys. Rev. **136,** B864 (1964).

[84] W. Kohn, and L. J. Sham, Phys. Rev. **140**, A1133 (1965).

[85] D. Vanderbilt, Physical Review B, **41**(11), 7892 (1990).

[86] P. E. Blöchl, Phys. Rev. B **50**, 17953 (1994).

[87] E. K. U. Gross and R. M. Dreizler. *Density functional theory an approach to the quantum many-body problem* (Springer, Berlin, 1990).

[88] W. Kohn. *Highlights of Condensed-Matter Theory*. In *International School of Physics "Enrico Fermi"* (edited by F. Bassani, F. Fumi, and P. Tosi), pages 1–15 (North-Holland, Amsterdam, Varenna on Lake Como, Villa Monastero, 28 June - 16 July 1983, 1985).

[89] R. G. Parr andW. Yang. *Density-functional theory of atoms and molecules* (Oxford University Press, New York, 1989).

[90] R. O. Jones and O. Gunnarsson, Reviews of Modern Physics, **61**(3), 689 (1989).

[91] W. E. Pickett, Computer Physics Reports, **9**(3), 115 (1989).

[92] R. M. Martin, *Electronic Structure* (Cambridge University Press, Cambridge, 2003)

[93] M. Born and J. R. Oppenheimer, "*Zur Quantentheorie der Molekeln*", Ann. Physik 84:457, 1927

[94] H. Hellmann. *Einf˙uhrung in die Quantenchemie* (Deuticke, Leipzig, 1937)

[95] R. P. Feynman, Physical Review, **56**, 340 (1939).

[96] W. Kohn and L. J. Sham, Physical Review, **137**, A1697 (1965).

[97] D. M. Ceperley and B. J. Alder, Physical Review Letters, **45**(7), 566 (1980).

[98] J. P. Perdew and A. Zunger, Physical Review B, **23**, 5048 (1981).

[99] J. P. Perdew and Y. Wang, Phys. Rev. B, **45**, 13244 (1992)

[100] J. P. Perdew, K.Burke, and M. Ernzerhoff, Phys. Rev. Lett. **77**, 3865 (1996).

[101] B. Holm and U. von Barth, Physical Review B, **57**(4), 2108 (1998).

[102 B. Holm, Physical Review Letters, **83**(4), 788 (1999).

[103] N. W. Ashcroft and N. D. Mermin. *Solid state physics* (Saunders College, Philadelphia, 1976).

[104] J. Ihm, A. Zunger, and M. L. Cohen, Journal of Physics C-Solid State Physics, **12**(21), 4409 (1979).

[105] O. H. Nielsen and R. M. Martin, Physical Review B, **32**(6), 3792 (1985).

[106] O. H. Nielsen and R. M. Martin, Physical Review B, **32**(6), 3780 (1985).

[107] J. C. Phillips and L. Kleinman, Phys. Rev., **116**, 287 (1959)

[108] W. E. Pickett, Computer Physics Reports, **9**(3), 115 (1989).

[109] D. R. Hamann, M. Schl¨uter, and C. Chiang, Physical Review Letters, **43**, 1494 (1979).

[110] G. B. Bachelet, D. R. Hamann, and M. Schl¨uter, Physical Review B, **26**(8), 4199 (1982).

[111] D. Vanderbilt, Physical Review B, **41**(11), 7892 (1990).

[112] N. Troullier and J. L. Martins, Physical Review B, **43**(3), 1993 (1991).

[113] L. Kleinman and D. M. Bylander, Physical Review Letters, **48**(20), 1425 (1982).

[114] X. Gonze, P. Kackell, and M. Scheffler, Physical Review B, **41**(17), 12264 (1990).

[115] X. Gonze, R. Stumpf, and M. Scheffler, Physical Review B, **44**(16), 8503 (1991).

[116] P. E. Blöchl, Phys. Rev. B **50**, 17953 (1994).

[117] A. Baldereschi, Physical Review B, **7**(12), 5212 (1973).

[118] H. J. Monkhorst and J. D. Pack, Physical Review B, **13**(12), 5188 (1976).

[119] G. Gilat, J. Comput. Phys. **10**, 432-65, 1972

[120] A. H. MacDonald, S. H. Vosko, and P. T. Coleridge, J. Phys. C: Solid State Phys. 12:2291-3002, 1979

[121] P. E. Blochl, O. Jepsen, and O. K. Andersen, Phys. Rev. B **49**, 16223-16233, 1994.

[122] L. Kleinman, Physical Review B, **24**(12), 7412 (1981)

[123] S. Baroni, R. Resta, A. Baldereschi and M. Peressi, in: Spectroscopy of Semiconductor Microstructures, Eds. G. Fasol, A. Fasolino and P. Lugli (Plenum, London, 1989) p. 251.

[124] C. G. Van de Walle, R. M. Martin, Phys. Rev. B **34** 5621 (1986); C. G. Van de Walle, R. M. Martin, Phys. Rev. B **35** 8154 (1987);

[125] S. Massidda, B.I. Min and A.J. Freeman, Phys. Rev. B **35** (1987) 9871.

[126] Zhu, X. and S.G. Louie, Phys. Rev. B **43**, 14142 (1991)

[127] Bylander, D.M. and L. Kleinman, Phys. Rev. Lett. **60,** 472 (1988)

[128] A. Baldereschi, S. Baroni and R. Resta, Phys. Rev. Lett. **61**, 734 (1988).

[129] G. X. Qian, R. M. Martin and D. J. Chadi, Phys. Rev. B, **38**, 7649 (1992)

[130] F. Reif, *Fundamentals of statistical and Thermal Physics* (McGraw-Hill, New York, 1965)

[131] J. F. Nye, *Physical Properties of Crystals* (Oxford University Press, Oxford, 1985)

[132] D. C. Wallace, *Thermodynamics of Crystals* (Wiley, New York, 1972).

[128] H. Pfisterer and K. Schubert, Z. Metallkd. **41**, 358 (1950).

[129] E. J. Graeber, R. J. Baughman, and B. Morossin, Acta Cryst. B **29**, 1991 (1973).

[130] N. Franco, J. E. Klepeis, C. Bostedt, T. Van Buuren, C. Heske, O. Pankratov, T. A. Callcott, D. L. Ederer, and L. J. Terminello, Phys. Rev. B **68**, 045116 (2003).

[131] O. Beckstein, J. E. Klepeis, G. L. W. Hart, and O. Pankratov, Phys. Rev. B **63**, 134112 (2001).

[132] C. Kittel, Introduction to Solid State Physics, 6th ed. (Wiley, New York, 1986).

[133] E. J. Graeber, R. J. Baughman, and B. Morossin, Acta. Cryst. B **29**, 1991 (1973).

[134] G. Kresse, and J. Furtmuller, Phys. Rev. B **54**, 11169 (1996).

[135] I. G. Batyrev, L. Kleinman and J. Leiro, Phys. Rev. B **70**, 073310 (2004).

[136] J. Padilla and D. Vanderbilt, Surf. Sci. **418**, 64 (1998).

[137] A. A. Naem, J. Appl. Phys. **64**, 4161 (1988).

[138] A. K. Pant, S. P. Murarka, C. Shepard and W. Lanford, J. Appl. Phys. **72**, 1833 (1992).

[139] C. Chang, B. Cunningham, A. Segmüller, H. C. W. Huang, F. E. Turene, A. Sugerman, and P. A. Totta, J. Vac. Sci. Technol. B **4,** 745 (1986).

[140] X. Zhang, A.A. Demkov, H. Li, X. Hu, Y. Wei, J. Kulik, Phys. Rev. B **68**, 125323 (2003).

[141] M. Kiskinova, G. Pirug and H. P. Bonzel, Surf. Sci. **133**, 321 (1983).

[142] R. Smoluchowski, Phys. Rev. **60**, 661 (1941).

[143] S. Adachi, “Properties of group –IV, III-V and II-VI semiconductors”, (John Wiley & Sons, Chichester, West Sussex, UK, 2005)

[144] M. Elices and F. Yndurain, J. Phys. C: Solid State Phys. **5**, L146 (1972).

[145] C. Detavernier, C. Lavoie, and F. M. d’Heurle, J. Appl. Phys. **93**, 2510 (2003).

[146] X. Zhang, A.A. Demkov, H. Li, X. Hu, Y. Wei, J. Kulik, Phys. Rev. B **68**, 125323 (2003).

[147] D. M. Bylander and Leonard Kleinman, Phys. Rev. B, **36**, 3229 (1987)

[148] V. W. Chin, M. A. Green, and J. W. V. Storey, Solid-State Electron. **36**,1107 (1993).

[149] J. Y. Spann, R. A. Anderson, T. J. Thornton, G. Harris, C. Tracy, IEEE Electron Device Lett., **26**, 151 (2005).

[150] E. J. Graber, R. J. Baughman, and B. Morosin, Acta. Crys. B **29**, 1991 (1973).

[151] B. Balakrisnan, C. C. Tan, S. L. Liew, P. C. Lim, G. K. L. Goh, Y. L. Foo, and D. Z. Chi, Appl. Phys. Lett. **87**, 241922 (2005).

[152] R. Nath, C. W. Soo, C. B. Boothroyd, M. Yeadon, D. Z. Chi, H. P. Sun, Y. B. Chen, X. Q. Pan, and Y. L. Foo, Appl. Phys. Lett. **86**, 201908 (2005).

[153] J. C. Slater, Symmetry and energy bands in crystals, Dover ed. (Dover, New York, 1972)

[154] P. Ravindran, L. Fast, P. A. Korzhavyi, B. Johansson, J. Wills, and O. Eriksson, J. Appl. Phys. **84**, 4891 (1998).

[155] E. Birch, J. Geophys. **83**, 1257 (1978).

[156] MacFarlane et. al. Phys. Lett. **18**, 91 (1965).

[157] M. E. Fine, J. App. Phys. **26**, 862 (1995).

[158] *Low frequency Properties of Dielectric Crystals*, Vol. 29a Landolt-Bornstein, New Series, Group III, edited by D.F. Nelson (Springer, Berlin, 1992).

[159] B. G. Baker, B. B. Johnson and G. L. C. Maire, Surf. Sci. **24**, 572 (1971).

[160] F. Flores, A. Munoz and J. C. Duran, Appl. Surf. Science, **41/42,** 144 (1989).

[161] F. Heuser, Z. Angew. Chem. **17**, 260 (1904).

[162] S. Hilpertand and T. Dieckmann, Ber. Dtsch. Chem. Ges. A **44**, 2378 (1911).

[163] M. Ramsteiner, H. Y. Hao, A. Kawaharazuka, H. J. Zhu, M. Kastner, R. Hey, L. Daweritz, H. T. Grahn, and K. H. Ploog, Phys. Rev. B **66**, 081304(R) (2002).

[164] M. Tanaka, J. P. Harbison, M. C. Park, T. Shin, and G. M. Rothberg, T. Shin, Appl. Phys. Lett. **65**, 1964 (1994).

[165] M. Tanaka, K. Saito, M. Goto, and T. Nishmaga, J. Magn. Magn. Mater. **198-199**, 719 (1999).

[166] T. Ogawa, M. Shirai, N. Suzuki, and I. Kitagawa, J. Magn. Magn. Mater. **196-197**, 428 (1999).

[167] Stefano Sanvito and Nicola A. Hill, Phys. Rev. B **62**, 15 553 (2000).

[168] Yu-Jun Zhao, W. T. Geng, A. J. Freeman, and B. Delley, Phys. Rev. B **65**, 113202 (2002). Note that the α and β phase notation in this paper is not standard.

[169] R. H. Wilson and J. S. Kasper, Acta Crystallogr. **17**, 95 (1964).

[170] F. Ishikawa, K. Koyama, K. Watanabe, and H. Wada, Jpn. J. Appl. Phys., Part 2 **42**, L918 (2003).

[171] J. B. Goodenough and J. A. Kafalas, Phys. Rev. **157**, 389 (1967).

[172] A. Serres, J. Phys. Radium **8**, 146 (1947).

[173] C. Guillaud, J. Phys. Radium **12**, 223 (1951).

[174] A. Ney, T. Hesjedal, C. Pampuch, A. K. Das, L. Daweritz, R. Koch, K. H. Ploog, T. Tolinski, J. Lindner, K. Lenz, and K. Baberschke, Phys. Rev. B **69**, 081306(R) (2004).

[175] G. E. Bacon and R. Street, Nature (London) **175**, 518 (1955).

[176] C. Kittel, Phys. Rev. **120**, 335 (1960).

[177] C. P. Bean and D. S. Rodbell, Phys. Rev. **126**, 104 (1962).

[178] R. W. De Blois and D. S Rodbell, Phys. Rev. **130**, 1347 (1963).

[179] J. Mira, F. Rivadulla, J. Rivas, A. Fondado, T. Guidi, R. Caciuffo, F. Carsughi, P. G. Radaellil, and J. B. Goodenough, Phys. Rev. Lett. **90**, 097203 (2003).

[180] J. B. Goodenough, M.I.T. Lincoln Laboratory, Lexington MA, Technical Report No. 345, DDC 435758, 1964 (unpublished).

[181] A. F. Andresen, H. Fjellvag, and B. Lebech, J. Magn. Magn. Mater. **43**, 158 (1984).

[182] S. Baroni, A. Dal Corso, S. de Gironcoli, and P. Giannozzi, http:// www.pwscf.org

[183] S. G. Louie, S. Froyen, and M. L. Cohen, Phys. Rev. B **26**, 1738 (1982).

[184] *Handbook of Physical Quantities*, edited by Igor. S. Grigoriev and Evgenii Z. Meilikhov, (CRC Boca Raton, 1997).

[185] We know of no experimental or theoretical work to confirm or refute this speculation. A calculation to compare the phonon spectra of the two phases is possible, but the purpose of this paper is to determine the magnetic structure of the b-phase and not to find the cause of the a to b transition.

VITA

Manish Kumar Niranjan was born in Lalitpur, U.P, India on July 22, 1977, the son of Ashok Niranjan and Asha Niranjan. After completing his work at Jawahar Navodaya Vidyalaya, Lalitpur, U.P, India, in 1995, he entered Indian Institute of Technology, Kharagpur, India. He received the B.Sc and M.Sc (Integrated M.Sc) from Indian Institute of Technology, Kharagpur, India, in May 2000. In August 2000 he entered the Graduate School of The University of Texas.

Permanent Address: Azad Pura, Guru Nanak Market, Lalitpur, U.P, India 284403

This dissertation was typed by the author